An Experimental and Computational Approach to the Development of SERS Substrates for Water Quality Monitoring Sensors

by

©Behrang Moazzez

A Dissertation submitted to the
School of Graduate Studies in partial fulfillment of the requirements for the degree of

Doctor of Philosophy

Department of Chemistry

Memorial University of Newfoundland

October 2014

St. John's Newfoundland and Labrador

Abstract

This PhD thesis presents three essential aspects for an optical sensor suitable for use in harsh environments. The first of these is a robust gold film layer. The second is the metallic rough film with tendency to engage the hydrocarbon on the surface for detection with surface enhanced Raman spectroscopy (SERS). The third is predicting the Raman responses of the confined hydrocarbon molecules for altered laser field directions.

The first project delineates a promoter-free protocol to improve the adhesion of thermally evaporated gold thin films by depositing the gold layer on SU-8 photoresist prior to UV exposure, and post-exposure baking steps of SU-8 processing. The higher adhesion of the top gold film to the post-deposition cured SU-8 sublayer is a product of shrinkage and distribution of residual stresses, due to cross-linking of the SU-8 polymer layer in the post-exposure baking step. The SU-8 underlayer can also impact the resulting gold film morphology. This approach is easily integrated with existing processes and can be used in a wide range of applications including, but not limited to, several types of optical sensors, where good adhesion of gold to a substrate is important and where controlled topography/roughness is key. In this project, a stable gold thin film substrate was developed specifically to address the mechanical properties required to avoid delamination and functionality in harsh environments, because gold thin films are naturally vulnerable to thermal shocks introduced during

different fabrication steps of the sensor package and when introduced to cold ocean water where the sensor package will be used. In addition, the findings are also beneficial for the development of gold coated cantilevers for atomic force microscopy (AFM) and for MEMS-based sensors.

For the first time, a mixed gold/chromium substrate is proposed and developed to tune surface features to generate a better SERS signal of the analyte in use. This alloy (SERS) substrate allows for detection of phenanthrene, a prominent member of the polycyclic aromatic hydrocarbons (PAHs), at low levels. Gold/chromium bilayer films with three different thickness ratios were deposited on glass by thermally evaporating layers of chromium and gold. Subsequent thermal annealing procedures either at 325 °C or 400 °C for either one or two hours were performed on bilayer films. Annealing led to the creation of gold and chromium islands. Atomic force microscopy (AFM), scanning electron microscopy (SEM), and energy dispersive X-ray (EDX) reveal that islands resulting from annealing-based segregation could reach the morphology and composition giving SERS activity for detection of phenanthrene. UV-Vis reflectance illustrates that films annealed at 400 °C show more intense scattering behavior than bilayer films. SERS activity tests with 532 nm excitation using confocal Raman spectroscopy show better response for annealed substrates with thicker top gold layers, with the best enhancement for those annealed at 400 °C for two hours.

A reproducible SER spectrum has been the target of many studies for the last five decades. One of the difficulties with reproducibility and quantification of analytes in trace concentrations comes from the changing interaction angle of the analyte with the laser electric field due to random movements. Here, quantum chemical time-dependent Hartree-Fock (TDHF) calculations are conducted to indicate the effect of the laser field direction and energy on the Raman spectra (peak shape and intensity) of oriented and free phenanthrene and naphthalene molecules. These findings can inform

and improve SERS experiment and sensor design by determining the appropriate molecular orientation(s) for optimum signal acquisition.

Acknowledgements

First and foremost, I would like to thank my supervisor Prof. Erika F. Merschrod S for giving me the opportunity to conduct my PhD program in her multidisciplinary research group and for her many valuable comments throughout my research especially in Chapter 3.

I would like to thank Prof. Yuming Zhao and Prof. Francesca Kerton who act as my supervisory committee and for reading the first draft of this thesis.

Indeed I am grateful to former and current members in the Merschrod research group for all the good times we spent and the scientific chats we had, especially Sandy Xu, Ramesh Kumar, Shahin Fatima and Liam D. Whelan. I thank Jordon Keats for teaching me the nanoindentation methodology and Prof. M. J. Clouter (Physics, Memorial University) for the use of and assistance with the metal evaporator. He trained me so well with his hand-made metal evaporator that with his help I was inspired to write a detailed manual for the device for the time of his retirement.

I also thank the people in the machine shop and electric shop, Bonnie and Steve in the Chemistry stores, David Murphy in the computer room and everyone in the general office of the Chemistry department, Viola, Mary, Ebony, Rosalind and Gina. Thank you to Nicholas Ryan and Joe Antle whom I assisted with their chemistry laboratory courses; I enjoyed working with them and learning from their teaching experience. I thank Dr. Wanda Aylward for the XRD analysis of mixed metal film

samples. Finally, I have a big thank you to my dear friend Saleh Riahi for being so enthusiastic about the subject of Raman study of oriented molecules. Whenever he found related examples in the literature he provided me with them and then we would have long discussions about the subject.

I take this opportunity to express my special thanks to my parents, Mohammad and Ashraf, specially my mom who cultivated my interest in science and helped me to set up my own chemistry laboratory in our basement when I was 12. As the last son I feel so fortunate for having my elder siblings Afshin and Houman. As brothers and good friends of mine their moral support have always been backing me up in all stages of my life particularly Houman during the course of my graduate studies overseas in Italy and Canada.

I have to thank my previous supervisors Dr. Carlo Giavarini, Dr. Paolo Goberti and Dr. Stefano Nascetti who supervised me during my second masters degree in polymer science and engineering (MASPENS) in Sapienza University of Rome joint with LyondellBasell, and my supervisors during my first masters program, Dr. Ali Hassanzadeh and Dr. Hossein Haghgooie, when I did my M.Sc. in Inorganic Chemistry.

Words are powerless to express my gratitude to what living in Newfoundland has offered me since 2009. To name a few: the chance to enjoy its intact beauty, its east coast hiking trails and the special weather which seems to be carved to calm my allergy to pollen and dust. I have found new life-long friends who I will forever be beholden to: Hanif Sedighnejad, Farzad Eskandari, Peyman Mahmoudifar, Dr. Ahmad Ghasemloonia, Yousef Pourghaz, Hilary Edison, Shirley Jones, Mrs. Radha Gupta and her beloved family, Dr. Veeresh Gadag and her beloved wife Rashmee Gadag, Dr. Thakor Patel, Ayesha Fiech and their families, and my great chemist fellows: Dr. Farzin Arjmand, my office mates Maryam B. Moghaddam and Yasaman

Jami Alahmadi for their love and support while I was writing up this thesis. Last but not the least was the chance to live with the most welcoming and warm hearted people on the earth –the Newfoundlanders.

Many thanks to Professor Benoit Champagne -the developer of the TDHF method within GAMESS-US for the analytical calculation of frequency-dependent Raman activities of free and oriented molecules- for his prompt feedback to my emails and for agreeing to have a Skype conversation which helped a lot in understanding the application of the TDHF method (in GAMESS-US) for calculating Raman signals of an oriented molecule.

This work was supported with funding from a Natural Sciences and Engineering Research Council of Canada Discovery Grant (materials), the Humber River Basin Project (materials and stipend), Canada Foundation for Innovation and the Research Development Corporation (instrumentation), and the Atlantic Innovation Fund (materials and stipends). Also I thank Compute Canada/Westgrid for the use of their computational resources and for their advice, and the School of Graduate Studies, Memorial University, for a graduate fellowship.

Table of Contents

Abstract **ii**

Acknowledgments **v**

List of Tables **xiv**

List of Figures **xix**

List of Abbreviations and Symbols **xxix**

1 Introduction **1**

1.1 Motivation for Raman based sensor development for *in situ* detection in water environments 1

1.2 Produced water monitoring 3

1.3 Surface enhanced Raman spectroscopy (SERS) 5

1.3.1 SERS-active metals and substrates 7

1.4 Intensity in normal Raman and SERS 8

1.5 Polarizability tensor and Raman tensor 10

1.6 SERS advantages and drawbacks 12

1.7 Ideal SERS substrate and substrate classifications 19

1.8 Sensing package and the application field 20

1.8.1 Motivation for substrate design: compatibility with application and mechanical properties of sensor package 21
1.8.1.1 Enhancing gold film adhesion/mechanical properties 23
1.8.2 Tailoring substrate surface features for better SERS signal with annealing approach 23
1.9 Atomic Force Microscopy 24
1.9.1 Force curves 25
1.9.2 Calibration of cantilever force constant 29
1.9.3 Roughness measurements 29
1.9.4 Thickness measurements 30
1.10 Overview of the thesis 31
Bibliography 31

Co-authorship Statement **40**

2 Improved Adhesion of Gold Thin Films Evaporated on Polymer Resin: Applications for Sensing Surfaces and MEMS **42**
2.1 Introduction 42
2.2 Experimental 44
2.2.1 Substrate Preparation 44
2.2.2 Metal Deposition 45
2.2.3 Mechanical Properties Measurements 46
2.2.4 Topography Measurements 47
2.3 Results 48
2.3.1 Scratch Tests 48
2.3.2 Indenting-Imaging Tests 49
2.3.3 Force Curves 50

2.3.4 AFM Topography Images 52
2.4 Discussion 53
2.5 Conclusions 56
Bibliography 56

3 Annealing Approach to Hot Spots for SERS Substrates: Applications to the Detection of Polycyclic Aromatic Hydrocarbons (PAHs) 60

3.1 Introduction 60
3.1.1 Objectives 64
3.2 Experimental 65
3.3 Results and Discussion 69
3.3.1 AFM, SEM, EDX and XRD 69
3.3.2 UV-Vis reflection spectra 71
3.3.2.1 Reflection intensity correlation with SERS; Au=42 nm/Cr=31 nm, 400 °C sample 73
3.3.2.2 Reflection intensity and maximum peak position; bilayer films 75
3.3.2.3 Reflection intensity; annealed vs. bilayer samples . . 76
3.3.2.4 Features in UV-Vis reflection spectra 77
3.3.3 Raman data 79
3.3.3.1 Identification of characteristic Raman peaks 79
3.3.3.2 Variability in CCC bending peak position 82
3.3.3.3 Variability in phenanthrene SER spectra 82
3.3.3.4 SERS enhancement 83
3.4 Conclusions 89
Bibliography 90

4 TDHF Study of Laser Field Directionality and Energy Effects on Raman Intensities of Oriented PAHs; With Applications to the Detection of PAHs with SERS **94**

4.1 Introduction 94

4.2 Methods 97

4.2.1 Definitions of orientation 98

4.2.2 Raman activities and intensities 101

4.3 Results 103

4.3.1 Altered laser field (polarization) directions 104

4.3.2 Altered laser energies 108

4.4 Discussion 112

4.4.1 Effect of altered laser field (polarization) directions 112

4.4.2 Effect of altered laser energies 114

4.5 Potential correlations between calculated and experimental Raman data seen for phenanthrene in Chapter 3 121

4.6 Conclusions 122

Bibliography 123

5 Conclusions **126**

5.1 Summary 126

5.2 Future directions 128

5.2.1 Roughness modification of the gold/SU-8 film system 128

5.2.2 Gold/SU-8 cantilever fabrication for biosensor applications . . 129

5.2.3 Aiming for further modification of islands of gold and chromium 130

5.2.4 Raman spectroscopy of molecularly imprinted polymers with analyte 130

5.2.5 Implementation of MIP films on a flat substrate with Raman microscopy and SERS . . . 132
Bibliography . . . 134

A Supplementary information for "Improved Adhesion of Gold Thin Films Evaporated on Polymer Resin: Applications for Sensing Surfaces and MEMS" 137
A.1 Example force curve . . . 137
A.2 Calibration of the cantilever force constant . . . 139
A.3 Thickness measurement . . . 140
Bibliography . . . 140

B Supplementary information for SU-8 polymer resin 142
Bibliography . . . 144

C Supplementary information for "Annealing Approach to Hot Spots for SERS Substrates: Applications to the Detection of Polycyclic Aromatic Hydrocarbons (PAHs)" 145
C.1 AFM . . . 145
C.2 Bands in UV-Vis reflection spectra . . . 147
C.3 UV-Vis instrumentation details . . . 147
C.4 Solubility limits and other physical properties of phenanthrene . . . 151
C.5 Raman . . . 151
C.5.1 Laser power . . . 154
C.5.2 Laser spot . . . 154
C.5.3 Optical density . . . 155
Bibliography . . . 155

D Supplementary information for "TDHF Study of Laser Field Directionality and Energy Effects on Raman Intensities of Oriented PAHs; With Applications to the Detection of PAHs with SERS" 157

D.1 Sample input file for an ordinary Raman calculation 157

D.2 Sample input file for a dynamic Raman calculation 163

D.3 Raman tensors for selected modes of confined naphthalene and phenanthrene molecules 174

Bibliography 176

List of Tables

1.1 This table shows the SERS studies with multicomponent PAHs solutions which contain phenanthrene and the study from this thesis. Concentrations are given here for detected phenanthrene. 5

1.2 Raman spectral wavenumbers and vibrational assignments for tetracene under different laser energies. The values accompanied with the abbreviations are Raman energy shifts in cm^{-1}. Column titles in bold represent the laser wavelength of the Raman instrument. s, strong; m, medium; w, weak; sh, shoulder; w sh, weak shoulder (used with permission from [59]). 16

1.3 Raman spectral wavenumbers and vibrational assignments for phenanthrene under different laser energies. The values accompanied with the abbreviations are Raman energy shifts in cm^{-1}. Column titles in bold represent the laser wavelength of the Raman instrument. v st, very strong; st, strong; m, medium; w, weak; v w, very weak; sh, shoulder; wsh, weak shoulder; m sh, medium shoulder; st sh, strong shoulder (used with permission from [59]). 17

2.1 Average indentation depths, elastic moduli and stiffness for each sample. Statistical information about these averages is provided in the text and in Figure 2.3. 50

2.2 Roughness values for 12 nm thick gold films on pre- and post-deposition-cured samples with different thickness of SU-8 underlayer. For comparison, the roughness measured for gold film without an SU-8 underlayer was 1.42 nm. Roughness data are calculated over 10x10 μm scan area. 53

3.1 Wavelength of maximum reflection (λ_{max}) for bilayer films. There is a blue-shift as the gold layer thickness increases. 78

3.2 Raman peak heights (for CCC bending), roughnesses, and surface areas for different SERS substrates. The calculated increased surface areas and the SERS enhancements are also tabulated. The roughness and surface area are obtained from a 20x20 μm AFM scan except for the marked ones where 5x5 μm scan was used. The Raman enhancement ratios for annealed samples of Au=42 nm/Cr=31 nm are calculated relative to their parent as-deposited bilayers using Equation 3.2 as explained in the text. Peak height values are from SERS data for substrates which were submerged in 0.01 mg/L phenanthrene solutions. Roughness data are calculated by averaging over four areas across each scan. 87

4.1 Intensities of naphthalene modes that show significant changes under different laser conditions (polarized and unpolarized), calculated with the 6-31G(d,p) basis set and ω = 0.04 hartree (IR). The values in parentheses are percentages with regard to the most intense mode. . . 106

4.2 Raman activities of phenanthrene modes that show significant changes under different laser conditions (polarized and unpolarized), calculated with the 6-31G(d,p) basis set and $\omega = 0.04$ (IR). The values in parentheses are percentages with regard to the most intense mode. 108

4.3 Effect of the laser energy on Raman activities for naphthalene. The values in parentheses are Raman activity coefficients as a percentage of the most intense mode. 109

4.4 Effect of the laser energy on Raman activities of phenanthrene. The values in parentheses are Raman activity coefficients as a percentage of the most intense mode. 109

4.5 Comparison of calculated Raman activities and experimental Raman intensities for phenanthrene. Experimental Raman results show an increase in signal strength when the laser wavelength was altered from 1064 nm to 532 nm. For comparison purposes the calculated Raman activities for 1139 and 536 nm wavelengths are provided. Calculated Raman frequencies are scaled by a factor of 0.905 [19, 30]. Symmetry assignments are provided by ordinary Raman calculation by GAMESS-US. Vibrational assignments are mostly the ones proposed by Alajtal *et al.* (in bold), while some are done by mode visualization with Macmolplt to help with associating experimental Raman shifts more accurately to the calculated frequencies. The notations represent the strength of the observed Raman intensities (v st, very strong; st, strong; m, medium; w, weak; v w, very weak; sh, shoulder; w sh, weak shoulder; m sh, medium shoulder; st sh, strong shoulder). stch stands for stretching. 116

A.1 MikroMasch manufacturer cantilever specifications for NSC35/AlBS (tip B) and comparison to measured force constant (thermal method) and resonance frequency. **Manufacturer** column presents the expected specification range provided by manufacturer (nominal values). **Measurement** shows the actual values which were obtained experimentally 139

D.1 Important naphthalene modes, their activities, and the first derivatives of their transition polarizabilities under altered laser field directions, calculated with TDHFX using the 6-31G(d,p) basis set and $\omega = 0.04$ hartree (IR). The activities are also given as percentages of the most intense mode (in parentheses). All modes listed here are of a symmetry. 166

D.2 Important naphthalene modes, their activities, and first derivatives of transition polarizabilities under unpolarized incident light calculated with TDHFX method using the 6-31G(d,p) basis set and $\omega = 0.04$ hartree (IR). The values in parentheses are Raman activity coefficients relative to the most intense mode presented as percentages. 167

D.3 Important phenanthrene modes, their activities, and the first derivatives of their transition polarizabilities under altered laser field directions, calculated with TDHFX using the 6-31G(d,p) basis set and $\omega = 0.04$ hartree (IR). The activities are also given as percentages of the most intense mode (in parentheses). All modes listed here are of a_1 symmetry. 168

D.4 Important phenanthrene modes, their activities, and first derivatives of transition polarizabilities under unpolarized incident light calculated with TDHFX method using the 6-31G(d,p) basis set and $\omega = 0.04$ hartree (IR). The values in parentheses are Raman activity coefficients as a percentage of the most intense mode. 169

D.5 Effect of the laser field ($\omega = 0.04$ hartree) polarization direction on the Raman activities of naphthalene. The values in parentheses are Raman activity coefficients as a percentage of the most intense mode. 170

D.6 Effect of the laser field ($\omega = 0.04$ hartree) polarization direction on the Raman activities of phenanthrene. The values in parentheses are Raman activity coefficients as a percentage of the most intense mode. 171

D.7 Raman tensor components of confined naphthalene for modes that show significant Raman activity changes under various laser polarization directions, calculated with the 6-31G(d,p) basis set and $\omega = 0.04$ hartree (IR). 175

D.8 Raman tensor components of confined phenanthrene for modes that show significant Raman activity changes under various laser polarization directions, calculated with the 6-31G(d,p) basis set and $\omega = 0.04$ hartree (IR). 175

List of Figures

1.1 A typical SERS based microfluidic sensor device. Metal thin film, plastic and insulator boundaries coexist to shape a functional SERS sensor package. 3

1.2 Schematic diagrams of Raman scattering and fluorescence. (a) Typical vibration/Q-displacement and its interaction with the incident laser resulting in inelastic scattering at frequencies above or below the laser frequencies. (b-Fluorescence) A wide fluorescence band as a consequence of an electronic transition. (b-Raman) Normal Raman *vs.* resonance Raman where the molecule is excited to virtual or real excited states respectively, and a Raman spectrum (used with permission from [37]). 13

1.3 Schematic of SERS substrates: different shaped metal nanoparticle colloids or films, metal coated nanospheres, random nanostructures coated with a metallic thin film, or metal nanoparticles mixed within a polymeric coating (used with permission from [68]). 21

1.4 AFM cantilever/probe/substrate manufactured by micromachining of Si or Si_3N_4. The words "probe" and "tip" are used interchangeably to convey the same concept. (Not drawn to scale.) 25

1.5 Schematic of the optical lever sensor. As a result of cantilever deflection, the reflected laser spot on the detector moves. Since the distance between the cantilever and the detector d is large, a tiny deflection of the cantilever results in a large position displacement of the laser spot at the detector. (Not drawn to scale.) 26

1.6 The top camera view from a progressive load scanning measurement with a silicon cantilever/probe. The black body at the left is the chip with the cantilever. The probe is at the right most part of the cantilever and it is not visible because it is below the cantilever. The blue light on the cantilever is the laser bouncing back to the detector. The orangish surface under the probe is the gold thin film. The black line in the vicinity of the cantilever is the resulting scratch due to a high applied load of the probe on the thin film during scanning. 26

1.7 A schematic force curve. The red segment is the extension part (load part) of the force curve in which the tip approaches the surface and then snaps to the surface due to attractive forces overcoming the cantilever stiffness; after this point the indentation starts where the loaded force increases up to the set point and then the tip retracts where the blue segment (unloading part) starts and ends where the load section started. 28

2.1 Line profile (perpendicular to the fast scan direction) across the deflection retrace image that is obtained while the set point voltage is manually increased. The post-deposition-cured sample requires a much higher applied force (and hence tip deflection) before film disruption (scratching) occurs. 49

2.2 Contact mode images after indentation tests for a post-deposition-cured sample (**a**) and a pre-deposition cured sample (**b**). Image (b) shows streaking: gold prepared with pre-deposition curing is so fragile that when the tip reaches the indented area it starts to scratch. In contrast, indentations could be clearly imaged for post-deposition-cured sample (a). 50

2.3 Box plots for elastic modulus (**a**) and stiffness (**b**) values calculated for each sample. The average elastic moduli for the two sample types are not significantly different, but the stiffness for the post-deposition-cured sample is significantly higher. The circles are outliers. 51

2.4 AFM images for gold films prepared by the (**a**) post-deposition-cured recipe and (**b**) pre-deposition cured recipe on 20 μm thick SU-8 layers. The morphologies and hence roughness values are different. 52

3.1 Schematic of the reflection setup. The light source sends UV-Vis light through the input leg of the reflection probe to the sample (bottom of the figure). The reflection probe holder holds the probe firmly at a 45 degree angle with respect to the surface. The output leg of the reflection probe collects scattered light at the same angle. (Not drawn to scale.) 68

3.2 AFM height channel image of a gold-chromium annealed film, showing regularly-spaced and -sized islands. 71

3.3 SEM images of the a) gold on a chromium bilayer and b) gold-chromium annealed films. The contrast variations in b show segregated regions. The arrows 1, 2, and 3 point to a gray, dark, and bright region (gold island) respectively. Representative EDX spectra of these three regions are shown in Figure 3.4. 72

3.4 EDX spectra show gold content of three regions in an annealed film based on the M line X-ray at 2.120 keV. The strong oxygen Kα line X-ray at 0.525 keV does not allow the detection of the adjacent chromium Lα line X-ray at 0.573 keV. Other elemental signals come from the underlying glass substrate. This could be correspondingly seen in the elemental map in Figure 3.5. 73

3.5 Elemental map of an annealed sample in the same field presented in SEM image in Figure 3.3b. a) The green dots show gold distribution in the annealed film. (M line, 2.120 keV signal); b) The red dots show chromium distribution along the same image. This shows chromium is present in all three regions. (Kα line, 5.411 keV signal) 74

3.6 XRD pattern of a Au=42 nm/Cr=31 nm film annealed at 400 °C for 2 hours (2 h). All peaks correspond to Au, with arrows indicating peaks which also coincide with Cr. 75

3.7 UV-Vis reflection spectra of bilayer films and a single layer gold film (smoothed data). The reflection of bilayer films correlates with the gold thickness. 76

3.8 UV-Vis reflection spectra of films annealed at 400 °C for 1 hour (1 h) or 2 hours (2 h) (smoothed data). Annealed films show higher intensity reflection. 76

3.9 Raman spectrum of chromium oxide film which is normalized to its Cr_2O_3 A_{1g} peak intensity (used with permission from [29]). 84

3.10 SERS activity of as deposited bilayer films and the single layer gold film. Substrates were submerged overnight in a 0.01 mg/L phenanthrene solution in ethanol. The single layer gold film provides the highest enhancement for the CCC bending among the others. The SER intensity with different substrates correlates with their UV-Vis spectra intensity. 85

3.11 SERS activity of Au=21 nm/Cr=14 nm and Au=42 nm/Cr=31 nm samples annealed at 325 °C for 1 hour (1 h) showing that the sample with the thicker initial gold layer gives higher enhancement. CCC bending peak positions are at 546 cm^{-1} for the former and at 541 cm^{-1} for the latter along with a peak at 298 cm^{-1} which can be related to PAH-Cr. Both substrates here were immersed in a 0.01 mg/L solution of phenanthrene in ethanol overnight. 85

3.12 SERS activity comparison for Au=42 nm/Cr=31 nm as-deposited bilayer sample and its variously annealed counterparts, all being exposed to a phenanthrene solution of 0.01 mg/L in ethanol overnight. 1 h and 2 h in the annotations mean annealed for 1 hour and 2 hours respectively. The Raman spectrum for the 400 °C, 2 h sample is offset downward to fit in the plot. Positions of CCC bending peak from top to bottom are 544 cm^{-1}, 542 cm^{-1}, 541 cm^{-1}, 556 cm^{-1}, 551 cm^{-1}, and no CCC bending peak for glass slide. Also seen for 400 °C, 2 h sample is a peak at 300 cm^{-1} which can be related to PAH-Cr. 86

3.13 The Au=42 nm/Cr=31 nm sample annealed at 400 °C for 2 hours (2 h) shows sufficient SERS activity for detecting the analyte (phenanthrene) at various concentrations when immersed in ethanol solutions for 5 seconds. CCC bending peak positions from top to bottom are similar (543 cm^{-1}, 548 cm^{-1}, and 548 cm^{-1}.) 88

3.14 Experimental normal Raman spectra (not SERS) for solid phenanthrene and its 10 mg/L solution (in ethanol) collected with 532 nm laser excitation using a 50X objective lens and 2 acquisitions, each of 6 seconds. One spectrum is obtained with 60 seconds of exposure time to obtain higher signal to noise ratio for the solution. 89

4.1 Naphthalene orientation with regard to the Cartesian coordinates. This is an orientation based on the master frame rules for GAMESS-US for a molecule with D_{2h} symmetry. 99

4.2 Phenanthrene orientation with regard to the Cartesian coordinates. This is an orientation based on the master frame rules for GAMESS-US for a molecule with C_{2v} symmetry. 99

4.3 Molecule-laser field interaction geometry with an x-polarized laser for (a) oriented naphthalene and (b) oriented phenanthrene. The incident laser could be also y or z polarized. Note the different orientations which are required to match the master frame rules for GAMESS-US for molecules of different symmetry. 100

4.4 Raman intensities for naphthalene for varying laser field direction and unpolarized incident light when $\omega = 0.04$ hartree (1.09 eV). Each relative intensity (in percentage) is associated to a Gaussian fit (FWHM = 4 cm^{-1}), the area under which is equal to that percentage value. . 105

4.5 Raman intensities for phenanthrene for varying laser field direction and unpolarized incident light when $\omega = 0.04$ hartree (1.09 eV). Each relative intensity (in percentage) is associated to a Gaussian fit (FWHM = 4 cm^{-1}), the area under which is equal to that percentage value. . 107

4.6 Raman intensities for naphthalene for laser field energies $\omega = 0.04$ hartree (1.09 eV) and $\omega = 0.085$ hartree (2.31 eV) and for a static field. Each relative intensity (in percentage) is associated to a Gaussian fit (FWHM = 4 cm^{-1}), the area under which is equal to that percentage value. 110

4.7 Raman intensities for phenanthrene for laser field energies $\omega = 0.04$ hartree (1.09 eV) and $\omega = 0.085$ hartree (2.31 eV) and for a static field. Each relative intensity (in percentage) is associated to a Gaussian fit (FWHM = 4 cm^{-1}), the area under which is equal to that percentage value. 111

4.8 Depicted vibration mode at 1487 cm^{-1} for naphthalene. This vibration mode shows higher Raman activity under x-polarized laser. Refer to Table 4.1 for the Raman activity values calculated under different electric field directions. 114

4.9 Depicted vibration mode at 1782 cm^{-1} for naphthalene. This vibration mode shows higher Raman activity under y-polarized laser. Refer to Table 4.1 for the Raman activity values calculated under different electric field directions. 115

5.1 Schematic of MIP formation. N,O-bismethacryloyl ethanolamine (NOBE), which is both the cross linker and the monomer, polymerizes around the template molecule. When the MIP is formed, the last step is to wash the template away in order to leave a binding cavity which selectively captures the template molecule. 132

A.1 A typical force curve from the post-deposition-cured sample 138

A.2 Magnified view of the same force curve from the post-deposition sample, showing the region fitted to calculate adhesion and elastic modulus . 138

A.3 The picture illustrates the sample holder of the metal evaporator device (after a metal deposition run) on which glass slides are mounted. The circled sample shows a glass slide which was partially masked by tape to avoid metal deposition on the edge of the slide. This is in order to create a clear metal thin film boundary on the glass slide for the purpose of subsequent thickness measurements with AFM. 140

B.1 When exposed to UV light followed by thermal treatment, SU-8's long molecular chains join from their epoxy group ends. This results in SU-8 hardening. 143

B.2 Gold thin film fabricated on an SU-8 cast glass slide according to the proposed recipe. When exposed to UV light followed by thermal treatment, SU-8 hardens and shrinkage of the polymeric layer results in a rough top gold layer. The top gold layer thickness is 10 nm and SU-8 thickness is 10 μm 144

C.1 AFM tapping mode images. Each row presents a bilayer as-deposited Au/Cr sample along with its corresponding various thermally treated counterparts with their roughness value mentioned below each image. All images are 20x20 μm except as-deposited Au=21 nm/Cr=14 nm (a), Au=42 nm/Cr=31 nm (f) bilayer films and Sample 2, 400 °C, 1 h (i) which are 5x5 μm. The z colour-scale for all images is 0-80 nm as shown in image (a). Thermally treated samples reveal the change in morphology and roughness. For example surface features for samples annealed for 2 hours (2 h) at 400 °C are larger in comparison to the samples annealed for 1 hour (1 h) at the same temperature. The same trend is seen for their roughness. Roughness data are calculated by averaging over four areas across each scan. 146

C.2 Original UV-Vis reflection spectra (without smoothing) of bilayer films and a single layer gold film. The reflection property of bilayer films correlates with the gold thickness. 148

C.3 Original UV-Vis reflection spectra (without smoothing) of films annealed at 400 °C for 1 hour (1 h) or 2 hours (2 h). 148

C.4 The R200-MIXED reflection/backscattering probe for expanded wavelength coverage. The leg which goes to the light source consists of 12 optical fibers, 6 for UV-Vis and 6 for VIS-NIR. The UV-Vis leg can carry the signal in the range of 200–750 nm. The other leg carries the signal in the 450–100 nm range. Only one leg at a time can be connected to the spectrometer. In experiments performed here in this thesis the UV-Vis leg was used. 149

C.5 The R200-MIXED reflection/backscattering probe is for expanded wavelength coverage. The diameter is 0.25 in (6.35 mm). This is almost four times the diameter of the inner circle which contains the optical fibers. Hence the diameter of the circle on the sample which is illuminated by probe could be estimated to be roughly in the range of 1.6–6.35 mm. 150

C.6 Raman spectra of solid phenanthrene obtained with 1064, 785, 633 and 514 nm lasers (used with permission from [6]). 152

C.7 The Au=42 nm/Cr=31 nm sample annealed at 400 °C for 2 hours (2 h) shows sufficient SERS activity for detecting the analyte at different concentrations when immersed in ethanol solutions for 5 seconds. These spectra are the same spectra presented in Figure 3.13 but with a larger window for wavenumber shift values on the x axis. 153

D.1 Schematic of the geometry assumed by GAMESS-US in the TDHFX method for the dynamic Raman calculation of a free molecule using the "ALLDIRS" keyword. The red and green arrows are light scattered parallel and perpendicular to the direction of polarization of the incoming laser respectively. 163

List of Abbreviations and Symbols

PW	Produced water
PAHs	Poly cyclic aromatic hydrocarbons
LSPR	Local surface plasmon
SERS	Surface enhanced Raman spectroscopy or scattering
EBL	Electron beam lithography
SU-8	photosensitive polymer in common use as a structural material
PLS	Progressive load scratch
PLST	Progressive load scratch test
QCM	Quartz crystal microbalance
SPR	Surface plasmon resonance
AFM	Atomic force microscope
QTM	Quad triangle method
SEM	Secondary electron microscopy
EDX	Energy dispersive X-ray spectroscopy
XRD	X-ray diffraction
UV-Vis	Ultraviolet-visible
h	Hour
Au/Cr	A bilayer film made of Au layer on top of Cr layer deposited on a support e.g. glass

MEMS	Microelectromechanical systems
NIR	Near infrared
IR	Infrared
TDHF	Time-dependent Hartree-Fock
MIP	Molecularly imprinted polymer

Chapter 1

Introduction

1.1 Motivation for Raman based sensor development for *in situ* detection in water environments

There is considerable current interest in methods of fast detection of chemicals, including water contaminants either for monitoring discharges from industry or any site affected by humans, to meet regulatory standards and to preserve watershed health [1–5]. Water composition measurements (physical, chemical, biological and ecological) require periodic sampling and later analysis in off-site laboratories. The measurements done later may not provide *in situ* information [6]. In addition, if a problem is identified from these analyses, any effective reaction to address the contamination source is delayed due to the time lapse between sampling and analysis.

In the case of produced water (PW)* from offshore petroleum installations, industry has the incentive to monitor components in discharged water because the

*Produced water is the sum of the reservoir water and the additional water which is injected into the reservoir to force the oil or gas to the surface [7].

chemistry of the produced water can be an indicator of the efficacy of earlier stages in the process stream [8]. Although much has been done regarding the enhancement of speed and sensitivity of analytical methods, there is still a need for rapid sampling and detection of water quality.

Current practices for online monitoring of polycyclic aromatic hydrocarbons (PAHs) from produced water in water typically involve fluorescence measurements, which can also provide an estimate of total hydrocarbon content [9]. However, fluorescence measurements cannot provide details about molecular size and functionality. Raman spectroscopy is an excellent choice for signal detection to sense not only organic species, but also inorganic compounds with very high specificity in an aqueous environment [10]. With the arrival of surface-enhanced Raman spectroscopy (SERS), which uses nanostructured metal features to boost the signal of analytes [11], Raman has become more appealing and is finding more applications in sensing, including environmental monitoring of aqueous and airborne organic and inorganic contaminants and pathogens [12–14].

This work, using simple and cost effective approaches, is intended to establish the groundwork required for sensing with SERS (to be applied in future development of SERS-based microfluidic sensors) to be ultimately adopted by the oil industry for online fast water quality monitoring for detection of hydrocarbons. Figure 1.1 shows a schematic of a SERS-based microfluidic sensor device, wherein the cold-ocean contaminated water flows in a micrometer-sized channel. Within the channel, the analyte species interact with the SERS active metal layer and hence the trace concentration can be detected with Raman spectroscopy. The results of this thesis could be beneficial for fabrication of such a sensing package. This includes fabrication of the robust metal layer, the SERS active metal film with a tendency to engage the hydrocarbon on the surface, and in-advance Raman calculations which help with the

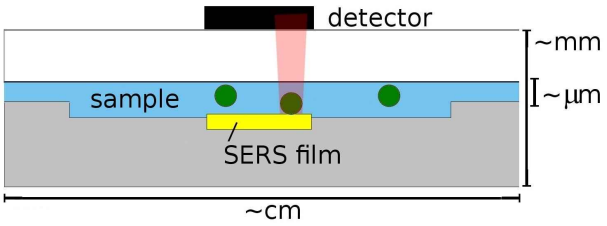

Figure 1.1: A typical SERS based microfluidic sensor device. Metal thin film, plastic and insulator boundaries coexist to shape a functional SERS sensor package.

design of the ultimate package.

In addition to the impact on the offshore petroleum sector, this work will also be of benefit to aquaculture and fisheries, given the extensive evidence for impact of PW on the health of marine organisms, including the Atlantic cod [15].

1.2 Produced water monitoring

Produced water is composed of dispersed and dissolved chemicals from fossil fuels and the geological reservoir that accommodates the formation water (water that exists with the oil reservoir) [16]. PW consists of dispersed oil, semi-soluble hydrocarbons: benzene, toluene, ethylbenzene and xylenes (BTEX), polycyclic aromatic hydrocarbons (PAHs), organic acids, phenol, and alkylated phenols. PW also contains small concentrations of chemical additives from the production/separation process, along with inorganic compounds and natural low-radioactive elements from geologic reservoir water [7, 16].

PAHs, and more specifically 2- and 3-ring PAHs, are the most significantly hazardous components of produced water discharge, where the hazards are defined as having a potential negative impact on the ecology [16, 17]. PAHs' solubility limits in seawater fall in the range of μg/L to mg/L; the value for phenanthrene is 0.6 mg/L [18]. Their health hazard is due to their induction of carcinogenesis. A study

by Flaveny and Perdew confirmed that rodents, when exposed to PAHs, would show hepatomegaly, immune disruption, reproductive, developmental and neurological defects as well as cancer [19]. In fish, uptake of PAHs lead to birth defects, reduced growth, cranial facial malformations, yolk sac and pericardial edema, and subcutaneous hemorrhaging [20], hence their monitoring is an important matter.

Many efforts have been made to develop methods for PAHs identification and quantitation in soot, water and soil. For many years, the most common chemical analysis methods have been gas chromatography-mass spectrometry (GC-MS) and fluorescence for determination of the PAH content of produced water. Sample preparation is needed before these analyses which costs time and money [7,9,21–23]. SERS does not have this requirement which nominates it as a pioneering technique to detect PAHs in water environments [23]. Numerous research projects have studied the applicability of the SERS technique for PAH detection in solutions and each has targeted a particular PAH or group of PAHs. These studies have all been conducted in laboratory scales on alcoholic [24–26] or aqueous solutions [27–29] and only a few of them have considered phenanthrene among their target molecules (see Table 1.1).

Leyton *et al.* use the SERS effect from carbon nanotube assemblies between the metallic surface and the analytes to detect pyrene as a model PAH at concentrations in the limit of 2 μg/L (10^{-9} mol/L) [30]. SERS has been applied by Schmidt *et al.* for a mixture of five PAHs, including phenanthrene, dissolved in artificial seawater [27]. Pfannkuche *et al.* performed SERS and GC-MS measurements of polluted seawater in the Gulf of Gdansk in order to gauge SERS quantitative power for detection of PAHs in real samples [13]. They concluded that SERS could be used as a non-quantitative alarm sensor in highly polluted waters ([PAH]$>$ 150 ng/L). Du and Jing, using a novel substrate based on thiol-functionalized Fe_3O_4@Ag core-shell magnetic nanoparticles for SERS, reported detection limits of 5 mg/L and 50 mg/L respectively

for phenanthrene and naphthalene [24].

Table 1.1: This table shows the SERS studies with multicomponent PAHs solutions which contain phenanthrene and the study from this thesis. Concentrations are given here for detected phenanthrene.

	Detected concentration	Sample	Substrate
Schmidt *et al.*	8.6 μg/L	seawater solution[a]	immobilized Ag colloid
Olson *et al.*	18 μg/L	aqueous solution[b]	functionalized Au colloid
Du and Jing	5 mg/L	ethanolic solution[c]	functionalized nanomagnets
This thesis	10 μg/L	ethanolic solution	mixed Au-Cr islands

[a] [27] naphthalene, fluorene, phenanthrene, fluoranthene, pyrene and anthracene

[b] [31] naphthalene, phenanthrene and pyrene

[c] [24] perylene, benzo-[a]pyrene (BaP), pyrene, anthracene and phenanthrene

An Analyte can only be detected by Raman if it comes in proximity of the SERS-active substrate (see Section 1.3.1). Due to their hydrophobic nature, PAHs have a very low solubility in water and low affinity to metallic surfaces [25]. This issue has been addressed by functionalization of metallic surfaces with a variety of hydrophobic molecular monolayers. As described above, Du and Jing [24] use 1-pentanethiol to functionalize their nanoparticles. Olson *et al.* [31] use a layer of alkylsilane (C18) molecules to further assist PAHs adsorption from aqueous solutions. This thesis proposes a new approach in which chromium serves as the entity with affinity to bind phenanthrene. The chromium is annealed with thin layers of gold as the SERS-active metal to give Au-Cr islands which could produce a SERS-active substrate.

1.3 Surface enhanced Raman spectroscopy (SERS)

SERS is a surface-sensitive event which results in enhanced Raman scattering when molecules settle at or near the surfaces of certain nanostructured coinage metals [11,

32–35]. The term SERS was coined by Van Duyne [36]. The primary enhancement factor is around a million-fold in comparison to normal Raman signals from non-adsorbed molecules [33,34]. The phenomenon was first observed by Fleischman in 1974 and was related, at the time, to the high density of the roughened silver electrode surface where pyridine molecules were adsorbed [32]. It was later realized [33, 34] that this enhanced signal was not dependent on the concentration, and neither could the small increase in the surface area of the silver electrode due to roughening have resulted in the million fold signal increase. Hence, signal enhancement was related to the adsorbed molecules' unique interactions with the metal surface. These unique interactions somehow impacted the Raman scattering of these adsorbed molecules.

This process has been explained by two accepted mechanisms. The first one, proposed by Jeanmaire and Van Duyne in 1977, states that the electromagnetic contribution from the noble metal surface based on the metal surface plasmon excitation with laser light is responsible for signal enhancement [33]. This leads to a large localized electromagnetic field in the vicinity of the surface, which is known as a hot spot [37]. The second mechanism, introduced by Albrecht and Creighton again in 1977, [34] proposes a chemical interaction due to charge transfer or bond formation between the adsorbed molecules and the metal that leads to a high molecular scattering cross-section. These two works demonstrated a new discovery regarding light and matter interaction. The most recent model was proposed by Lombardi as a unified view of surface-enhanced Raman by combining three types of resonances leading to the surface-enhanced scattering effect: the surface plasmon resonance in the metal nanostructure, a charge-transfer resonance as a result of electron exchange between the molecule and the conduction band of the metal, and molecule-specific resonances [38].

1.3.1 SERS-active metals and substrates

Xia *et al.* described optical properties of metallic nanostructures, explaining how a metallic nanostructure can carry SERS activity [39, 40]. According to their explanation, when metal is exposed to the incident laser, the free electrons start to oscillate with the laser's electric field, which is known as surface plasmon resonance (SPR). The collective oscillations of these free electrons results in a plasmon band. Peaks in the extinction spectra (extinction = scattering + absorption) are due to these collective oscillations, with specific values of λ_{max} which are specific to the metal. The peak position is also impacted by nanostructure in the metal, which leads to the color of metal colloids [39].

The polarized surface charges under the laser excitation in a nanoparticle cannot propagate as a wave as they would on a flat surface [40]. This is due to the incomparable length scales of the VIS-NIR laser wavelength in the range of 512 to 1064 nm (large) and the small nanoparticle in the range of 10–80 nm*. Hence the induced charges are localized, leading to the name localized surface plasmon resonance (LSPR) [39]. LSPR generates strong local electric fields within 10–50 nm of the surface of the nanoparticle depending on size, shape and local environment [39]. As a consequence of this, molecules adsorbed to or residing near the particle surface will show enhanced Raman scattering [40].

Since the discovery of SERS, localized fields in metals other than coinage metals, such as Li, Na, K and In, have been shown to demonstrate the SERS effect with incident laser energy in near or in the visible region [42, 43].

The common property that nominates these metals for SERS is that their plasmon band energy is in the energy range of typical lasers (532–1064 nm). For example, SERS enhancement with Pd substrates is low because light absorption/scattering occurs for

*The typical admissible size for SERS experiments is in the range of 10 to 80 nm [41].

this metal only in the UV region [40].

1.4 Intensity in normal Raman and SERS

In the classical view of light scattering, Raman scattering could be defined as a secondary emission (secondary is defined in contrast to the incident laser which is considered as the initial) developed from the molecule as a consequence of light inducing a dipole in the molecule. The electric field of the incident light E distorts the polarizable electron clouds. The extent of the distortion depends on the atom types in the molecule and on the types of bonds (single, double and triple). This interaction creates an induced dipole moment P in the molecule. The magnitude of P (induced dipole moment) relies on the polarizability, α, of a specific molecule and also on the electric field E of the incident light:

$$P = \alpha E \tag{1.1}$$

Since E is an oscillating field rather than being a static electric field, the induced dipole will oscillate with the same frequency as the light does:

$$P = \alpha E_0 cos(2\pi\nu t) \tag{1.2}$$

where ν is the frequency of the incident light and E_0 is the maximum amplitude. In this view, an oscillating dipole radiates at the same frequency as the incident light. The mean rate of total radiation by such a dipole is represented in Equation 1.3 [44]:

$$I = \frac{16}{3}\frac{\pi^4\nu^4}{c^3}P^2 \tag{1.3}$$

where c is the light speed, ν is the frequency of the incident light and P is the induced dipole. This equation could also be written as

$$I = \frac{16}{3}\frac{\pi^4\nu^4}{c^3}\alpha^2E^2 \tag{1.4}$$

The outcome from Equation 1.4 is that the more intense the incident radiation and the more polarizable the molecule, the higher the intensity of the Raman band since I is directly proportional to E^2 and α^2.

One can also think of the polarizability of particular vibrational modes. The scattering molecule has its own specific vibrational coordinates Q which could be defined by Equation 1.5, in which ν_k is the vibrational frequency and Q_k^0 is the bond length at equilibrium [44]:

$$Q_k = Q_k^0 cos(2\pi\nu_k t) \tag{1.5}$$

As a consequence, the polarizability α is affected by these vibrations as defined in Equation 1.6, where α_0 is the polarizability at the equilibrium position [44].

$$\alpha = \alpha_0 + \left(\frac{\partial\alpha}{\partial Q_K}\right)_0 Q_k + \text{higher order modes} \tag{1.6}$$

The combination of Equations 1.2 and 1.6 defines P (Equation 1.7) as a function of the vibrational frequency. Hence the induced dipole moment from the incoming electric field is also regulated by these vibrations as expressed in Equation 1.7:

$$P = \left[\alpha_0 + \left(\frac{\partial\alpha}{\partial Q_K}\right)_0 Q_k^0 cos(2\pi\nu_k t)\right] E_0 cos(2\pi\nu t) \tag{1.7}$$

As a result, the induced dipole oscillates with the same frequency as the incident light field and also at shifted frequencies different from the incoming light frequency by $\pm$ molecular vibrational frequency (ν_k) as seen in Equation 1.8 [44], a rephrased form

of Equation 1.7. These shifted oscillations in the secondary emission (scattered light) are called Stokes and anti-Stokes:

$$P = \alpha_0 E_0 cos(2\pi\nu t) + \frac{1}{2}\left(\frac{\partial\alpha}{\partial Q_K}\right)_0 Q_k^0 E_0 \left[cos2\pi(\nu+\nu_k)t + cos2\pi(\nu-\nu_k)t\right] \quad (1.8)$$

Figure 1.2 (a) shows schematic diagrams of Stokes and anti-Stokes Raman scattering.

Looking at Equation 1.4 we can gain insight into SERS enhancing mechanisms. Basically SERS happens because some mechanisms lead to an increase of E or α or both together, which ultimately results in an increase of I (Raman intensity enhancement). The two famous mechanisms which lead to the SERS effect could be described based on this classical view. In this regard the electromagnetic mechanism suggests the amplification of the local electric field E in which laser excitation is responsible for SERS signal enhancement [42]. In the chemical enhancement mechanism, the molecular polarizability α increases as a consequence of charge transfer between the metal surface and the adsorbate that is responsible for signal enhancement [45].

1.5 Polarizability tensor and Raman tensor

Polarizability is a second-rank tensor since it relates the electric field and induced dipole moment, both of which are vectors. If the polarizability tensor of the molecule is spherically symmetric then the molecular polarizability could be defined in this way:

$$\vec{P} = \alpha\vec{E} \quad (1.9)$$

where $\vec{P}$ and $\vec{E}$ are the molecular dipole moment and the electric field vector of the incident light in three-dimensional space, respectively. However, since the polarizability tensor is not spherically symmetric the equation above will be written as the

following:

$$\vec{P} = [\alpha]\,\vec{E} \tag{1.10}$$

where $[\alpha]$ is the tensor expression of the polarizability (the polarizability tensor) [46].

The Raman tensor is defined as the differential of the polarizability tensor which was first introduced by Ovander [47] in 1960. Similarly it is a second-rank tensor and may be given as $[\alpha']$. If the principal axes of the Raman tensor are defined as x-, y- and z-axes, the tensor is shown as

$$[\alpha'] = \begin{pmatrix} \alpha'_{x,x} & \alpha'_{x,y} & \alpha'_{x,z} \\ \alpha'_{y,x} & \alpha'_{y,y} & \alpha'_{y,z} \\ \alpha'_{z,x} & \alpha'_{z,y} & \alpha'_{z,z} \end{pmatrix} \tag{1.11}$$

This Raman tensor belongs to an individual vibrational mode of the molecule and is usually assumed as an ellipsoid. It is the interaction between the electric field vector of the incident light and this ellipsoid which results in Raman scattering. Therefore Raman scattering carries directional information about the ellipsoid [46].

Porto [48] for the first time conducted the study of the polarization direction dependence of the Raman scattering, introduced the depolarization ratio, and related it to the Raman tensor. In 1971, Snyder [49] shed light on the relation between the Raman tensor, molecular orientation and the observed intensity. Dependence of the single molecule SERS signal on polarization was first discussed by Nie and Emory [50] and developed by others [51–53].

The values $\bar{\alpha'}$ and $\bar{\gamma'}$ (shown in Equations 1.12 and 1.13 respectively) are defined as the isotropic and anisotropic part of the Raman tensor.

$$\bar{\alpha'} = \frac{1}{3}(\alpha'_{x,x} + \alpha'_{y,y} + \alpha'_{z,z}) \tag{1.12}$$

$$\bar{\gamma'}^2 = \frac{1}{2}\{(\alpha'_{x,x} - \alpha'_{y,y})^2 + (\alpha'_{y,y} - \alpha'_{z,z})^2 + (\alpha'_{z,z} - \alpha'_{x,x})^2 + 6[(\alpha'_{y,x})^2 + (\alpha'_{y,z})^2 + (\alpha'_{z,x})^2]\} \tag{1.13}$$

$\bar{\alpha'}$ is the magnitude of differential polarizability of the molecule and $\bar{\gamma'}$ is the degree of departure from its isotropic behavior [54]. These will be explicitly used to give the Raman activities of scattered light in directions parallel and perpendicular to the incident laser polarization direction or the sum of scattered light in both directions and for calculation of the depolarization ratio of an individual vibration mode.

1.6 SERS advantages and drawbacks

SERS has received great interest for the last three decades due to its potential for ultrahigh sensitivity and specificity. This is particularly true when compared to fluorescence, which is the current *in situ* monitoring method used for produced water [23]. See Figure 1.2 for schematic diagrams of Raman scattering and fluorescence. Fluorescence spectra contain broad bands compared to Raman: a Raman peak width of a dye will be 15 cm^{-1}, but the width for a fluorescence emission will be in the range of 1000–2000 cm^{-1} [55]. Fluorescence spectra also lack detailed molecular structural data [37, 55]. Raman scattering reveals information about molecular vibrational levels. Since molecular vibrations are dependent on the types of atoms contributing to molecular bonds and their bond strengths, which are specific to unique atomic arrangements for a particular compound, Raman spectra provide fingerprint-level information. These specific bands can distinguish similar molecules like phenanthrene, anthracene, pyrene, benzo-[a]pyrene and perylene in a Raman spectrum of a multicomponent solution containing these PAHs [24]. This aspect of Raman along with the ultrahigh sensitivity of SERS leads to detection of trace concentration of analytes as low as the single molecule level [50, 56].

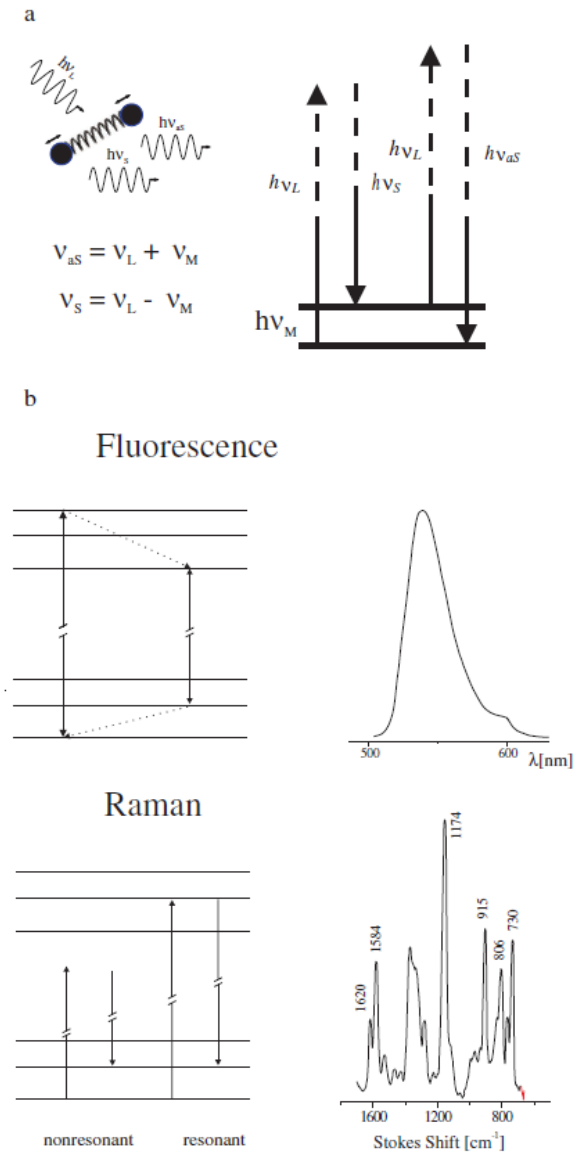

Figure 1.2: Schematic diagrams of Raman scattering and fluorescence. (a) Typical vibration/Q-displacement and its interaction with the incident laser resulting in inelastic scattering at frequencies above or below the laser frequencies. (b-Fluorescence) A wide fluorescence band as a consequence of an electronic transition. (b-Raman) Normal Raman *vs.* resonance Raman where the molecule is excited to virtual or real excited states respectively, and a Raman spectrum (used with permission from [37]).

SERS differs from normal Raman spectroscopy due to the various resonant contributions, as discussed before. First, these contributions make SERS spectra more dependent on the laser wavelength than normal Raman spectra. The match between the laser wavelength λ_{ex} and the plasmon band wavelength (λ_{max} in the extinction spectrum) of the SERS substrate does not necessarily correlate with the SERS intensity [57]. For example spherical gold nanoparticles with $\lambda_{max} = 530$ nm show good enhancement activity with a lower energy excitation at $\lambda_{ex} = 632$ nm [58]. Second, totally symmetric and non-totally symmetric vibrational modes have different relative contributions to signal enhancement. The orientation of the molecule with respect to the surface, and consequently the contribution of metal Fermi levels to the accessible states of the molecule-metal system, significantly impacts the extent of difference (intensity/energy shift of specific Raman bands) between SERS and the corresponding Raman spectrum [38].

Aspects of the Raman spectra of organic molecules like tetracene depend on the energy of the laser due to emergence of fluorescence under higher energy Raman lasers [59]. Fluorescence has a higher signal to noise ratio compared to Raman and hence it swamps weak Raman signals [37]. As seen for tetracene (see Table 1.2), the number of detected Raman bands in the Raman spectra is at a maximum for the lowest energy laser (1064 nm) and decreases with increase in photon energy until all are superimposed by a strong fluorescent signal under the highest energy laser (514 nm). In contrast, this is less prominent in phenanthrene which does not naturally fluoresce although a small residual spectral background can be seen at the higher energy side with particular fluorescence superimposing a number of CH stretching modes under the 514 nm laser (see Figure C.6 in Appendix C and Table 1.3). Background fluorescence might be quenched by SERS-active metallic substrates [37], which is an advantage.

Resonance of a molecule's electronic transition energy with the electric field experienced by the molecule in the vicinity of the surface of the SERS substrate adds more complexity to SERS experiments [38]. Furthermore, specific Raman peaks' intensities will show some variances for different laser energies regardless of resonance effects and will be discussed in section 4.3.2 for Raman activities (not to be confused with Raman intensities). This is reported in the literature for some of the Raman bands in Table 1.3: for example an increase of signal intensity is seen for the 547 cm^{-1} Raman band of phenanthrene from medium to strong when the laser energy is altered from 1064 nm to 514 nm. Another increase in signal is from strong to very strong for the 710 cm^{-1} band [59].

With the many factors contributing to the SERS response, the SERS signal might not be reproducible, which precludes the reliable concentration measurement of an analyte [60]. This irreproducibility is due to differences in signal intensity or appearance/disappearance of specific mode(s) during different data acquisition runs, or a combination of both. One key to this issue is the development of a stable and reproducible SERS-active substrate, which is able to generate a high signal enhancement [51]. Such a substrate is not the sole requirement for obtaining a reproducible and reliable SERS signal. However, to address reproducibility issues of both band intensity and shape, one needs to create conditions that allow control over all of the steps that lead to the SERS phenomenon, for example to think of ways to always obtain the same orientation of the analyte on the substrate.

Surface chemistry of the substrate defines the adsorption geometry (orientation) through local coordination. This local surface geometry can vary over a substrate through inherent heterogeneity, defects, etc. [61]. Furthermore, interactions between adsorbates can also impact adsorption geometry, and this depends on surface coverage, which, could complicate the orientation [61]. One case that could lead to this situa-

Table 1.2: Raman spectral wavenumbers and vibrational assignments for tetracene under different laser energies. The values accompanied with the abbreviations are Raman energy shifts in cm^{-1}. Column titles in bold represent the laser wavelength of the Raman instrument. s, strong; m, medium; w, weak; sh, shoulder; w sh, weak shoulder (used with permission from [59]).

1064 nm	**785 nm**	**633 nm**	**514 nm**	**Assignments**
3050 m			No peaks	C-H stretching
1630 w sh				
1616 m	1614 m	1619 m		C=C stretching
1606 w sh	1605 w sh			
1542 st	1540 st	1542 m		C-C or ring stretchings
1517 w	1517 w			
1490 w				
1447 st	1445 st	1447 w		C-C stretching vibrations
1403 m	1400 m			Skeletal ring vibration
1384 st	1381 st	1383 m		C=C in plane vibration
1368 w	1364 w			
1197 m	1194 m			C-H in plane
1180 m	1117 m			C-H in plane deformation vibration
1160 m	1157 m			C-H in plane deformation vibration
997 m	994 m			C-H in plane deformation vibration
973 w				
960 w				
851 w				C-H out of plane deformation vibration
751 m	748 m			CCC ring deformations
494 m	491 m			C-C deformation vibration
314 st	3311 m			CCC ring deformations
213 w				

Table 1.3: Raman spectral wavenumbers and vibrational assignments for phenanthrene under different laser energies. The values accompanied with the abbreviations are Raman energy shifts in cm^{-1}. Column titles in bold represent the laser wavelength of the Raman instrument. v st, very strong; st, strong; m, medium; w, weak; v w, very weak; sh, shoulder; wsh, weak shoulder; m sh, medium shoulder; st sh, strong shoulder (used with permission from [59]).

1064 nm	**785 nm**	**633 nm**	**514 nm**	**Assignments**
3071 st	3071 st	3072 st	3071 st	CH stretching
3055 m	3055 m	3056 m	3057 m sh	
3035 m	3035 m	3034 m		
	1748 w			
1622 m	1620 m	1622 v st	1622 st	C=C stretching vibration
1613 m sh	1613 m sh	1613 st sh	1613 st sh	C-C stretching
1599 w sh	1599 w sh	1599 w	1599 w	
1569 m	1569 w	1569 m	1570 m	C-C stretching
1523 st	1523 m	1523 st	1523 st	
1440 st	1437 st	1439 v st	1440 v st	C-C stretching, HCC bending
1429 w sh	1429 w sh	1429 st	1429 st	C-C stretching, HCC bending
1418 m sh	1418 m sh	1418 st	1418 st	
		1402 w sh	1402 w sh	
		1362 m sh	1362 m sh	
1349 st	1349 st	1349 v st	1350 v st	C-C stretching, HCC bending
1318 w	1318 w	1320 w	1316 w	
1245 st	1242 st	1244 m	1245 m	HCC bending
1200 m	1200 m	1200 m	1200 m	C-C stretching, HCC bending
1170 m	1170 m	1169 m	1169 m	
1141 w	1141 w	1141 w	1162 m	
1036 st	1033 st	1035 st	1036 st	C-C stretching, HCC bending
828 m	825 m	828 st	828 m	
710 st	706 st	709 vst	710 v st	
547 m	543 m	546 st	546 st	CCC bending
498 v w	498 v w	496 w	498 w	
442 w	442 w	441 w	442 w	
410 st	406 st	409 st	409 st	CCC bending
249 m	246 m	242 m	250 m	

tion is when SERS substrates, after being submerged in the analyte solution, are dried before SERS acquisition. The rapid solvent vaporization leads to accumulation of analyte molecules at particular regions on the SERS-active substrate. A solution to this coverage complexity could be the implementation of a molecularly imprinted polymer (MIP) layer on the SERS-active surface (see sections 5.2.4 and 5.2.5 in Chapter 5). Another ideal to avoid signal irreproducibility would be to maintain the same relative contributions from electromagnetic and chemical enhancement between the analyte and the SERS-active substrate by preventing the chemically adsorbed molecule from rotating through its bond to the surface. For example, thiophenol adsorbed via its sulfur atom within a hot spot can rotate along its C_2 symmetry axis. This rotation results in a varying interaction angle with the anisotropic electric field present at hot spots and this will alter the contribution of electromagnetic and chemical enhancement mechanisms [62].

One last thing that should be considered is the Raman laser polarization direction. Application of polarization/orientation is a valuable option [50, 52, 53, 63–65]. This provides the advantage of richer data to distinguish between otherwise similar spectra of similar molecules. One application is in characterization of crystal structures as a complementary technique to X-ray crystallography [63]. Another application is the determination of alignment of single wall carbon nanotubes [64]. Polarization/orientation in SERS (polarized SERS) has been considered with single molecule detection [50,52,53,65]. These have all been relying on the fact that SERS intensities vary with the polarization direction of the incident laser. For lasers in the visible and NIR regions the enhancement for SERS is confirmed to be maximum when the polarization of the incident laser is parallel to the local field, e.g., parallel to the axis of a dimer of two Ag nano spheres with a nanometric gap (hot spot) in between [52,53,65].

As seen in Chapter 4, characteristic peaks in otherwise similar molecules can

vary with changing laser polarization direction. Therefore, the option of changing polarization can be an important element in designing a sensor, provided that the changes with polarization are well understood. For this reason, in Chapter 4 this has been studied on phenanthrene and naphthalene molecules confined in space. In the case of a real SERS experiment, since the analyte molecule is adsorbed on the SERS substrate (confined), a change in laser polarization direction will affect the angle at which the laser field will interact with the molecular plane of the confined molecule.

1.7 Ideal SERS substrate and substrate classifications

Lin [58] laid out four characteristic parameters of an ideal SERS substrate:

1. High SERS activity to yield high sensitivity. The substrate LSPR frequency can be matched to the incident laser frequency by gaining control over the size of the nanoparticles (larger than 50 nm) and their spacing (shorter than 10 nm).

2. Uniformity. For a uniform substrate (one which provides enhancement with a deviation of less than 20% over the whole surface) nanoparticles should acquire a relatively ordered arrangement on the substrate.

3. Good stability and reproducibility. Substrates should maintain their enhancement for a long period. Substrates which are fabricated with the same method should not show enhancement deviations larger than 20% .

4. Cleanliness. Substrates should be free from surface contaminants in order to be able to adsorb weak adsorbates, including unknown samples, and not only strong adsorbates.

A substrate with these four characteristics is not accessible and the optimum design depends on the particular application and the purpose. Lin [58] suggests that for quantitative analysis, uniformity and reproducibility are two parameters required for optimum substrate design, whilst for trace analysis a substrate with a large enhancement is needed.

Alvarez-Puebla classifies SERS-active substrates into two groups [66], depicted schematically in Figure 1.3. First are the colloidal metal nanoparticles in a range of different shapes and sizes [66]. These substrates are produced cost-effectively by synthesizing nanoparticles from chemical reduction, laser ablation, photoreduction, and other wet-chemistry methods [41]. The most common method to make metal suspensions is chemical reduction [41]; in this method the starting material is a metal salt which is reduced by another chemical agent in order to obtain colloidal suspensions of nanoparticles [41].

The second class of SERS-active substrates, according to Alvarez-Puebla, is nanostructured thin films, and they are produced by controlled nanoparticle assembly or by physical vapour deposition, sputtering, electrochemical roughening or electron beam lithography (EBL) [66]. Among these methods, EBL produces uniform substrates with a high enhancement factor and reproducibility, but the disadvantage is its high cost, especially if a substrate with a large area is required [67].

1.8 Sensing package and the application field

The aforementioned microfluidic-based sensor package (see section 1.1) will be used for detection of oil in off-shore drilling sites or screening for chemicals from human activity in the Humber River (Newfoundland and Labrador). The ultimate package (beyond the goal of this thesis) would be roughly the size of a microscope slide and

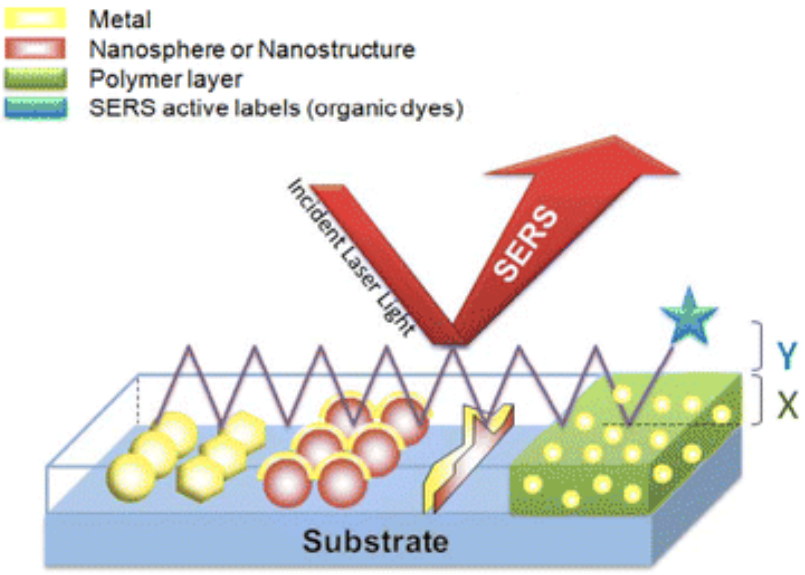

Figure 1.3: Schematic of SERS substrates: different shaped metal nanoparticle colloids or films, metal coated nanospheres, random nanostructures coated with a metallic thin film, or metal nanoparticles mixed within a polymeric coating (used with permission from [68]).

would be easy to use. It could simply be inserted into the target water to be analyzed by the end user and then it would be studied by a portable Raman device to obtain the SERS spectrum. The sensor package could be installed off shore at drilling sites for online screening of oil (such as PAHs) in produced water. The sensor package could even be installed on an autonomous underwater vehicle for exploration in a range of environments.

1.8.1 Motivation for substrate design: compatibility with application and mechanical properties of sensor package

To serve this purpose, fabrication of a metallic thin film on a flat platform (glass slide, silicon wafer) that can also hold microfluidic channels on itself would be desirable. In addition, the use of a flat substrate enables more control over signal efficiency because

the quality of the Raman signal could be further improved by inclusion of MIP thin films (as discussed in 5.2.4), so that a reproducible Raman or SERS signal would be achievable.

This flat SERS-active substrate must also carry specific properties that add to the durability of the sensor package under the harsh variations of environmental conditions such as temperature shock, which result in contraction of components of the sensor package with different coefficients of expansion when being introduced from room temperature to 0 °C ocean water or vice versa. See Figure 1.1 for the schematic of a microfluidic SERS sensor device where interfaces made from various types of materials (polymeric, metallic and glass) exist in a sensor package. For this purpose we need to lay out a stable gold film (SERS active substrate) that can withstand the expansion and contraction cycles of sensor components under temperature fluctuations.

A gold film is a good choice because of its resilience to chemical shock, and it has been used widely in chemical sensors including as a SERS-active metal [69]. For example, Baia *et al.* fabricated gold thin films with 15, 30 and 60 nm thicknesses using thermal evaporation on silica substrates [70]. They coated silica substrates with a monodisperse layer of polystyrene nanospheres (400 nm diameter) by putting a drop of suspension onto the surface to create self-assembled hexagonally close-packed two-dimensional (2D) colloidal crystals in order to generate a mask in advance of metal deposition. This way truncated gold tetrahedra were generated in the spaces between spheres (400 nm diameter) after metal deposition and removal of nanospheres. Farcau and Astilean simply deposited 100 nm thick gold films with thermal evaporation over two-dimensional arrays of 450 nm polystyrene nanosphere coated glass slides without removing the polystyrene layer [71].

1.8.1.1 Enhancing gold film adhesion/mechanical properties

Unfortunately, gold films carry very weak mechanical properties which make them vulnerable to mechanical stresses. For example, gold has such poor adhesion to common substrates like glass and silicon wafers that it delaminates [72–74]. As a traditional way to address this issue, adhesive layers like chromium have been commonly used as an intermediate layer to promote gold adhesion to glass or silicon wafers [72–75].

SU-8 commercial photoresist polymer was used in the work presented in Chapter 2 as the alternative adhesion enhancer layer instead of chromium and a novel processing recipe was implemented to engage gold atoms even more strongly with this polymeric layer by creating a gold-polymer composite interface so that gold film adhesion was enhanced. Atomic force microscopy (AFM) was explicitly used to characterize topography and mechanical properties of these gold films. See Figure B.2 in Appendix B for the schematic of the gold flat substrate fabricated on SU-8. More details regarding the photoresist can be found in the same Appendix.

1.8.2 Tailoring substrate surface features for better SERS signal with annealing approach

Nanostructured metal films are key for SERS. The extent to which a substrate enhances the SERS signal depends on the size and distribution of the nanostructures, and local fields called "hot spots", which can be created by thermal evaporation of metal on surfaces roughened prior to evaporation [71].

A new approach was developed in this work for nanostructured SERS films using a simple two-step metal evaporation and subsequent annealing process. As described in Chapter 3, the SERS Au/Cr films were fabricated with different surface optical properties under different annealing temperatures/lengths leading to various distributions

of gold islands (see Appendix C).

1.9 Atomic Force Microscopy

Atomic force microscopy (AFM) generates information by scanning a probe with a sharp tip over the sample surface (raster scanning). From the deflection of this probe as a result of its interaction with surface features, AFM produces a map of the height (topography) of the surface as it goes along the scan lines to give a rectangular pattern (AFM image) of the scanned region. See Figure 1.4 for an illustration of an AFM cantilever/probe/chip.

In this work either of two scanning modes was used: contact mode or tapping mode. In both modes the tip is always forced to maintain a specific distance from the surface through a feedback loop. In contact mode, the feedback loop relies on maintaining the deflection of the cantilever as the tip scans the surface [76]. In tapping mode, the cantilever is oscillated close to its fundamental resonance frequency in the vicinity of the surface and the tip-sample distance is maintained by keeping the amplitude at a set point [77].

The part of the AFM responsible for translation of the interactions of the tip with the surface is called the force transducer. The force transducer can have different designs; the most common design is the optical lever [78] which was first invented by Meyer and Amer [79], and the first atomic resolution image was obtained by Alexander *et al.* from native oxide on silicon [80]. See Figure 1.5 for a schematic diagram of the optical lever sensor. As shown, as a result of cantilever deflection the reflected laser spot on the detector moves significantly. The back sides of cantilevers are coated with shiny metals like gold in order to improve laser reflection [81]. The deflection signal is the difference between the voltages generated in the top and bottom halves of the

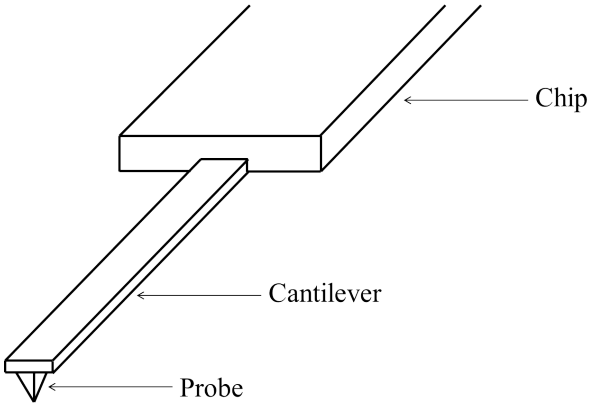

Figure 1.4: AFM cantilever/probe/substrate manufactured by micromachining of Si or Si_3N_4. The words "probe" and "tip" are used interchangeably to convey the same concept. (Not drawn to scale.)

position sensitive detector [81].

The optical (inspection) microscope component of the AFM (here) is a top down design. This optic is used to locate the desired region for scanning and to position the laser light on the cantilever. This microscope optic is also useful to screen the effect of scanning on the thin film. This is particularly useful when carrying out a progressive load scratch (PLS) test (see section 2.2), providing a live video camera view of how the thin film behaves under PLS. See Figure 1.6 for the top view of the tip on the sample after a PLS test.

1.9.1 Force curves

A force-distance curve (or force curve) is used to describe the response of the surface to the applied force from the probe. To obtain a force curve the probe is driven toward the sample surface to a pre-defined position (this approach part is called extension) and then retracted (this part of force curve is called retraction section). The amount that the cantilever deflects over the extension and retraction steps is used to produce a force-distance curve (see Figure 1.7 for a schematic force curve).

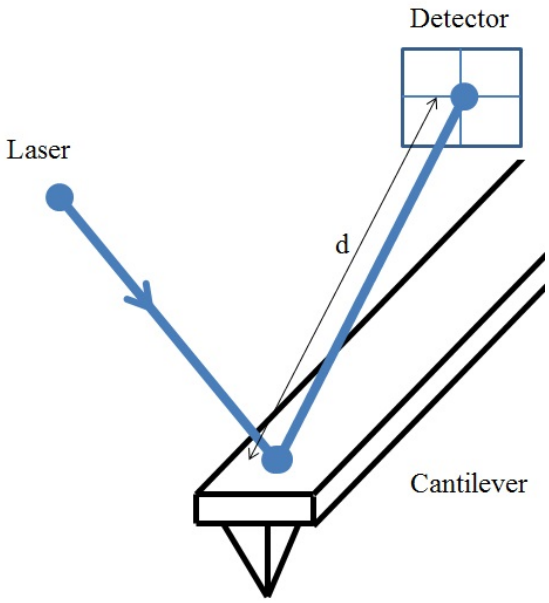

Figure 1.5: Schematic of the optical lever sensor. As a result of cantilever deflection, the reflected laser spot on the detector moves. Since the distance between the cantilever and the detector d is large, a tiny deflection of the cantilever results in a large position displacement of the laser spot at the detector. (Not drawn to scale.)

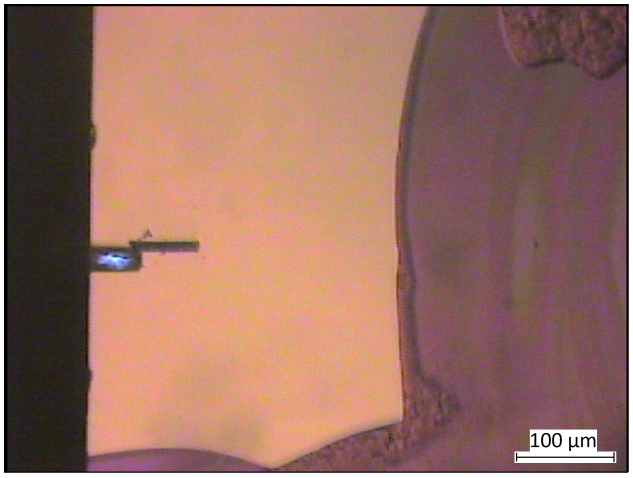

Figure 1.6: The top camera view from a progressive load scanning measurement with a silicon cantilever/probe. The black body at the left is the chip with the cantilever. The probe is at the right most part of the cantilever and it is not visible because it is below the cantilever. The blue light on the cantilever is the laser bouncing back to the detector. The orangish surface under the probe is the gold thin film. The black line in the vicinity of the cantilever is the resulting scratch due to a high applied load of the probe on the thin film during scanning.

There are two alternatives available to set the end point for the force curve. It can be set either as a certain amount of cantilever deflection or a distance from the start point. The former permits the user to determine the maximum force that the probe is allowed to apply to the sample surface which is defined by Hooke's law, $F = -kx$, in which k is the cantilever spring constant representing its stiffness, and F is the force required to deflect the cantilever (acting as a "spring") [82]. If the applied force is large enough to indent the sample, the force analysis is called an indentation study and the corresponding force curve will be called a force indentation curve. If we are interested in the data measured when the tip makes contact with the surface and presses against the sample surface, this is called nanoindentation [83], which has been extensively used to gain insight into relative stiffness in different parts of a sample, e.g., relative distribution of hard magnetic and non-magnetic ceramic particles on the surface of a magnetic storage tape [84].

The AFM software allows the user to acquire force curves in a grid pattern over an area of interest to measure the tip-sample interaction across the sample surface. This is called a force map; Eaton and West call this utility by different names such as layered imaging, volume spectroscopy or force volume imaging [78]. The data from force maps can be averaged to reflect the sample's mechanical properties like elastic modulus and stiffness.

Stiffness (S) is defined as the resistance of the sample against indention. It is the slope of the extension (the slope of the upward part of the red segment in Figure 1.7) or retraction segment (the downward part of the blue segment in Figure 1.7) of the force curve which is obtained from Equation 1.14 in which F stands for the load force and Ind stands for the indentation depth [85, 86].

$$S = \frac{F}{Ind} \tag{1.14}$$

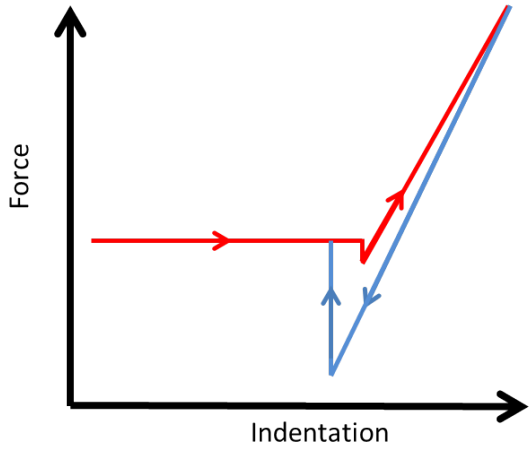

Figure 1.7: A schematic force curve. The red segment is the extension part (load part) of the force curve in which the tip approaches the surface and then snaps to the surface due to attractive forces overcoming the cantilever stiffness; after this point the indentation starts where the loaded force increases up to the set point and then the tip retracts where the blue segment (unloading part) starts and ends where the load section started.

The elastic modulus can be obtained by modeling the indentation (force-indentation curve) via the Hertz model. This model assumes an elastic interaction between the tip of a known shape and the sample [86–88]. The force-indentation relation for a hyperboloidal contact which was used in this work for elastic modulus calculation is based on the Hertzian model which is given by Equation 1.15 [89]:

$$F = \frac{Ea^3}{(1-\sigma^2)R}\left[\xi^2 + (1-\xi^2)\frac{R\delta}{a^2}\right], \tag{1.15}$$

where F is the load force, ξ is $R\cot(\alpha)/a$, a is the contact area radius, α is the tip conical angle (30° according to manufacturer's specifications for indenters), R is the probe's radius of curvature, E is the Young's modulus, σ is the sample's Poisson ratio (0.42 for gold [90]), and δ is the indentation depth and is equal to

$$\delta = \frac{a^2\xi}{2R}\left[\frac{\pi}{2} + \arctan\left(\frac{1}{2\xi} - \frac{\xi}{2}\right)\right]. \tag{1.16}$$

1.9.2 Calibration of cantilever force constant

To measure mechanical properties (elastic modulus and stiffness) and accurate depths for indentation experiments on delicate thin films, one should not rely on the averaged properties provided on the manufacturer's label for AFM tips package. Specifications (force constant, resonance frequency) differ from one cantilever to another in a package of 50 cantilevers. See Table A.1 for cantilever specifications on a factory provided label for a package of 50 cantilevers, which shows a wide distribution for resonance frequency and force constant. Hence the actual force constant of the cantilever must be verified before nanoindentation measurements [82] rather than using the nominal value provided by the manufacturer.

Among the common methods (also used here) for calculating force constant (cantilever calibration) is the thermal noise method, which was first introduced by Hutter and Bechhoefer [91, 92]. A simplified explanation of this is to assume the cantilever as a simple harmonic oscillator $\frac{1}{2}kx^2$ in which case, according to the equipartition theorem, $\frac{1}{2}kx^2$ is equal to $\frac{1}{2}k_BT$. Hence, from a thermal noise measurement, which determines the value for x^2, the force constant k can be calculated according to the equipartition theorem. This consists of measuring the thermal noise spectrum when the cantilever is in contact with a hard and smooth surface like mica. Although there is a possibility of tip shape change under oscillation, the technique has been shown to be precise and accurate [93].

1.9.3 Roughness measurements

Surface roughness is a crucial surface characteristic of materials which can impact optical and electronic properties [94]. AFM is the first choice to measure nanoscale roughness and it is widely used to determine roughness for metals and metal oxides

[95]. AFM gives height data, which provides high contrast roughness measurements. Scanning electron microscopy (SEM) cannot access this contrast for surfaces with roughness values less than 10 nm. This is because SEM detects electrons scattered within the range of a few nanometers under the surface, but roughness measurement with optical techniques requires opaque surfaces. However, none of these limitations apply to AFM because it directly measures accurate roughness values with Angstrom level [78].

For accurate roughness comparisons with AFM, the general rule is to maintain identical scanning, processing and analysis for imaging conditions. Imaging parameters such as tip radius, pixel size, scan speed and size should be defined for reproducible roughness measurements according to Walther *et al.* [96]. Roughness can be measured as root mean square of pixel heights (rms).

$$\text{Roughness} = \sqrt{\frac{1}{N}\sum_i Y_i^2} \tag{1.17}$$

N is the number of points and Y_i is the vertical distance of the ith point from a mean line. Walther *et al.* also demonstrate that the rms method is a reliable roughness measurement method to compare surface roughnesses, as long as appropriate scan speed and feedback parameters are set so that the AFM tip can manage to entirely access the surface topography [96]. For rms roughness results to be meaningful and useful, scan size and image treatment (if any) must be reported with the roughness values [96, 97].

1.9.4 Thickness measurements

AFM provides an easy way to measure the thickness of thin films. This is of particular value for obtaining data from optical components because a mechanical profiler would

potentially scratch their surfaces [78]. A thickness measurement could be performed by scanning in contact mode across a masked region. See Appendix A.

1.10 Overview of the thesis

Several components are required to develop a SERS sensor. One important factor in sensor package development is the mechanical robustness of the overall sensor package when all the various types of material interfaces meet to make the ultimate sensor package functional (see Figure 1.1 where metal, plastic and insulator boundaries co-exist). The second chapter of this thesis introduces a new method to fabricate thin gold films on glass slides mediated with SU-8 polymer photoresist with high adhesion and improved mechanical properties for a wide range of delicate applications. These include MEMS-based sensors e.g. fabrication of SU-8 cantilevers for biosensor applications [98, 99] or for atomic force microscopy [100]. The third chapter introduces a new class of mixed metal substrates and explores varying their properties and SERS activity to detect phenanthrene. Chapter 4 describes a time dependent Hartree Fock method which evaluates how the laser polarization and energy can change the Raman signal of confined and free molecules respectively. This specifically is important because it reveals the effect of the laser electric field direction on the Raman response of an oriented molecule. This computational approach can be conducted for particular analytes to plan optimum laser incident-molecule interaction geometry and eventually benefit the sensor design.

Bibliography

[1] Dasary, S. S.; Ray, P. C.; Singh, A. K.; Arbneshi, T.; Yu, H.; Senapati, D. *Analyst* **2013,** *138,* 1195-1203.

[2] Farrell, M. E.; Pellegrino, P. M. *Proc. SPIE Int. Soc. Opt. Eng.* **2012,** *8460,* 84600J/1-84600J/12.

[3] Farrell, M. E.; Holthoff, E. L.; Pellegrino, P. M. *Proc. SPIE Int. Soc. Opt. Eng.* **2012,** *8358,* 835816/1-835816/11.

[4] Tan, E.; Yin, P.; Lang, X.; Zhang, H.; Guo, L. *Spectrochim. Acta, Part A* **2012,** *97,* 1007-1012.

[5] Baker, G. A.; Moore, D. S. *Anal. Bioanal. Chem.* **2005,** *382,* 1751-1770.

[6] Greenwood, R.; Mills, G. A.; Roig, B. *TrAC, Trends Anal. Chem.* **2007,** *26,* 263-267.

[7] Faksness, L.; Grini, P.; Daling, P. *Mar. Pollut. Bull.* **2004,** *48,* 731-742.

[8] Ahmadun, F.; Pendashteh, A.; Abdulah, L.; Biak, D. R. A.; Madaeni, S. S.; Abidin, Z. Z. *J. Hazard. Mater.* **2009,** *170,* 530-551.

[9] Diercks, A.-R.; Highsmith, R. C.; Asper, V. L.; Joung, D.; Zhou, Z.; Guo, L.; Shiller, A. M.; Joye, S. B.; Teske, A. P.; Guinasso, N.; Wade, T. L.; Lohrenz, S. E. *Geophys. Res. Lett.* **2010,** *37,* L20602/1-L20602/6.

[10] Zielinski, O.; Busch, J. A.; Cembella, A. D.; Daly, K. L.; Engelbrektsson, J.; Hannides, A. K.; Schmidt, H. *Ocean Sci.* **2009,** *5,* 329-349.

[11] Vo-Dinh, T. *Trends Analyt. Chem.* **1998,** *17,* 557-582.

[12] Halvorson, R. A.; Vikesland, P. J. *Environ. Sci. Technol.* **2010,** *44,* 7749-7755.

[13] Pfannkuche, J.; Lubecki, L.; Schmidt, H.; Kowalewska, G.; Kronfeldt, H.-D. *Mar. Pollut. Bull.* **2012,** *64,* 614-626.

[14] Cialla, D.; März, A.; Böhme, R.; Theil, F.; Weber, K.; Schmitt, M.; Popp, J. *Anal. Bioanal. Chem.* **2012,** *403,* 27-54.

[15] Meier, S.; Morton, H. C.; Nyhammer, G.; Grosvik, B. E.; Makhotin, V.; Geffen, A.; Boitsov, S.; Kvestad, K. A.; Bohne-Kjersem, A.; Goksoyr, A.; Folkvord, A.; Klungsoyr, J.; Svardal, A. *Mar. Environ. Res.* **2010,** *70,* 383-394.

[16] Neff, J. M.; Johnsen, S.; Frost, T. K.; Utvik, T. I. R.; Durell, G. S. *Mar. Environ. Res.* **2006,** *62,* 224-246.

[17] Ball, A.; Truskewycz, A. *Environ. Sci. Pollut. Res. Int.* **2013,** *20,* 4311-4326.

[18] Verschueren, K. *Handbook of Environmental Data on Organic Chemicals;* volume 1-2 John Wiley & Sons: New York, NY, 4th ed.; 2001.

[19] Flaveny, C.; Perdew, G. *Mol. Cell. Pharm.* **2009,** *1,* 119-123.

[20] Billiard, S. M.; Timme-Laragy, A. R.; Wassenberg, D. M.; Cockman, C.; Di Giulio, R. T. *Toxicol. Sci.* **2006,** *92,* 526-536.

[21] Asher, S. A. *Anal. Chem.* **1984,** *56,* 720-724.

[22] Krupadam, R. J.; Bhagat, B.; Wate, S. R.; Bodhe, G. L.; Sellergren, B.; Anjaneyulu, Y. *Environ. Sci. Technol.* **2009,** *43,* 2871-2877.

[23] Okparanma, R. N.; Mouazen, A. M. *Appl. Spectrosc. Rev.* **2013,** *48,* 458-486.

[24] Du, J.; Jing, C. *J. Phys. Chem. C* **2011,** *115,* 17829-17835.

[25] Xie, Y.; Wang, X.; Han, X.; Song, W.; Ruan, W.; Liu, J.; Zhao, B.; Ozaki, Y. *J. Raman Spectrosc.* **2011,** *42,* 945-950.

[26] Xie, Y.; Wang, X.; Han, X.; Xue, X.; Ji, W.; Qi, Z.; Liu, J.; Zhao, B.; Ozaki, Y. *Analyst* **2010,** *135,* 1389-1394.

[27] Schmidt, H.; Ha, N.; Pfannkuche, J.; Amann, H.; Kronfeldt, H.; Kowalewska, G. *Mar. Pollut. Bull.* **2004,** *49,* 229-234.

[28] López-Tocón, I.; Otero, J.; Arenas, J.; Garcia-Ramos, J.; Sanchez-Cortes, S. *Anal. Chem.* **2011,** *83,* 2518-2525.

[29] Shi, X.; Kwon, Y.-H.; Ma, J.; Zheng, R.; Wang, C.; Kronfeldt, H.-D. *J. Raman Spectrosc.* **2013,** *44,* 41-46.

[30] Leyton, P.; Gomez-Jeria, J. S.; Sanchez-Cortes, S.; Domingo, C.; Campos-Vallette, M. *J. Phys. Chem. B* **2006,** *110,* 6470-6474.

[31] Olson, L. G.; Uibel, R. H.; Harris, J. M. *Appl. Spectrosc.* **2004,** *58,* 1394-1400.

[32] Fleischman, M.; Hendra, P. J.; McQuillan, A. J. *Chem. Phys. Lett.* **1974,** *26,* 163-166.

[33] Jeanmaire, D. L.; Van Duyne, R. P. *J. Electroanal. Chem.* **1977,** *84,* 1-20.

[34] Albrecht, M. G.; Creighton, J. A. *J. Am. Chem. Soc.* **1977,** *99,* 5215-5217.

[35] Moskovits, M. *J. Chem. Phys.* **1978,** *69,* 4159-4161.

[36] Haynes, C. L.; Yonzon, C.; Zhang, X.; Van Duyne, R. *J. Raman Spectrosc.* **2005,** *36,* 471-484.

[37] Kneipp, K.; Kneipp, H.; Itzkan, I.; Dasari, R. R.; Feld, M. S. *J. Phys. Condens. Matter* **2002,** *14,* R597-R624.

[38] Lombardi, J. R.; Birke, R. L. *Acc. Chem. Res.* **2009,** *42,* 734-742.

[39] Xia, Y.; Halas, N. J. *MRS Bull.* **2005,** *30,* 338-344.

[40] Xia, Y.; Xiong, Y.; Lim, B.; Skrabalak, S. E. *Angew. Chem. Int. Ed.* **2009,** *48,* 60-103.

[41] Aroca, R. F.; Alvarez-Puebla, R. A.; Pieczonka, N.; Sanchez-Cortez, S.; Garcia-Ramos, J. V. *Adv. Colloid Interface Sci.* **2005,** *116,* 45-61.

[42] Moskovits, M. *Rev. Mod. Phys.* **1985,** *57,* 783-826.

[43] Otto, A. *Top. Appl. Phys.* **1984,** *54,* 289-418.

[44] Bulkin, Bernard, J. The Raman Effect: An Introduction. In *Analytical Raman Spectrosocopy*, Vol. 114; Grasselli, J. G.; Bulkin, Bernard, J., Eds.; John Wiley & Sons: New York, 1991; Chapter 1, pages 1–18.

[45] Otto, A. *J. Raman Spectrosc.* **1991,** *22,* 743-752.

[46] Tanaka, M.; Young, R. *J. Mater. Sci.* **2006,** *41,* 963-991.

[47] Ovander, L. *Opt. Spectrosc.* **1960,** *9,* 571-575.

[48] Porto, S. *J. Opt. Soc. Am.* **1966,** *56,* 1585-1589.

[49] Snyder, R. *J. Mol. Spectrosc.* **1971,** *37,* 353-365.

[50] Nie, S.; Emory, S. R. *Science* **1997,** *275,* 1102-1107.

[51] Kneipp, K.; Kneipp, H.; Itzkan, I.; Dasari, R. R.; Feld, M. S. *Chem. Rev.* **1999,** *99,* 2957-2976.

[52] Xu, H. X.; Käll, M. *ChemPhysChem* **2003,** *4,* 1001-1005.

[53] Etchegoin, P. G.; Galloway, C.; Le Ru, E. C. *Phys. Chem. Chem. Phys.* **2006,** *8,* 2624-2628.

[54] Laserna, J. J. *Modern Techniques in Raman Spectroscopy;* John Wiley & Sons Inc.: Chichester, 1996.

[55] Etchegoin, P. G.; Le Ru, E. C. *Phys. Chem. Chem. Phys.* **2008,** *10,* 6079-6089.

[56] Kneipp, K.; Wang, Y.; Kneipp, H.; Perelman, L. T.; Itzkan, I.; Dasari, R. R.; Feld, M. S. *Phys. Rev. Lett.* **1997,** *78,* 1667-1670.

[57] Moskovits, M. *Phys. Chem. Chem. Phys.* **2013,** *15,* 5301-5311.

[58] Lin, X.-M.; Cui, Y.; Xu, Y.-H.; Ren, B.; Tian, Z.-Q. *Anal. Bioanal. Chem.* **2009,** *394,* 1729-1745.

[59] Alajtal, A. I.; Edwards, H. G. M.; Elbagerma, M. A.; Scowen, I. J. *Spectrochim. Acta, Part A* **2010,** *76,* 1-5.

[60] Pieczonka, N.; Aroca, R. *ChemPhysChem* **2005,** *6,* 2473-2484.

[61] Ling, X.; Wu, J.; Xu, W.; Zhang, J. *Small* **2012,** *8,* 1365–1372.

[62] Futamata, M.; Maruyama, Y.; Ishikawa, M. *J. Phys. Chem. B* **2003,** *107,* 7607-7617.

[63] Mizoguchi, K.; Nakashima, S.-i. *J. Appl. Phys.* **1989,** *65,* 2583-2590.

[64] Liu, P.; Liu, L.; Zhang, Y. *Phys. Lett. A* **2003,** *313,* 302-306.

[65] Tao, J.; Lu, Y. H.; Chen, J. X.; Lu, D. W.; Chen, C. C.; Wang, P.; Ming, H. *Plasmonics* **2011,** *6,* 785-789.

[66] Alvarez-Puebla, R. A.; Liz-Marzán, L. M. *Energy Environ. Sci.* **2010,** *3,* 1011-1017.

[67] Tripp, R. A.; Dluhy, R. A.; Zhao, Y. *Nano Today* **2008,** *3,* 31-37.

[68] Kim, J.; Junkin, M.; Kim, D.-H.; Kwon, S.; Shin, Y. S.; Wong, P. K.; Gale, B. K. *Microfluid. Nanofluid.* **2009,** *7,* 149-167.

[69] Wilson, D. M.; Hoyt, S.; Janata, J.; Booksh, K.; Obando, L. *IEEE Sens. J.* **2001,** *1,* 256-274.

[70] Baia, L.; Baia, M.; Popp, J.; Astilean, S. *J. Phys. Chem. B* **2006,** *110,* 23982-23986.

[71] Farcau, C.; Astilean, S. *J. Phys. Chem. C* **2010,** *114,* 11717-11722.

[72] Rairden, J. R.; Girard, R. T. *Am. Ceram. Soc. Bull.* **1971,** *50,* 536-540.

[73] Thomas, R. E.; HAAS, G. A. *J. Appl. Phys.* **1972,** *43,* 4900-4907.

[74] George, M. A.; Glaunsinger, W. S.; Thundat, T.; Lindsay, S. M. *Thin Solid Films* **1990,** *189,* 59-72.

[75] Huang, Y.; Qiu, H.; Wang, F. P.; Pan, L. Q.; Tian, Y.; Wu, P. *Vacuum* **2003,** *71,* 523-528.

[76] Binnig, G.; Quate, C.; Gerber, C. *Phys. Rev. Lett.* **1986,** *56,* 930-933.

[77] Martin, Y.; Williams, C.; Wickramasinghe, H. *J. Appl. Phys.* **1987,** *61,* 4723-4729.

[78] Eaton, P.; West, P. *Atomic Force Microscopy;* Oxford University Press Inc.: New York, 2010.

[79] Meyer, G.; Amer, N. M. *Appl. Phys. Lett.* **1988,** *53,* 1045-1047.

[80] Alexander, S.; Hellemans, L.; Marti, O.; Schneir, J.; Elings, V.; Hansma, P. K.; Longmire, M.; Gurley, J. *J. Appl. Phys.* **1989,** *65,* 164-167.

[81] Lavrik, N. V.; Sepaniak, M. J.; Datskos, P. G. *Rev. Sci. Instrum.* **2004,** *75,* 2229-2253.

[82] Emerson, R. J.; Camesano, T. A. *Ultramicroscopy* **2006,** *106,* 413-422.

[83] Bhushan, B.; Koinkar, V. N. *Appl. Phys. Lett.* **1994,** *64,* 1653-1655.

[84] Bhushan, B. *Wear* **2005,** *259,* 1507-1531.

[85] Oliver, W.; Pharr, G. *J. Mater. Res.* **1992,** *7,* 1564-1583.

[86] Carl, P.; Schillers, H. *Pflügers Arch., EJP* **2008,** *457,* 551-559.

[87] Hay, J. L.; Wolff, P. J. *J. Mater. Res.* **2001,** *16,* 1280-1286.

[88] Gotzinger, M.; Peukert, W. *J. Adhes.* **2004,** *80,* 223-242.

[89] Kumar, R. M.; Merschrod S., E. F.; Poduska, K. M. *Biomacromolecules* **2009,** *10,* 1970-1975.

[90] Kipp, D. O. *Metal Material Data Sheets;* MatWeb - Division of Automation Creation, Inc.: Blacksburg, VA, USA, 2010.

[91] Hutter, J. L.; Bechhoefer, J. *Rev. Sci. Instrum.* **1993,** *64,* 1868-1873.

[92] Hutter, J. L. *Langmuir* **2005,** *21,* 2630-2632.

[93] Matei, G. A.; Thoreson, E. J.; Pratt, J. R.; Newell, D. B.; Burnham, N. A. *Rev. Sci. Instrum.* **2006,** *77,* 083703/1-083703/6.

[94] Swerts, J.; Temst, K.; Van Bael, M. J.; Van Haesendonck, C.; Bruynseraede, Y. *Appl. Phys. Lett.* **2003,** *82,* 1239-1241.

[95] Cai, K. Y.; Muller, M.; Bossert, J.; Rechtenbach, A.; Jandt, K. D. *Appl. Surf. Sci.* **2005,** *250,* 252-267.

[96] Walther, F.; Heckl, W. M.; Stark, R. W. *Appl. Surf. Sci.* **2008,** *254,* 7290-7295.

[97] Macdonald, W.; Campbell, P.; Fisher, J.; Wennerberg, A. *J. Biomed. Mater. Res. Part B* **2004,** *70B,* 262-269.

[98] Nordström, M.; Johansson, A.; Sánchez Nogueron, E.; Calleja, M.; Boisen, A. *Microelectron. Eng.* **2005,** *78-79,* 152-157.

[99] Godin, M.; Tabard-Cossa, V.; Miyahara, Y.; Monga, T.; Williams, P. J.; Beaulieu, L. Y.; Lennox, R. B.; Grutter, P. *Nanotechnology* **2010,** *21,* 075501/1-075501/8.

[100] Schneider, A.; Ibbotson, R. H.; Dunn, R. J.; Huq, E. *Microelectron. Eng.* **2011,** *88,* 2390-2393.

Co-authorship Statement

Behrang Moazzez made a major intellectual and practical contribution to the design of the research proposal, practical aspects of the research and data analysis, and manuscript preparation (including writing the first draft of the manuscript and participating in all revisions) for all the work presented in Chapters 2, 3 and 4. Chapter 2, entitled "Improved Adhesion of Gold Thin Films Evaporated on Polymer Resin: Applications for Sensing Surfaces and MEMS" is published in the Sensors open access journal. In this work Stacey M. O'Brien (summer student) repeated the fabrication of spin cast glass slides with SU-8 polymer. The suggested protocol used in Chapter 3, entitled "Annealing Approach to Hot Spots for SERS Substrates: applications to the detection of polycyclic aromatic hydrocarbons (PAHs)" includes fabrication of thermally evaporated bilayer Au/Cr films followed by their annealing at elevated temperatures for fabrication of mixed metal films which was performed by Behrang Moazzez. Fabricated films were characterized for their morphology, chemical composition and optical properties using AFM, SEM/EDX, X-ray diffraction, and UV-Vis reflection spectroscopy by Behrang Moazzez. The SERS activity using the bilayer and resulting mixed metal for detection of phenanthrene was investigated with Raman spectroscopy by Behrang Moazzez. Liam D. Whelan repeated the Raman experiments with bilayer Au=42 nm/Cr=31 nm sample and its annealed counterparts. Chapter 4, "TDHF study of laser field directionality and energy effects on Raman intensities of oriented

PAHs, with applications to the detection of PAHs with SERS" is a computational approach which applies TDHF method within GAMESS-US for calculation of Raman activities of oriented and free molecules and studies the effect of laser energy on the observed Raman activities of various Raman bands; this work was done by Behrang Moazzez.

Chapter 2

Improved Adhesion of Gold Thin Films Evaporated on Polymer Resin: Applications for Sensing Surfaces and MEMS*

2.1 Introduction

Gold is often used in microfabricated devices due to its high electrical conductivity and optical reflectivity, combined with a low Young's modulus of 79 GPa [1, 2]. It has been used widely in chemical and biochemical sensors as a signal transducer based on each of the above mentioned unique properties or their combinations [3]. For example, a gold thin film serves well as a surface enhanced Raman scattering (SERS) substrate in miniaturized microfluidic lab on chip devices due to its inert

*This chapter is a modified version of "Improved Adhesion of Gold Thin Films Evaporated on Polymer Resin: Applications for Sensing Surfaces and MEMS", Moazzez B, O'Brien SM, Merschrod S EF, *Sensors* **13**, 7021-7032 (2013).

character, required for continuous online monitoring under chemical stresses enforced by the environment [4,5]. There are likewise applications in surface plasmon resonance (SPR) sensors [6].

One of the main issues in the applicability of gold thin films in microfabrication technology is their weak adhesion to inert and commonly used glass and silica substrates even using adhesion promoting processes [7–9]. Oxidative metals such as chromium, used as an intermediate layer, can enhance gold adhesion, but because chromium diffuses to the gold surface and oxidizes, the top gold layer morphology and electrical properties are affected dramatically [7, 10]. Polymeric materials have found applications in related fields as adhesive layers as a result of their ease of processing and high chemical resistance which also lead to lower fabrication costs. Hence Ge *et al.* [11] and Nordström [1] have studied the adhesion of Cu and Au, respectively, to photosensitive epoxies including SU-8.

SU-8 is a photosensitive polymer in common use as a structural material [1, 12], not only as a negative photoresist for subsequent fabrication steps. Nordström *et al.* fabricated cantilevers for biochemical detection systems with SU-8 [1]. They deposited a thin layer of Au on top of the SU-8 surface in order to enhance the coatability of the cantilevers with probe molecules. Sameoto *et al.* have also investigated methods to enhance gold adhesion to SU-8 in order to find the optimum procedure which is required to fabricate reliable electrical connections to SU-8 microelectromechanical systems (MEMS) [13].

Increasing gold adhesion to a glass substrate and/or SU-8 is also of interest for microfluidic based SERS substrates, especially if achieved in a more cost- and time-effective manner in comparison with recently patented methods [14], while preserving the same level of control over morphology and thermo-mechanical properties. More generally, adhesion of thin films is a vital consideration for sensor device performance.

There are a few studies regarding gold deposition with physical vapor deposition methods on SU-8 such as reverse imprinting [15–17], and — to the best of our knowledge — no previous study has taken the approach we present here.

The motivation in this work has been to develop a reliable method to fabricate a robust gold thin film with promising mechanical properties. This chapter presents a new method (post-Au-deposition SU-8 polymerization) to improve adhesion and potentially tune the morphology of thermally-evaporated gold films. This protocol results in thin films with appropriate smoothness (roughness values $\cong$ 1 nm range) for many delicate applications in optics for gold mirrors and gratings where micro roughness causes undesirable light scattering [18], cantilever fabrications for atomic force microscopy [19], biosensors [12, 20–22] and chemical sensors such as SERS-active substrates [4]. The method also offers the opportunity to control the fine (nanometer) scale morphology or roughness of the film, which has added advantages for SERS activity. This chapter also illustrates both pragmatic and fundamental approaches to characterize the adhesion quality of metal films, an essential consideration in sensor fabrication and design.

2.2 Experimental

2.2.1 Substrate Preparation

Glass slides (Cole-Parmer precleaned 25 × 75 × 1 mm Plain) were rinsed with 95.5% ethanol, 30% acetic acid and nanopure water (Barnstead, 18.2 MΩ·cm), dried with filtered, dry compressed air, and cut into 25 × 25 mm squares with a diamond scribe (SPI Supplies). After depositing 1 mL of SU-8 (Microchem Corp, SU-8 2010) photoresist onto a glass square, a two step spin-coating process (WS 400, Laurell Technologies) spread SU-8 evenly on the surface to give a final thickness of 20 μm. Following accel-

eration of 100 rpm/s to a final spin speed of 500 rpm for 30 s, a second acceleration of 300 rpm/s led to the final spin speed of 1,000 rpm for 60 s.

Additional samples were prepared with final spin speeds of 4,000 rpm and 1,500 rpm, yielding film thicknesses of 10 μm and 15 μm, respectively. These samples were used to vary the surface roughness.

A soft-bake step involved placing the coated glass slide on a hot plate (Corning PC-35) at 65 °C for one minute followed by 2 minutes on a hotplate (VWR 825 digital Aluminum top) at 95 °C, to evaporate the solvent. Exposure to UV light was performed on the stage of a Maskless Patterning System (Intelligent Micropatterning, LLC) for 2 minutes, immediately followed by a post-exposure bake following the same steps of soft bake for polymerization to occur.

The glass substrates of the "pre-deposition cured" type followed the above steps in succession. The other type of substrate, the "post-deposition-cured" type, involved a metal evaporation step after the soft-bake, before UV exposure.

2.2.2 Metal Deposition

Metal deposition was done using a conventional thermal evaporation chamber (built in-house) with a quartz crystal microbalance (QCM) thickness monitor (INFICON XTM/2 deposition monitor). Substrates, prepared as mentioned above, were placed on the sample holder disc and mounted 20 cm above the source at the same level as the QCM element. Gold foil (Johnson Matthey and Mallory gold) was placed in a tungsten boat (Kurt J. Lesker). Evaporation was conducted at pressures below 10^{-3} Pa. Substrates were removed after allowing the system to cool down to ambient temperature to avoid carbon contamination usually caused by introduction of air to a hot chamber. A 10 nm layer of gold was evaporated on the polymer coated glass slides as reported by the QCM thickness measurement unit. Film thickness was measured

independently by atomic force microscopy (Asylum Research MFP-3D system with MikroMasch CSC37/Cr-Au tip) to be 12 nm.

2.2.3 Mechanical Properties Measurements

Initial screening of adhesion quality involved two simple tests: manual scratching with a tweezer (SPI Swiss Wafer Tweezers 4WF), and attachment/removal of adhesive tape (3M Scotch Magic Tape 810, 3/4 in wide). Then a progressive load scratch test (PLST) was performed with an MFP-3D (Asylum Research) atomic force microscope in contact mode using a silicon tip (NSC35/AlBS, nominal spring constant 6.5–27.5 N/m, MikroMasch). In order to grade the adhesion quality in a quantified manner, increasing forces were applied while the AFM tip was scanning the sample in contact mode until the tip deflection signal showed a discontinuity, also seen in the height and lateral force signals and as a scratch under the optical view. To apply a variable force, the deflection set point was increased as the tip scanned a 90 μm $\times$ 90 μm area. The cantilever deflection set point value is measured as a voltage difference from a split photodiode that detects a laser beam reflected off the back of the cantilever. The force required to scratch is directly proportional to the deflection of the cantilever (measured as a voltage between 0 and 10 V) at the initiation point of the scratch.

To further assess the mechanical response of the gold thin films on the microscale, a combination of destructive nanoindentation and contact mode imaging was performed using the same type of probes as above (NSC35/AlBS, MikroMasch). Pre-indentation contact mode images of a 40 μm $\times$ 40 μm area with scan rate of 1 Hz were followed by destructive indentation (to depths of at least 100 nm, thus past the gold layer and into the SU-8 underlayer) at different locations within that area. Post-indentation contact mode images were obtained of the indented regions. In addition to morphological information, this further identified samples with poor adhesion and hence vulnerable

to disruption by the cantilever during scanning.

Embedded functions within the MFP3D software (Asylum Research) were used to measure stiffness and elastic modulus at regular intervals across a sample. Force maps (50 points over a 20 μm $\times$ 20 μm area for the post-deposition-cured sample and 48 points over a 20 μm $\times$ 20 μm area for the pre-deposition cured sample; indentation rate of 1.39 μm/s) were acquired to extract elasticity data. The force set point was selected for tip indentation depths of around 2 nm (one fifth of the thickness of gold film), to acquire data that reflect the properties of top gold film without also directly probing the underlying solid support (glass slide), and to avoid the plastic deformation described above. Sample force curves are provided in Appendix A.

Before indenting the sample, the instrument was calibrated for its deflection sensitivity by obtaining force curves on a bare mica substrate (See Appendix A). For proper selection of cantilever stiffness with regard to sample stiffness, different levers with different spring constants were tried to choose the lever that produces appropriate force curves. The lever of choice has a spring constant of 20 N/m, as measured using the thermal noise method [23]. All force data used here were obtained with the same tip.

Elastic moduli were calculated based on the Hertzian model [24] by extracting force and indentation depths from the retraction segment of each of the fitted force curves [25], assuming a gold Poisson's ratio of 0.42 [26]. Stiffness was calculated as the slope of the retraction curve, the applied force required to achieve a given indentation.

2.2.4 Topography Measurements

AFM topography images from which we obtained our roughness data were acquired under contact mode (CSC37/AuCr tip, MikroMasch) with a scanning area of 10 μm $\times$ 10 μm and scan rate of 1 Hz. Roughness was calculated as the root mean square

(rms) height value for each image:

$$\text{Roughness} = \sqrt{\frac{1}{N}\sum_i Y_i^2} \tag{2.1}$$

N is the number of points (pixels in the image) and Y is the height at each pixel.

2.3 Results

2.3.1 Scratch Tests

Tweezer scratching and tape attachment/removal tests indicate that the post-deposition-cured sample is more robust than the pre-deposition cured one. The following PLST results verify and quantify this difference in film adhesion quality.

Figure 2.1 is a line profile, perpendicular to the fast scanning direction, from the deflection retrace data channel. This plot clearly illustrates the initiation point of the scratch, when the deflection signal drops after reaching a maximum. The deflection increases as the set point value is increased until the point when the tip penetrates the gold film and the scratch begins, where the deflection drops immediately from its maximum and stays at the same dropped value as the tip pulls away the gold layer.

The higher the voltage for the set point value just before scratch starts, the higher would be the deflection of the cantilever, and both are proportional to a larger force being applied by the cantilever tip against the film surface to initiate the scratch. The set point voltage at the initiation of the scratch for the post-deposition-cured sample was at least 1 μm or 10 V (the maximum measurable deflection) and for the pre-deposition cured sample falls in the range of 320–420 nm or 3.2–4.2 V. This indicates that at least 2.4 times higher force is required to initiate a scratch on the post-deposition-cured sample. It is worth mentioning that for a gold thin film deposited

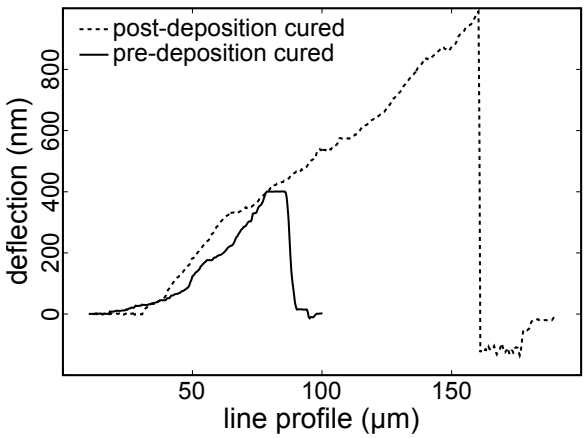

Figure 2.1: Line profile (perpendicular to the fast scan direction) across the deflection retrace image that is obtained while the set point voltage is manually increased. The post-deposition-cured sample requires a much higher applied force (and hence tip deflection) before film disruption (scratching) occurs.

on bare glass, scratching starts at a set point of 0.5 V or 50 nm deflection.

2.3.2 Indenting-Imaging Tests

In the contact mode image for a post-deposition-cured sample (Figure 2.2(a)) the tiny black holes with white color shells are indented locations where the white shells are debris due to disruption of the gold film. The image shows clear signs of deformation during indentation, reinforcing the need to extract elastic data from the retraction and not the extension curve. The indentation marks are not clear in the pre-deposition cured sample (Figure 2.2(b)). Pre-deposition cured films demonstrate a delicate structure, being less scratch-resistant compared with post-deposition-cured films. For post-indentation imaging, when the tip reached the indented region of the pre-deposition cured film (Figure 2.2(b)), it started to scratch the gold surface while imaging.

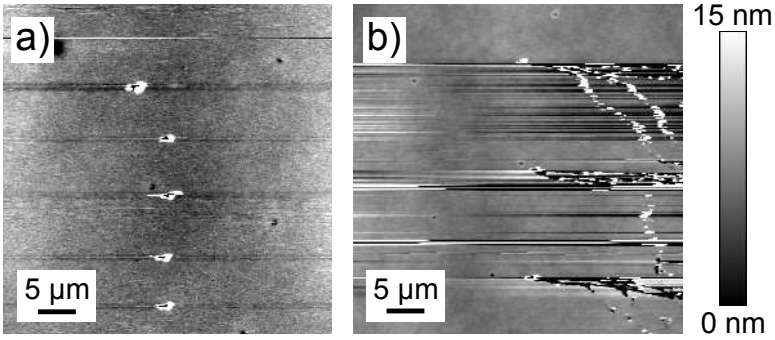

Figure 2.2: Contact mode images after indentation tests for a post-deposition-cured sample (**a**) and a pre-deposition cured sample (**b**). Image (b) shows streaking: gold prepared with pre-deposition curing is so fragile that when the tip reaches the indented area it starts to scratch. In contrast, indentations could be clearly imaged for post-deposition-cured sample (a).

Table 2.1: Average indentation depths, elastic moduli and stiffness for each sample. Statistical information about these averages is provided in the text and in Figure 2.3.

Sample	**Indentation Depth (nm)**	**Elastic Modulus (GPa)**	**Stiffness (nN/nm)**
Pre-deposition-cured	2.8±0.8	98±12	98±32
Post-deposition-cured	2.3±0.4	100±10	113±22

2.3.3 Force Curves

Average indentation depths, elastic moduli, and stiffness are collected in Table 2.1. A shallower indentation value of 2.3 ± 0.4 nm was observed for post-deposition-cured thin film samples compared with 2.8 ± 0.8 nm for the pre-deposition cured samples, with a correspondingly higher stiffness. The difference in average stiffness and indentation depth between these two sets of data is statistically significant with 95% confidence ($P_{stiff} = 2 \times 10^{-4}$; $P_{depth} = 6 \times 10^{-4}$). Here and elsewhere, assessment of statistical significance between populations uses a two-tailed t-test assuming unequal variance in the two data sets.

Figure 2.3(a) shows the distribution of calculated elastic properties for each sample with box plots. The mean elastic modulus is slightly larger for the post-deposition-

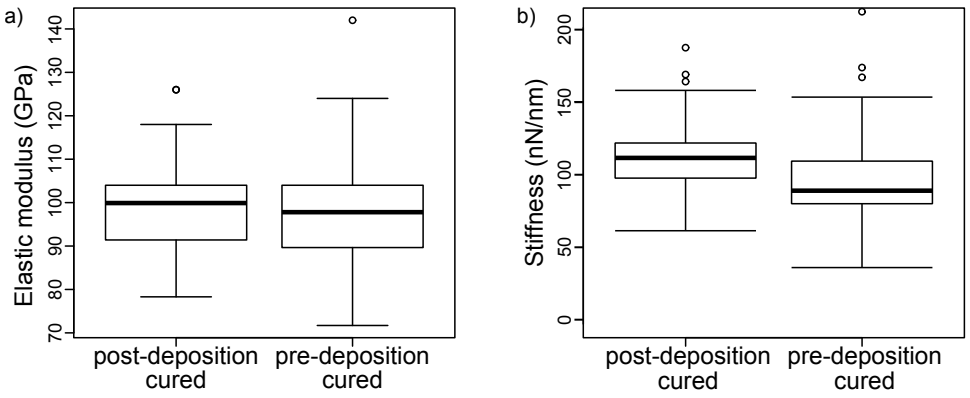

Figure 2.3: Box plots for elastic modulus (**a**) and stiffness (**b**) values calculated for each sample. The average elastic moduli for the two sample types are not significantly different, but the stiffness for the post-deposition-cured sample is significantly higher. The circles are outliers.

cured gold film sample, but a t-test analysis rejects any significant difference, rather providing a significant (19%) probability of similarity. Gold films prepared with the pre-deposition recipe give more centered values but a wider range for elastic modulus, while clearly for post-deposition-cured samples the values are distributed in a slightly narrower range although skewed. The stiffness values shown in Figure 2.3(b) do differ significantly, with the post-deposition-cured sample demonstrating higher stiffness and a narrower distribution of stiffness. The force curves were shallow enough that they showed no signatures of plastic deformation.

Because we are measuring thin films, there is a chance that the substrate contributes significantly to the resultant nanoindentation measurement. Analysis of curves with indentation depths less than 2 nm (to avoid excess contribution from the solid support) yields elastic moduli of 93 $\pm$ 10 GPa for the post-deposition-cured sample and 101 $\pm$ 23 GPa for the pre-deposition cured sample, with distributions with significant overlap with the whole data set. Furthermore, the force curve shapes indicate no evidence of substrate effect since the curvature of the extension and retraction curves was totally due to the probe shape, not coupling with the harder substrate.

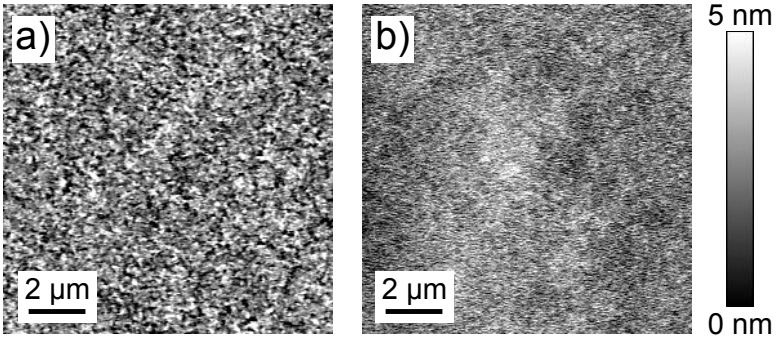

Figure 2.4: AFM images for gold films prepared by the (**a**) post-deposition-cured recipe and (**b**) pre-deposition cured recipe on 20 μm thick SU-8 layers. The morphologies and hence roughness values are different.

The solid support cannot be excluded entirely given the thin and soft nature of the film being measured [27], but this small contribution will be found across all samples and therefore the trends we measure are still interpretable.

2.3.4 AFM Topography Images

Height images for both pre-deposition cured and post-deposition-cured samples (Figure 2.4) show generally smooth films (roughness values on the order of 1 nm). Sample roughness can introduce distortion in the force curve due to torsional momentum resulting in a twist of the tip [28], but our samples with roughness of less than 3 nm on a 1 μm $\times$ 1 μm scale will not show this effect.

A gold film on bare glass has a roughness of 1.42 nm (as defined in Equation (2.1)). The pre-deposition-cured films show a much smoother gold layer, while the post-deposition-cured films are rougher. Table 2.2 presents these data for gold films on a 20 μm-thick SU-8 underlayer, the sample type discussed up to this point. Data from additional samples with varying thickness of SU-8 underlayer (15 μm and 10 μm) show the potential for modifying the gold layer morphology for the post-deposition-cured samples.

Table 2.2: Roughness values for 12 nm thick gold films on pre- and post-deposition-cured samples with different thickness of SU-8 underlayer. For comparison, the roughness measured for gold film without an SU-8 underlayer was 1.42 nm. Roughness data are calculated over 10x10 μm scan area.

	Roughness in nm		
Sample	**20 μm SU-8**	**15 μm SU-8**	**10 μm SU-8**
Pre-deposition-cured	1.02	0.90	0.98
Post-deposition-cured	1.36	2.01	1.52

2.4 Discussion

Thin-film coatings may be non-durable under thermal fluctuations where materials with different thermal expansion coefficients are joined together in a packed sensor. Problems with mechanical stability can be exacerbated when one layer is deposited at elevated temperature as in the case of gold thermal evaporation, where the different thermal expansion coefficients of metal, underlayer and substrate can lead to substantial residual stress upon cooling [29]. Subsequent mechanical impacts, such as the scratch, tape and nanoindentation tests, can result in different types of film disruption depending on the balance between the elasticity of the film and the strength of interactions between the film and the underlayer.

Our morphological investigations indicate a stronger coupling between the underlayer and the gold film for the post-deposition cured film. The post-deposition cured sample shows larger scale ($\sim$1 μm) height fluctuations than the pre-deposition cured sample, which is smoother with feature sizes below 300 nm. One would expect higher yield stress for materials with smaller grain size [30], with all other things being equal, but the morphological features in the gold film are not individual grains in a polycrystalline film. In fact, the longer-scale corrugations and overall film morphology are unique to the post-deposition-cured film. This suggests that the polymer layer can convey morphology and contours to the top metal layer when cured after gold

deposition.

By varying the thickness of the SU-8 underlayer, the roughness can be varied as well, as shown in Table 2.2. The data for both pre- and post-deposition cured methods demonstrate that the gold film morphology is independent of the glass substrate, with resulting roughness controlled by the SU-8 layer. The relation between SU-8 thickness and roughness is not simple, however. The roughness of pre-deposition-cured samples is quite similar (0.90–1.02 nm) regardless of SU-8 thickness, while there is much more variation (1.36–2.01 nm) for the post-deposition-cured samples. While the resulting gold film morphology likely reflects the morphology of the underlying SU-8, different morphologies emerge when the polymer curing takes place in the presence of the gold film. This coupling between the gold and polymer layers also plays a role in the resultant mechanical properties.

The elastic modulus values for both samples are around the 100 GPa value which Moody *et al.* [10] presented in their work. The pre- and post-deposition cured films do not differ significantly in elastic modulus. The large and overlapping distributions of elasticity values are consistent with the large scatter in mechanical properties measured by others for thin films at small indentation depths [31]. The shallower average indentation value required to reach the force set point for the post-deposition cured sample does indicate greater stiffness, which is in fact what we measure (see Table 2.1). The difference in spread between stiffness data and elastic modulus data (which is derived from stiffness) likely arises from differences between the idealized tip shape used to calculate all elastic moduli data and the real (and possibly changing) tip shape.

The plastic deformation seen after destructive nanoindentation for the post-deposition cured film in Figure 2.2(a) is in sharp contrast to the cracking and delamination of the pre-deposition cured film shown in Figure 2.2(b). The PLST experiments also

demonstrate that the post-deposition cured film is significantly stronger (requires a higher load to rupture). AFM scratch tests (PLST) reveal better adhesion for gold films on post-deposition cured SU-8 polymer, and simple tweezer scratch and tape tests confirm this.

Interface structure and composition are two of the most significant factors affecting the performance and dependability of the thin film devices [32]. The data point toward a model in which, during post-deposition cross-linking, the SU-8 chains cross-link around the bottom layer of large and heavy gold atoms (See Appendix B for SU-8 photoresist). This cross-linking and the subsequent shrinkage of polymerized SU-8 due to reduction in free volume trap the bottom layer of gold atoms, resulting in gold-polymer composite structure with overall good adhesion of the gold layer to the cured SU-8 sublayer and the observed robustness of the post-deposition cured film. The gold atoms also impact the post-deposition cross-linking, imposing a spatial disturbance for chains to cross-link completely just beneath the adjacent gold layer. Hence lightly cross-linked SU-8 chains in the vicinity of the gold layer lead to the increased plasticity observed with the destructive nanoindentation (Figure 2.2(a)).

For the post-deposition cured sample, stress introduced during cooling after evaporation can be reduced during this cross-linking stage. The additional stress from macroscopic shrinkage due to cross-linking is relieved through film corrugation: as the film shrinks laterally it can expand normal to the substrate. This creates the uneven film surface observed in the AFM image in Figure 2.4(a).

In contrast, the pre-deposition cured film is smoother and less robust. The coupling between the gold layer and the SU-8 underlayer is much weaker, and it cannot access the stress-reducing mechanisms available in the post-deposition curing process.

2.5 Conclusions

Post-gold-deposition curing of a polymer underlayer is a reliable protocol to have a robust gold thin film satisfying the mechanical requirements for sensors. This protocol can also address issues of subsequent processing/packaging required to develop biomedical cantilever sensors or robust gold substrates for SERS or SPR sensors, where the graded gold–polymer interface can better withstand the issues arising from the different thermal expansion coefficients of the constituents.

The data show that the post-deposition cured samples are more resistant to applied mechanical stresses. The smaller spread in data seen for indentation depths for the post-deposition cured sample is repeated for stiffness and elastic modulus measurements, further emphasizing the more homogeneous and reliable behavior for the post-deposition cured sample.

Finally, the film topography that is translated from the SU-8 sublayer could be of interest for creating a controlled roughness for the "hot spots" used in surface enhanced Raman sensing.

Bibliography

[1] Nordström, M.; Johansson, A.; Sánchez Nogueron, E.; Calleja, M.; Boisen, A. *Microelectron. Eng.* **2005,** *78-79,* 152-157.

[2] Yan, X.; Brown, W. L.; Li, Y.; Papapolymerou, J.; Palego, C.; Hwang, J. C. M.; Vinci, R. P. *J. Microelectromech. Syst.* **2009,** *18,* 570-576.

[3] Wilson, D. M.; Hoyt, S.; Janata, J.; Booksh, K.; Obando, L. *IEEE Sens. J.* **2001,** *1,* 256-274.

[4] Halvorson, R. A.; Vikesland, P. J. *Environ. Sci. Technol.* **2010,** *44,* 7749-7755.

[5] Gordon, R.; Sinton, D.; Kavanagh, K. L.; Brolo, A. G. *Acc. Chem. Res.* **2008,** *41,* 1049-1057.

[6] Taguchi, Y.; Takano, E.; Takeuchi, T. *Langmuir* **2012,** *28,* 7083-7088.

[7] George, M. A.; Glaunsinger, W. S.; Thundat, T.; Lindsay, S. M. *Thin Solid Films* **1990,** *189,* 59-72.

[8] Audino, R.; Destefanis, G.; Gorgellino, F.; Pollino, E.; Tamagno, S. *Thin Solid Films* **1976,** *36,* 343-347.

[9] Kang, K. D.; Burgess, R. R.; Coleman, M. G.; Keil, J. G. *IEEE Trans. Electron Devices* **1969,** *16,* 356-360.

[10] Moody, N. R.; Adams, D. P.; Medlin, D.; Headley, T.; Yang, N.; Volinsky, A. *Int. J. Fract.* **2003,** *119,* 407-419.

[11] Ge, J.; Kivilahti, J. K. *J. Appl. Phys.* **2002,** *92,* 3007-3015.

[12] Johansson, A.; Blagoi, G.; Boisen, A. *Appl. Phys. Lett.* **2006,** *89,* 173505/1-173505/3.

[13] Sameoto, D.; Lee, S.-W.; Parameswaran, M. *J. Micromech. Microeng.* **2008,** *18,* 075023/1-075023/8.

[14] Allara, D. L.; Dwight, D. W. Surface enhanced raman spectroscopy (SERS) substrates exhibiting uniform high enhancement and stability. US 7450227, November 11, 2008.

[15] Cardozo, B. L.; Pang, S. W. *J. Vac. Sci. Technol., B* **2008,** *26,* 2385-2389.

[16] Chen, H. L.; Chuang, S. Y.; Lee, W. H.; Kuo, S. S.; Su, W. F.; Ku, S. L.; Chou, Y. F. *Opt. Express* **2009,** *17,* 1636-1645.

[17] Peng, C.; Cardozo, B. L.; Pang, S. W. *J. Vac. Sci. Technol., B* **2008,** *26,* 632-635.

[18] Palmer, C., Ed.; *Diffraction Grating Handbook;* Thermo RGL: Rochester, New York, 5th ed.; 2005.

[19] Schneider, A.; Ibbotson, R. H.; Dunn, R. J.; Huq, E. *Microelectron. Eng.* **2011,** *88,* 2390-2393.

[20] Godin, M.; Tabard-Cossa, V.; Miyahara, Y.; Monga, T.; Williams, P. J.; Beaulieu, L. Y.; Lennox, R. B.; Grutter, P. *Nanotechnology* **2010,** *21,* 075501/1-075501/8.

[21] Mertens, J.; Calleja, M.; Ramos, D.; Taryn, A.; Tamayo, J. *J. Appl. Phys.* **2007,** *101,* 034904/1-034904/8.

[22] Calleja, M.; Tamayo, J.; Nordström, M.; Boisen, A. *Appl. Phys. Lett.* **2006,** *88,* 113901/1-113901/3.

[23] Hutter, J. L.; Bechhoefer, J. *Rev. Sci. Instrum.* **1993,** *64,* 1868-1873.

[24] Hay, J. L.; Wolff, P. J. *J. Mater. Res.* **2001,** *16,* 1280-1286.

[25] Kumar, R. M.; Merschrod S., E. F.; Poduska, K. M. *Biomacromolecules* **2009,** *10,* 1970-1975.

[26] Kipp, D. O. *Metal Material Data Sheets;* MatWeb - Division of Automation Creation, Inc.: Blacksburg, VA, USA, 2010.

[27] Guo, S.; Akhremitchev, B. B. *Biomacromolecules* **2006,** *7,* 1630-1636.

[28] Pratt, J. R.; Smith, D. T.; Newell, D. B.; Kramar, J. A.; Whitenton, E. *J. Mater. Res.* **2004,** *19,* 366–379.

[29] Audoly, B. *J. Mech. Phys. Solids.* **2000,** *48,* 2315-2332.

[30] Volinsky, A. A.; Moody, N. R.; Gerberich, W. W. *J. Mater. Res.* **2004,** *19,* 2650-2657.

[31] Du, K.; Pang, X.; Chen, C.; Volinsky, A. A. Mechanical properties of evaporated gold films. Hard substrate effect correction. In *Mater. Res. Soc. Symp. Proc.*, Vol. 1086; 2008.

[32] Moody, N. R.; Adams, D. P.; Volinsky, A. A.; Kriese, M. D.; Gerberich, W. W. Annealing effects on interfacial fracture of gold-chromium films in hybrid microcircuits. In *Mater. Res. Soc. Symp. Proc.*, Vol. 586; 2000.

Chapter 3

Annealing Approach to Hot Spots for SERS Substrates: Applications to the Detection of Polycyclic Aromatic Hydrocarbons (PAHs)

3.1 Introduction

Surface enhanced Raman scattering (SERS) is becoming an important sensing technique because of its versatility, allowing for measurements of components in gas, solid, liquid, solution, and suspension form without specific pretreatment [1, 2]. Due to its scattering character, direct laser Raman spectroscopy suffers from weak signals [3]. In SERS based sensors, however, interaction of a molecule with the nanostructured surface of a metal such as silver, gold, or copper leads to a significantly enhanced

Raman signal, allowing trace amounts of contaminants to be detected [3, 4]. As a vibrational spectroscopic technique, SERS provides distinct spectral fingerprints for even quite similar compounds, and unlike IR spectroscopy it can be applied effectively to aqueous samples [5]. However, challenges remain in the application of SERS in sensors which include reproducibility and interpretation of spectra [6].

Surface-enhanced Raman spectroscopy (SERS) presents interesting materials challenges, relying as it does on nanostructured metal films [7]. SERS active substrates may be formed by nanopatterning a film, immobilizing nanoparticles, or other approaches combining features of both of these [8–10]. Sandhyarani *et al.* introduced an inexpensive, simple, one-step method for the preparation of SERS active gold films. They did this by sputter deposition of 200 nm thick gold film on aluminum foil commercially available for packaging purposes. Aiming for a rough surface they oxidized the foil by heating at 500 °C in air for 5 hours prior to gold deposition. They showed the ability of this substrate to obtain good quality Raman spectra using 1064 nm laser from 1,4-benzenedimethanethiol (BDMT) with 70 mW power and from C_nH_{2n+1}(n = 3, 6, 8, 9, 10, 12 and 18) thiols with 300 mW power [9]. Baia *et al.* made their SERS substrates by thermal vapor deposition of 15, 30, and 60 nm gold films onto silica substrates which were coated with a mask of monodisperse layer of polystyrene nanospheres. They investigated the SERS activity for p-aminothiophenol (p-ATP) probe molecules after immersing their substrates for 24 hours in methanolic solution of the probe and with visible (532, 20 mW and 633 nm, 4.3 mW) and NIR (830 nm, 1.1 mW) lasers. They obtained the best result with 850 nm laser on 60 nm thick film [10].

In the study presented in this Chapter, the annealing approach is proposed as a two-step method which starts with fabrication of a continuous gold (Au)/chromium (Cr) bilayer film and results in a nanostructured multilayer with Au or Au-rich islands

on a Cr background. A number of articles have investigated adhesion, diffusion and electrical resistivity properties of Au/Cr bilayer films annealed at different temperatures showing that chromium would be driven into the gold top layer through grain boundaries in the top layer and by dissolving into the gold grains [11–14]. By annealing bilayer Au/Cr films at temperatures around 200 °C, the adhesion of the gold layer to its Cr sublayer is elevated due to diffusion of Cr into the gold top layer [13].

Huang *et al.* studied the effects of temperature (170 °C, 180 °C, 200 °C, and 250 °C) and time (from 5 to 120 minutes) of annealing (under vacuum) on the structural, compositional and electrical properties of Au=110 nm/Cr=20 nm bilayer films sputter-deposited on glass slides [13]. They detected Cr inside the Au layer for the bilayer film annealed at 200 °C for 60 minutes or longer and for the higher temperature of 250 °C regardless of annealing time. They concluded that diffusion of Cr into the Au layer happens when annealing at either 200 °C for 60 minutes and longer or at 250 °C for 5 minutes or so. Also their study revealed that annealing decreases point defects in gold and higher annealing temperatures enlarges grain sizes resulting in lower electrical resistance.

Rairden *et al.* calculated the diffusion coefficients for Au=680 nm/Cr=50 nm films for various annealing temperatures of 250, 300, 400 or 450 °C [11]. They showed that an increase in annealing temperature raises the diffusion coefficient of Cr into Au. They also showed that when the substrate is soda-lime glass some of the chromium reacts with the glass and there will be less chromium available to diffuse into the gold top layer unlike clear fused quartz and silicon wafer substrates. On the other hand they found that the activation energy for bulk diffusion ($\sim$41 kcal/mol) is almost twice that for thin films (25 kcal/mol) due to higher concentration of point defects. In fact the grain size is usually larger in thin films and is around the order of the film thickness [11]. Overall, they attributed the observed diffusion energy to diffusion

via grain boundaries and to some extent via the lattice [11]. Therefore in the project explained in this chapter various thicknesses of gold (all three being less than 50 nm) were applied in order to study the possible effects of varying grain boundary sizes on optical properties and hence SERS activity of as-deposited bilayer and annealed samples.

Huang *et al.* in another work produced Au=110 nm/Cr=50 nm and Au=110 nm/Cr=10 nm films with subsequent annealing at 300 °C for 2, 5 and 30 minutes in a vacuum to investigate the effect of Cr layer thickness on annealed film properties [14]. They realized that for thinner Cr layers the diffusion of Cr into the gold layer is slower but good adhesion to the glass support was achieved for both with the shorter annealing time. Therefore the Cr thickness is intended not to be over $\sim$ 30 nm ($\cong$ the average thickness used by Huang *et al.*).

Moody *et al.* demonstrated that annealing at a higher temperature of 400 °C for longer times of 120 and 480 minutes does not adversely affect the adhesion promoting property of the Cr layer in their sputter deposited Au=200 nm/Cr=6 nm samples [12]. Their work showed that the continuous Cr layer had completely dissolved in the Au layer only after 480 minutes of thermal treatment at 400 °C. Hence the annealing temperatures (325 and 400 °C) and times (60 and 120 minutes) are selected in this Ph.D. thesis to preserve the quality of the gold top layer, and to improve its adhesion to the glass substrate.

In the case of annealed samples the following model presumably applies. Gold islands surrounded by Cr, form upon heating the bilayer, forming a base for the generation of surface plasmons. These gold islands contain gold grains. The Cr which diffuses into the grain boundaries (inter grain spaces) isolates these gold grains just as it does the gold islands. The Cr regions bind phenanthrene molecules (the analyte) to the surface [15–17] in the space in between the gold islands and grains where

the plasmonic field strength is the largest [18], known as hot spots among different research groups [19, 20].

3.1.1 Objectives

Nonetheless, SERS activity depends on the three factors of electromagnetic field in use as an optical enhancer, Raman activity of the analyte under study, and last but not the least, the affinity of the analyte for the plasmonic surface [21]. The purpose of the present work is to develop experimental procedures to make mixed metal films designed for SERS. The design strategy was to exploit the increase of electric fields close to an irradiated corrugated plasmonic surface. Adsorbed analyte molecules interact with evanescent waves from the surface yielding enhancement of Raman responses of vibrational modes [22]. Ultimately, these experiments lead to SERS detection of the analyte. To this end, different protocols were designed to investigate the morphology and the heterogeneity in composition which are actively involved in the enhancement mechanism. In this project higher temperatures of 325 °C and 400 °C for annealing periods of 60 and 120 minutes were used to:

1. enforce corrugation by generating separate metal islands aiming for rough surfaces (to enlarge the available surface area for the analyte to interact with),

2. manipulate grain sizes due to high temperature (to explore optical response properties and resulting SERS effects), and

3. drive Cr diffusion into both gold grains and grain boundaries (to enlarge the presumed phenanthrene adsorption sites).

Phenanthrene is used as a model analyte due to its importance in monitoring in marine environments [2]. The substrate developed in this work is used to detect

0.01 mg/L phenanthrene in ethanol which is lower than the 5 mg/L detection limit (ethanol solution) reached by Du and Jing using thiol-functionalized Fe_3O_4-Ag core-shell magnetic nanoparticles and operating the spectrometer with a 785 nm laser and 4 cm^{-1} resolution [23].

3.2 Experimental

Glass slides (Cole-Parmer precleaned 25 x 75 x 1.00 mm Plain) were rinsed with 95% ethanol, diluted 30% acetic acid and nanopure (Barnstead, 18.2 MΩ·cm) water and then dried with an air gun and cut into three equal pieces with a diamond scribe (SPI).

Metal deposition on glass with a custom-built evaporation chamber used pure chromium and gold sources under vacuum on glass. The aforementioned glass slide pieces were placed on the sample holder disc and mounted 20 cm above the source at the same level with quartz crystal microbalance (QCM) (INFICON XTM/2 deposition monitor) to measure the amount of deposition. Gold foil (Goodfellow, Cambridge, 99.5% purity) and chromium pellets were put in a tungsten boat and a basket (Kurt J. Lesker), respectively. Evaporation was conducted at pressures below 10^{-3} Pa by first evaporating Cr and subsequent evaporation of Au to generate the top layer. Evaporation was stopped by simultaneously placing the shutter in front of the chromium source and turning off the voltage controller to properly finalize the Cr layer deposition. When the chromium basket cooled down, gold deposition was started by reopening the shutter and turning the voltage controller on. Hence the Au top layer was deposited directly on Cr coated glass slides without allowing them to be exposed to air prior to gold deposition. To avoid carbon contamination caused by introduction of air to a hot chamber, substrates were removed after the evaporation

chamber cooled down to ambient temperature.

Bilayer Au/Cr films with three different gold top layer thicknesses of 13, 21 and 42 nm (as displayed by the QCM) were deposited on glass coated with Cr thicknesses of 17, 14 and 31 nm respectively. Au/Cr bilayer films were annealed at either 325 °C or 400 °C. The oven (Thermolyne 114300) was programmed with heating and cooling rates of 100 °C per hour and to stay at the target temperature for either one or two hours. In this way, 12 different gold-chromium mixed film substrates were generated. Also a single layer gold film was made by directly depositing a layer of gold with 145 nm thickness on glass.

AFM images were obtained in tapping mode using an MFP-3D (Asylum Research) atomic force microscope with a silicon tip (tip model number NSC35AlBS, Mikromasch). AFM tapping mode images along with their roughnesses are presented in Appendix C. AFM MFP3D software (Asylum Research) also calculated the surface area of the scanned samples using the quad triangle method (QTM) [24]. In this method every four adjacent pixel centers are assumed to make a rectangle as a group of four triangles which share a central vertex. The height of this central vertex is the averaged height of the four pixels. The program calculates the surface area of the triangles and then moves on to the next four-pixel group. In this way, each pixel participates in four triangles.

Additional morphology data as well as elemental distribution within the mixed film came from scanning electron microscopy (SEM) (FEI Quanta 400) images and energy dispersive X-ray (EDX) (Roëntec Quantax) analysis. In addition to the Raman data of chromium oxide compounds in the literature, which suggests these compounds do not exist in the developed films, to further investigate the possible existence of chromium oxide compounds more structural analysis was performed on the two nominated annealed samples using the Rigaku Ultima-IV Multipurpose X-ray diffraction

system with Cu Kα radiation (40 kV/ 44mA) with sampling width of 0.0200 deg and scan speed of 1.000 deg/min.

The UV-Vis spectra of substrates were measured in reflection using a USB2000 (Ocean Optics) UV-Vis spectrometer. A silvered mirror which has a constant reflectivity in the wavelength range studied here is used as the reference [25]. This set up is recommended by Ocean Optics to assess optical properties of mirrors and coatings [26]. For this the R200-MIXED reflection split fiber probe (for more details see Appendix C and Figures C.5 and C.4 therein) was fixed firmly at a 45° angle to the substrate surface by mounting the probe head in the RPH-1 OceanOptics probe holder (see Figure 3.1 for reflection setup). This ensured that the probe head maintained the same distance and angle with respect to the surface for all measurements. Sampling variables in this study were adjusted to 1200 msec for integration time and an averaging of five readings for each spectrum.

UV-Vis reflection spectra were obtained for a single layer gold film, bilayer Au/Cr films and their annealed counterpart films. The 350 nm – 800 nm range where the plasmon bands (dips in reflection spectra) appear was studied to further investigate the optical properties of these films in order to pinpoint any potential correlation between reflection spectra and SERS. The OOIBase32 software (Ocean Optics) applies Equation 3.1 for the reflection spectrum calculation.

$$R\% = \frac{S - D}{R - D} 100\% \tag{3.1}$$

S is the reflection signal from the sample, D is the dark signal when the light source optical fiber to the sample is blocked and R is the reflection signal from the reference. Therefore sample reflection ($R\%$) is a percentage relative to the reflection from the mirror reference. The 45° angle set up used here (also called diffuse reflection set up)

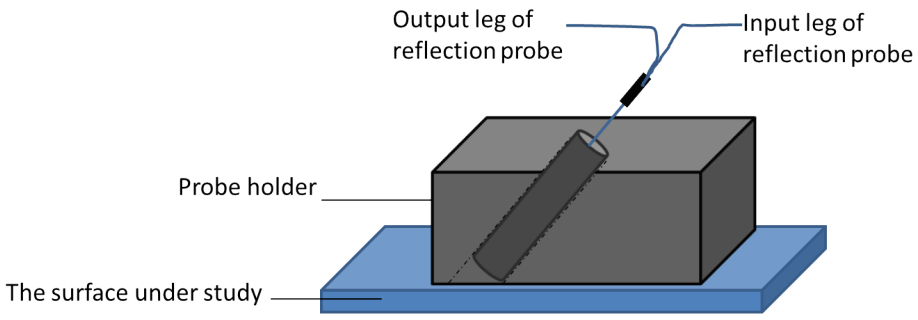

Figure 3.1: Schematic of the reflection setup. The light source sends UV-Vis light through the input leg of the reflection probe to the sample (bottom of the figure). The reflection probe holder holds the probe firmly at a 45 degree angle with respect to the surface. The output leg of the reflection probe collects scattered light at the same angle. (Not drawn to scale.)

illuminates and collects signals at 45° to measure the diffuse reflection property of the sample. For rough samples (thermally treated samples) the reflection intensities are 100% or higher. Since the diffuse reflection is the prominent reflection behavior from rough surfaces and since the reference was a smooth mirror which has a very weak diffuse reflection signal, intensities are larger than 100% for these samples. The spectral data presented here are smoothed using Igor software's (WaveMetrics) built-in binomial algorithm which is a Gaussian filter (original spectra can be found in Appendix C). Two major types of smoothing algorithms are widely used in analytical chemistry: least-square polynomial (LSP) and binomial algorithms. The LSP algorithm suffers from defects, which causes misinterpretation of the results. On the other hand, the binomial algorithm is faster and easier to implement without those problems [27]. Therefore the binomial algorithm was used in this study to smooth the data and determine peak maxima in the UV-Vis spectral data.

Raman spectra were acquired from solid phenanthrene and substrates after they were submerged overnight (12 hours) in 0.001 M (saturated, nearly 178 mg/L), 10 mg/L, 5 mg/L and 0.01 mg/L phenanthrene solution in ethanol and saturated water solution (1.6 mg/L) [28] to check the functionality of the SERS substrate in order to

detect phenanthrene in an aqueous environment. See Appendix C for phenanthrene solubility limit in ethanol and other physical properties which are important here for Raman experiments. After rinsing and drying the substrates, spectra were obtained with a backscattering setup. Raman experiments were done using a confocal Raman scattering spectrometer (HR LabRAM, Jobin Yvon Horiba) equipped with an Olympus BX41 microscope (50X, N.A.=0.50 and 100X, N.A.=0.90), a dispersive grating of 1800 lines/mm, and a 1024 pixel chip CCD detector using a 70 mW, 532 nm excitation laser source. The power density experienced by these samples under a 100X objective lens is either 0.7 x 10^{-4} mW/nm^2 or 0.175 x 10^{-4} mW/nm^2 corresponding to neutral density filters of 1 and 0.6. See Appendix C for explanation of laser power. The confocal hole aperture and slit sizes were respectively 300 μm and 150 μm. The 100X Olympus objective lens (0.90 N.A.) resulted in a laser spot of about 721 nm. See Appendix C for laser spot size calculation. Neutral density filters with either 1 or 0.6 optical densities were used as required. See Appendix C for optical density definition. Spectra were obtained for 2 accumulations with 6 seconds exposure time each.

3.3 Results and Discussion

3.3.1 AFM, SEM, EDX and XRD

According to AFM and scanning electron microscopy (SEM) images shown in Figures 3.2 and 3.3b respectively, the annealed films show regularly sized and distributed regions of varying height and composition. Annealing enforces both dewetting and diffusion at the same time. Annealed samples present higher roughness as opposed to unannealed Au/Cr bilayer samples. The surface area calculated from the AFM images is necessary to account for the analyte concentration on the surface when rationalizing

the SERS enhancing ability of the selected annealed samples to be discussed later in section 3.3.3 (see Table 3.2 for surface area and roughness (rms) values of these samples). Roughness data are calculated by averaging over four areas across each scan. Films annealed at 400 °C and a longer annealing period of two hours show higher roughness (see Figure C.1 in Appendix C).

The SEM image of the annealed film consists of dark, gray and bright regions corresponding to how poor (darker) or rich (brighter) they are in their gold content, as indicated by EDX spectra (see Figure 3.4). The peaks for other elements in Figure 3.4 come from the glass substrate. The chromium is present in all regions (see also elemental analysis map presented in Figure 3.5b). This demonstrates a homogeneous chromium distribution across the sample while gold shows distinctive segregation (see Figure 3.5a) which generates gold islands. The gold-rich islands are of interest for their plasmon enhancing character. EDX spectra and imaging are consistent with Cr also being present in the grain boundary regions within the corrugated gold islands, although this cannot be directly seen in the SEM images as the individual gold grains are not resolved. The SEM/EDX is simply not the instrument of choice for the evidence of grain boundaries.

Because of the large penetration depth of the 15 keV electron beam used in SEM and EDX studies which is in the range of 1–3 μm (large compared to the annealed film thickness, which is in the range of 30–70 nm), signals from the underlying Cr layer would appear in all three EDX spectra obtained from bright, gray and dark regions. Therefore, EDX cannot definitively identify the bright regions as gold islands on a chromium sublayer or a gold-rich alloy. However, the Cr map (see Figure 3.5b) clearly reveals the presence of Cr throughout, perhaps as a continuous underlayer.

The Au=42 nm/Cr=31 nm sample annealed for 2 h at 400 °C was selected for further structural analysis to reveal information about the possible presence of chromium

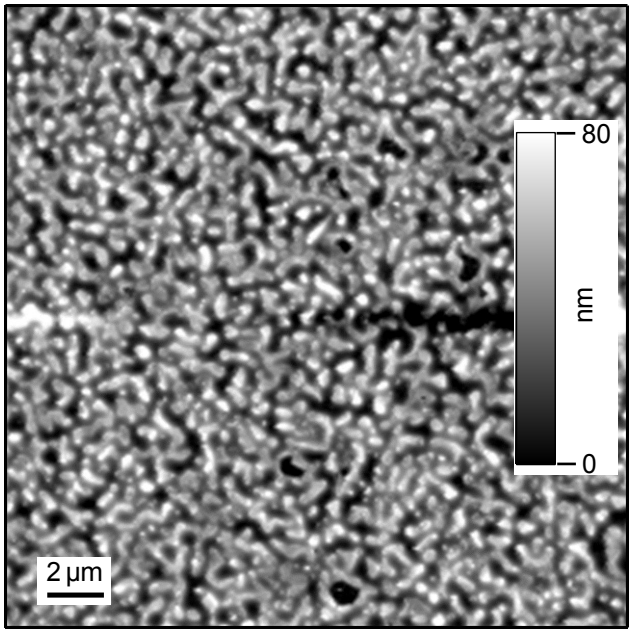

Figure 3.2: AFM height channel image of a gold-chromium annealed film, showing regularly-spaced and -sized islands.

oxide (see Figure 3.6). The X-ray diffraction (XRD) data in Figure 3.6 indicate the presence of Au and Cr but not of Cr_2O_3 or CrO_2 compounds which were expected to give peaks at 2θ values of 43° (CrO_2), 51° and 55° (Cr_2O_3) based on the literature [29]. All peaks in the XRD spectra match those for Au, with the dominant (111) peak at 38.2° indicating the expected (111) texture [14]. The XRD database identified Cr peaks, which are shown with arrows, are at similar positions as the Au peaks. These Cr peaks are indicative of crystalline elemental Cr.

3.3.2 UV-Vis reflection spectra

UV-Vis reflection spectra were obtained to further understand the effect of the thickness and annealing procedure on optical properties of developed substrates despite the fact that, as explained by Moskovits, SERS intensity does not always correlate with the extinction spectrum of SERS substrate [19].

The overall intensity in the UV-Vis spectra presented in Figures 3.7 and 3.8 pro-

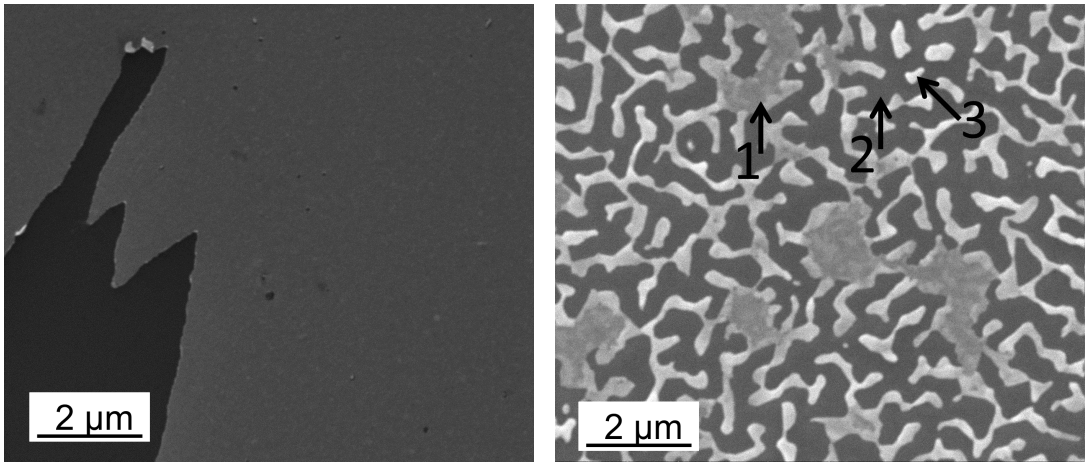

(a) (b)

Figure 3.3: SEM images of the a) gold on a chromium bilayer and b) gold-chromium annealed films. The contrast variations in b show segregated regions. The arrows 1, 2, and 3 point to a gray, dark, and bright region (gold island) respectively. Representative EDX spectra of these three regions are shown in Figure 3.4.

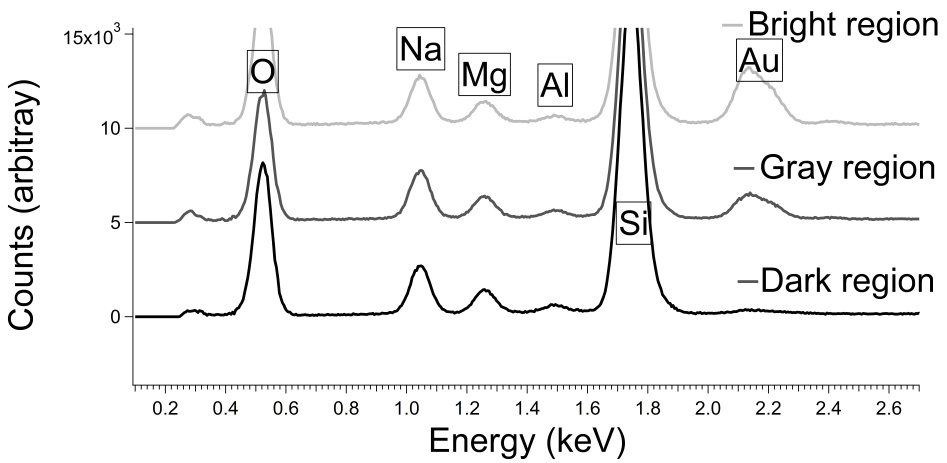

Figure 3.4: EDX spectra show gold content of three regions in an annealed film based on the M line X-ray at 2.120 keV. The strong oxygen Kα line X-ray at 0.525 keV does not allow the detection of the adjacent chromium Lα line X-ray at 0.573 keV. Other elemental signals come from the underlying glass substrate. This could be correspondingly seen in the elemental map in Figure 3.5.

vides information regarding the films' reflection/scattering properties: a higher intensity corresponds to a larger diffuse reflection. Corresponding UV-Vis reflection spectra for bilayer and selected annealed films are presented separately in Figures 3.7 and 3.8 respectively because of the above mentioned significant difference in their reflection intensities. The dips in the reflection spectra correspond to absorption of UV-Vis light by the surface and are related to surface plasmon bands. Annealed films, especially those annealed at 400 °C, show significant diffuse reflection as opposed to those annealed at 325 °C and those of bilayer films. In Figure 3.8 only optical properties of those samples annealed at 400 °C are presented and will be discussed here.

3.3.2.1 Reflection intensity correlation with SERS; Au=42 nm/Cr=31 nm, 400 °C sample

The intensity of the UV-Vis spectrum for Au=42 nm/Cr=31 nm, 400 °C, 2 h yields insight as to why specifically this substrate consistently showed the largest Raman baseline intensity (see related spectra in Figures 3.12 and 3.8.). In fact these two

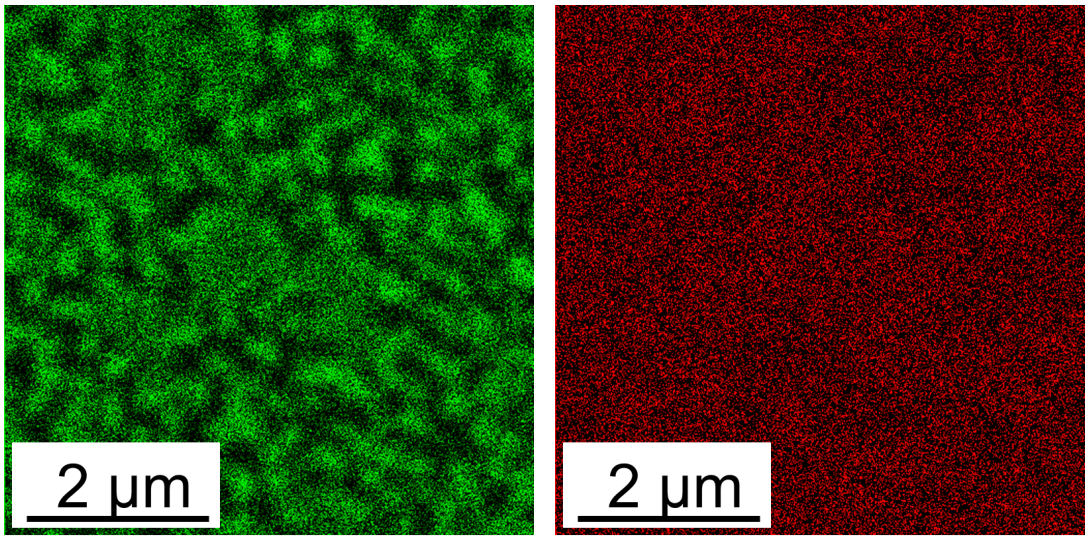

(a) (b)

Figure 3.5: Elemental map of an annealed sample in the same field presented in SEM image in Figure 3.3b. a) The green dots show gold distribution in the annealed film. (M line, 2.120 keV signal); b) The red dots show chromium distribution along the same image. This shows chromium is present in all three regions. (Kα line, 5.411 keV signal)

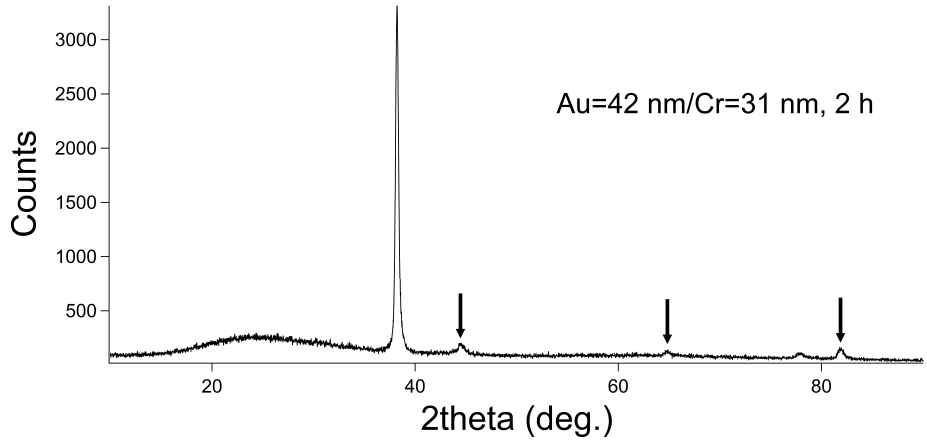

Figure 3.6: XRD pattern of a Au=42 nm/Cr=31 nm film annealed at 400 °C for 2 hours (2 h). All peaks correspond to Au, with arrows indicating peaks which also coincide with Cr.

observations are consistent because a sample with larger diffuse reflection is able to generate larger scattering when the laser interacts with the substrate surface in Raman measurements.

3.3.2.2 Reflection intensity and maximum peak position; bilayer films

In the case of the bilayer films in Figure 3.7, the overall reflection intensity is directly proportional to the initial gold layer thickness, with the single layer 145 nm gold film showing the most intense reflection (see Figure 3.7). Another behavior seen here is that the maximum reflection wavelength is decreasing (shifting to higher energies) as the maximum reflection intensity increases for bilayer films with the increase in gold layer thickness (see Table 3.1). The intensity of the reflection spectra of the bilayer films appears to show an increase with the increase in roughness values (Au=42 nm/Cr=31 nm, roughness 4.03 ± 1.68 nm) > (Au=21 nm/Cr=14 nm, roughness 3.34 ± 1.18 nm) > (Au=13 nm/Cr=17 nm, roughness 2.87 ± 0.13 nm). However, the differences between roughnesses are not statistically significant. For the single layer gold substrate with the lowest roughness value of 1.42 ± 0.72 nm the intensity is the

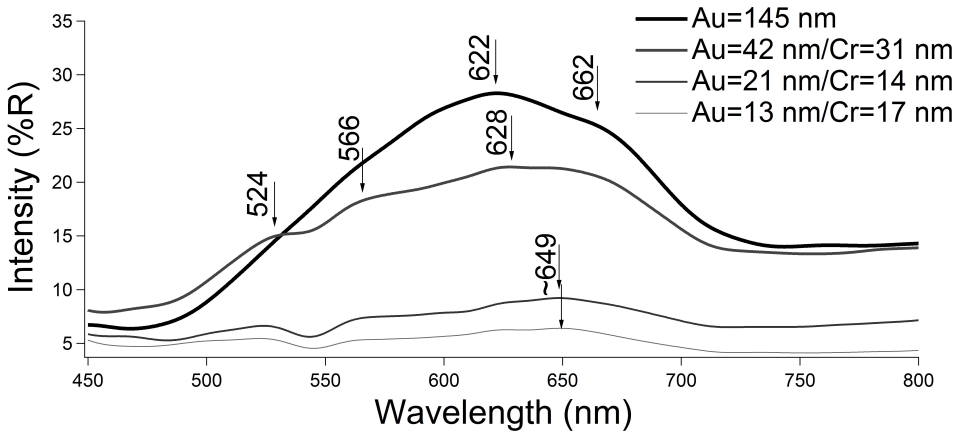

Figure 3.7: UV-Vis reflection spectra of bilayer films and a single layer gold film (smoothed data). The reflection of bilayer films correlates with the gold thickness.

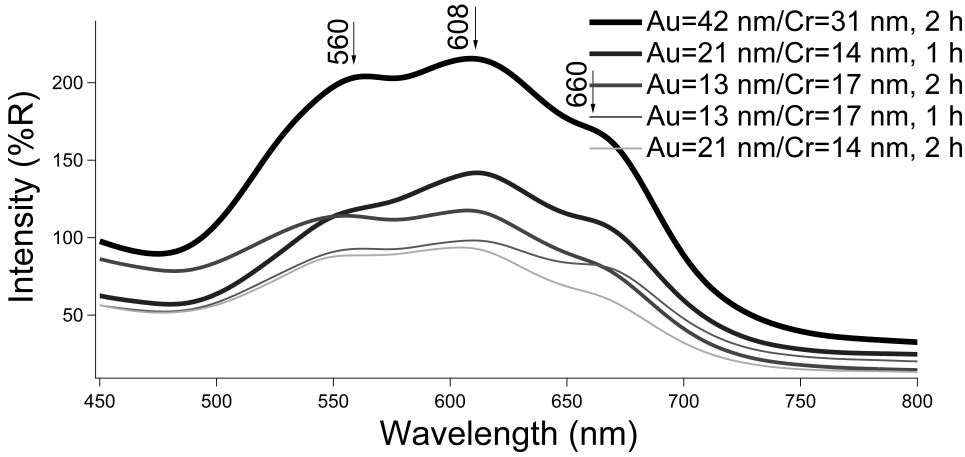

Figure 3.8: UV-Vis reflection spectra of films annealed at 400 °C for 1 hour (1 h) or 2 hours (2 h) (smoothed data). Annealed films show higher intensity reflection.

largest. This could be related to the grain size being the largest of all in this substrate since grain sizes are generally on the order of the actual film thickness [11]. Therefore the thickest film having the largest grain size is a better scatterer resulting in a more intense UV-Vis reflection spectrum.

3.3.2.3 Reflection intensity; annealed vs. bilayer samples

The annealed samples present more intense reflection in their UV-Vis spectra than do the bilayer films. Gadenne *et al.* [30] investigated properties of Au-Cr thin films where

the various Au/Cr ratios were co-deposited by evaporation and sputtering methods on glass and polymer substrates for their applications as optical data storage media. They reported results for crystallographic, optical (reflection, transmittance) and electrical resistivity measurements as a function of film composition and deposition method for fresh (as deposited), aged and annealed films. For Au/Cr annealed films, based on the work by Gadenne *et al.* one can expect higher reflection values and lower transmittance for films with higher Cr content [30]. This is in line with the observation of high reflection intensities for films annealed at higher temperature of 400 °C and for longer time where higher diffusion rates of Cr into Au are expected [11]. The trend seen here for reflection intensities for annealed samples does not follow their roughness trend (see Figure C.1 in Appendix C for roughness values).

3.3.2.4 Features in UV-Vis reflection spectra

In the reflection spectra of the gold film two adjacent maxima appear: one at 662 nm and another at 622 nm with a larger intensity. (Peak positions or maxima are identified as the wavelength of maximum intensity within that wavelength region.) For the Au/Cr bilayer films two extra shoulder-like maxima appear at about 566 nm and 524 nm which could be due to the presence of the Cr underlayer film modifying the surface electric field of the top gold layer.

For annealed samples the dip between the two adjacent maxima on the left side becomes more distinct. The peak at about 524 nm (seen in bilayer films) disappears and the 566 nm peak (seen in bilayer films) becomes more intense and red-shifted toward 560 nm. Possibly the peak at 608 nm is the blue-shifted 622 nm gold peak. For example, for Au=42 nm/Cr=31 nm annealed for two hours at 400 °C the three maxima appear at 560, 608 and 660 nm with the reflection peak at 608 nm being the most intense one.

Table 3.1: Wavelength of maximum reflection (λ_{max}) for bilayer films. There is a blue-shift as the gold layer thickness increases.

Sample	λ_{max} (nm)
Au=145 nm single layer film	622.2
Au=42 nm/Cr=31 nm bilayer film	628.2
Au=21 nm/Cr=21 nm bilayer film	648.5
Au=13 nm/Cr=17 nm bilayer film	649.1

For annealed samples the appearance of the peak at 560 nm, which is not present in the gold film, possibly increases scattering from the excitation laser (532 nm) of Raman resulting in the large SERS effect for this annealed sample. The new dip between 608 nm and 560 nm could be related to the anisotropic dimensions of the gold features seen in the SEM image (Figure 3.3) as such splits in UV-Vis spectra are expected when nanoparticles possess unequal axes [31]. This will also have an effect on the nonlinearity of Raman responses (peak heights) seen for the adsorbed analyte on the Au=42 nm/Cr=31 nm, 400 °C, 2 h when exposed to various concentrations of analyte, as will be discussed in section 3.3.3.

Inhomogeneity in size, shape and thickness of gold features across the sample along with dissimilar Au-Cr composition due to different diffused chromium content between different annealed samples all affect the reflection spectra, where the nonidentical bandwidths add up to the complexity of these UV-Vis spectra. Therefore it is not possible to clearly identify the source of the every feature seen in the UV-Vis spectra. However, it is clear that thermally induced dewetting and Cr diffusion into gold islands in annealed samples are responsible for the larger reflection intensities and the various shapes of the UV-Vis spectra.

3.3.3 Raman data

The Raman spectra in Figures 3.10, 3.11, and 3.12 are for parent bilayer films and their developed annealed films which were immersed in 0.01 mg/L phenanthrene solution overnight (for 12 hours). Such long exposure times are not necessary: the analyte peak is also visible in the spectra from an annealed substrate which was immersed in various concentrations for 5 seconds (Figure 3.13). SER spectra were obtained at different points for each sample. At each point three SER spectra were obtained to study the possibility of phenanthrene thermal and photodecomposition under laser excitation. Characteristic Raman peaks of phenanthrene were observed inconsistently as discussed below in section 3.3.3.3, but the peak around 540 cm^{-1} appears to be the most reliable enhanced peak for phenanthrene adsorbed on all the annealed samples.

Photodecomposition was not seen for normal Raman (not SERS) spectra from solid-state phenanthrene under prolonged (10 minutes) exposure. Phenanthrene was detected from ethanol solutions with concentrations as low as 0.01 mg/L using the SERS substrates developed here. The solubility limit of phenanthrene in seawater is 0.6 mg/L [28]. Therefore the detection at such concentrations offered by these substrates provides a basis for sensor applications in the marine environment.

3.3.3.1 Identification of characteristic Raman peaks

Among SERS peak values being observed for the analyte, the peak around 540 cm^{-1} appears to be the most enhanced peak which is consistently present for various concentrations of phenanthrene solutions adsorbed on all as-deposited bilayer and annealed samples (Figures 3.10, 3.11, 3.12 and 3.13). This peak is assigned to a phenanthrene CCC bending mode (546 cm^{-1} [21]) based on comparison to the phenanthrene spectra in the work by Alajtal *et al.* obtained using 514 nm, 633 nm, 785 nm and 1064 nm excitation lasers [21]. See Figure C.6 in Appendix C for these normal Raman (not

SERS) spectra of phenanthrene. Other characteristic peaks expected for the analyte based on the Raman spectrum of solid state phenanthrene are often quenched or absent in SERS studies carried out here due to either dominant superimposed fluorescence signals possibly from both substrate and adsorbed molecule or absorption of scattered Raman light by the SERS substrate [32]. This is inevitable in this study, where only a high energy (532 nm) excitation laser is being used.

The UV-Vis absorption band maximum for phenanthrene is at 250 nm [33] and hence no resonant Raman or fluorescence signal would be expected from the probe molecule when a lower energy 532 nm laser is employed. However, Alajtal *et al.* reported some residual fluorescence with a 514 nm laser [21]. In the case of the SERS spectrum, one cannot rule out fluorescence effects merely based on a bulk or solution optical absorption measurement since the molecular structure (and hence its optical absorption spectrum) might have been modified as a consequence of adsorption on the surface as well as under the effect of the strong plasmonic field which is present on the surface under Raman laser excitation. Compared to the work presented in this thesis, Due *et al.* in their study were able to see more peaks (eight peaks) in the SER spectra of phenanthrene. However, this is not unexpected as in their case phenanthrene is attracted to the surface due to the hydrophobic character of the functionalized surface where there is no chemical binding of phenanthrene with thiol-functionalized Fe_3O_4-Ag core-shell magnetic nanoparticles [23].

In Figure 3.12 for Au=42 nm/Cr=31 nm, 400 °C, 2 h there is a peak at 300 cm^{-1} which is also present for Au=42 nm/Cr=31 nm, 325 °C, 1 h at 298 cm^{-1} in Figure 3.11 but with a lower intensity. This peak could be assigned to PAH-Cr stretching at 290 cm^{-1} as found by Arrais *et al.* where they studied spectroscopic properties of $[\eta-PAH]Cr(CO)_3$ complexes (PAH= pyrene, perylene, chrysene and 1-2,benzenthracene) [16].

It is important to recognize any possible features in SER spectra that could be introduced by the substrate itself in order to reliably attribute the observed SERS peaks to the analyte. Due to annealing it could be suspected that chromium oxide introduces additional signals to the Raman spectrum. Sousa *et al.* in their Raman study of chromium oxide with 514 nm laser excitation could detect two types of oxides: CrO_2 and Cr_2O_3. They showed that four Raman peaks at 355, 530, 555 and 615 cm^{-1} are attributed to Cr_2O_3 with the peak at 555 cm^{-1} being the most significant. CrO_2 illustrates only one Raman peak at 700 cm^{-1} [29] (see Figure 3.9). The Raman spectra of the annealed samples developed in this work do not exhibit any of these peaks. This possibility is further ruled out due to the persistence observation of the same peak for the non-annealed bilayer and single layer gold substrates (see Figure 3.10). As mentioned above (Section 3.3.1), there is also no evidence of crystalline chromium oxides in the XRD data.

Major possible photodecomposition products of phenanthrene, are (1,1'-biphenyl)-2,2'-dicarboxaldehyde and phenanthrenedione, as reported by Kou *et al.* [34]. They investigated the possibility of photodegradation of phenanthrene via photosensitized electron transfer under visible light ($\lambda \geq 450$ nm) irradiation in the presence of each of the cation solutions of Cr^{3+}, Mn^{2+}, Fe^{3+}, Co^{2+}, Ni^{2+}, Cu^{2+}, and Zn^{2+}. They discovered such behavior only in the presence of Fe^{3+}. Here none of the peaks is related to those products. For example the carbonyl groups in both of the products were not seen at $\sim$ 1700 cm^{-1} in the SER spectra of annealed samples exposed to phenanthrene (see Figure C.7 in Appendix C). Furthermore, apart from the possibility of ion impurities in the metal film, there is no source of Fe^{3+} in our samples to catalyze this degradation pathway. Amorphous carbon is known for its Raman bands at 1580 cm^{-1} and 1330 cm^{-1} [35]. Similar features of these Raman bands also seen here (Figure C.7 in Appendix C). This suggests two possibilities: organic species are burnt

as the laser impinges on the surface, or carbon contamination has been introduced by the metal evaporator and/or the annealing oven. To confidently attribute the 540 cm^{-1} band to phenanthrene, amid these other possible sources of Raman signal, reference spectra should be taken of the substrates before exposing to the analyte.

3.3.3.2 Variability in CCC bending peak position

The small difference in peak position from Alajtal [21] could be in line with phenanthrene being chemisorbed in this work as opposed to Alajtal's study of phenanthrene in the solid state. In the present case π electrons are donated to free orbitals in chromium [15]. This could conceivably result in weaker C-C bonds and hence lower energy for CCC bending [16].

Differences for the CCC bending peak position in SER spectra of phenanthrene on different substrates as seen in Figure 3.12 could be linked with the vibrational Stark effect where molecular vibration energies are perturbed by a local electrostatic field resulting in induced changes in their infrared and Raman spectra [36]. Since this local electric field is characteristic of the substrate, the adsorbed molecule on each substrate experiences a different field.

3.3.3.3 Variability in phenanthrene SER spectra

The SER spectrum of phenanthrene on single layer Au=145 nm film has two other distinctive peaks at 1356 cm^{-1} (either of 1350 or 1362 cm^{-1} [21]) and 1423 cm^{-1} (either of 1418 or 1429 cm^{-1} [21]) which are identified in the work by Alajtal *et al.* as being related to C-C stretching/ HCC bending. Since in the SER spectrum the signal comes from phenanthrene adsorbed on the surface and the molecular structure is affected by surface plasmonic field, the observed SER peaks could be related to any of the above mentioned values reported in the Raman spectrum (non-SERS) of

solid-state phenanthrene. The SER spectrum on the Au=42 nm/Cr=31 nm bilayer film interestingly shows one new peak at 846 cm^{-1} which is not present for other as-deposited bilayer substrates. This could be related to a mode at 828 cm^{-1} reported for solid phenanthrene by Alajtal *et al.* which is a CCC bending in plane ring deformation (see Table 4.5 in Chapter 4). The shifts from normal Raman values suggest different possibilities for adsorption geometries of phenanthrene on the surface, still leaving room for more discussion as to why only these certain peaks occasionally appear in the SER spectra.

For annealed substrates, in addition to the CCC bending peak, SER peaks also appear at about 1382 cm^{-1} (either a 1362 cm^{-1} medium intensity shoulder or 1402 cm^{-1} weak shoulder for C-C stretching, HCC bending) and 1576 cm^{-1} (1570 cm^{-1} medium intensity for C-C stretching) presented in Appendix C. The peak values within parentheses are expected literature values [21] for the normal Raman spectrum of solid phenanthrene. As discussed in Section 3.3.3.1, this observation is also in line with the presence of carbon contamination.

3.3.3.4 SERS enhancement

Raman enhancement for the analyte adsorbed on bilayer films is directly proportional to the thickness of the gold top layer thickness and is largest for the single layer gold film. Figure 3.10 illustrates as-deposited bilayer films SER activity for CCC bending (see Table 3.2 for CCC bending peak heights). According to this observation, signal enhancement is related to the UV-Vis spectrum reflection intensity of each substrate.

SER spectra of adsorbed phenanthrene on annealed samples of bilayer films with the thickest gold top layer (Au=42 nm), when compared to annealed samples with thinner initial gold layers (Au=21 nm and 13 nm), show larger peak heights. Figure 3.11 e.g. shows the Raman activity of Au=21 nm/Cr=14 nm, 325 °C, 1 h (peak

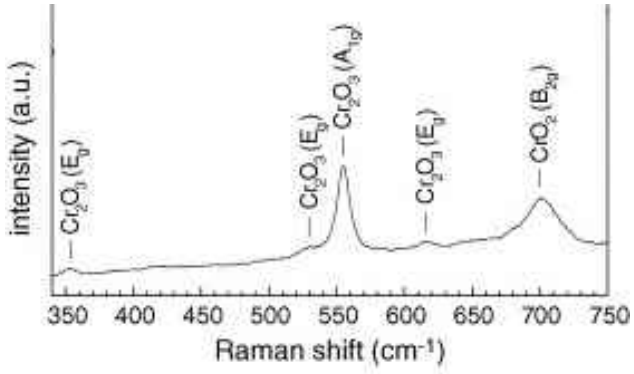

Figure 3.9: Raman spectrum of chromium oxide film which is normalized to its Cr_2O_3 A_{1g} peak intensity (used with permission from [29]).

height 65 counts, roughness 22.35 ± 2.81 nm) and Au=42 nm/Cr=31 nm, 325 °C, 1 h (peak height 325 counts, roughness 26.72 ± 5.94 nm) samples both annealed at 325 °C for 1 hour where phenanthrene CCC bending peak is five times larger for the latter sample with the peak height of 325 counts.

The sample with the thickest initial gold layer (Au=42 nm/Cr=31 nm), annealed at 400 °C and for the longer period of 2 hours, shows the highest enhancement for the CCC bending molecular vibration over the other samples (see Figure 3.12). Using this substrate, the analyte was detected for all tested concentrations and adsorption times between a few hours and a few seconds (see Figure 3.13). This high phenanthrene signal from the annealed substrates could be not only because of the higher intensity of the stronger plasmonic field on the surface of the sample annealed at 400 °C for 2 hours but also the larger concentration of phenanthrene on this sample because of the higher area of Cr available compared to other samples annealed at lower temperatures. The Cr regions are thought to act as a trap for phenanthrene [17]. Therefore, this annealed sample may have a higher concentration of analyte in the focal area as well as a stronger plasmonic field on the surface as its unique UV-Vis spectrum suggests.

Equation 3.2 was used to calculate the signal enhancing quality of the developed substrates. This equation accounts for the extra signal from larger concentrations of

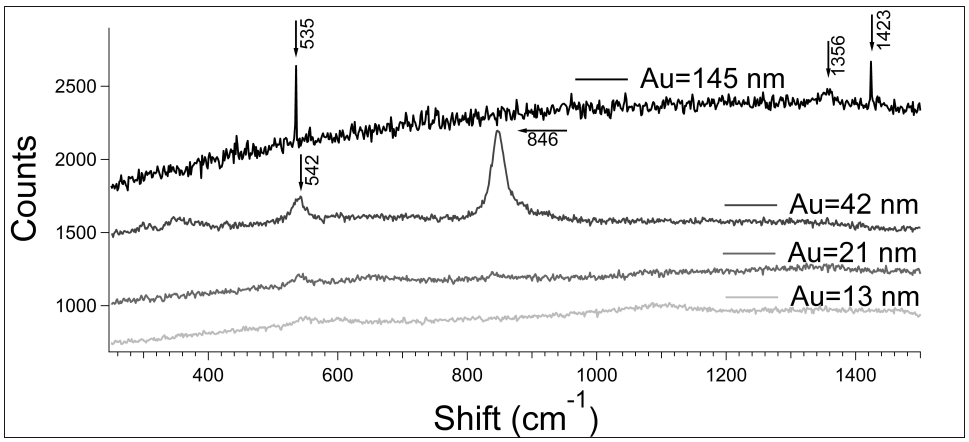

Figure 3.10: SERS activity of as deposited bilayer films and the single layer gold film. Substrates were submerged overnight in a 0.01 mg/L phenanthrene solution in ethanol. The single layer gold film provides the highest enhancement for the CCC bending among the others. The SER intensity with different substrates correlates with their UV-Vis spectra intensity.

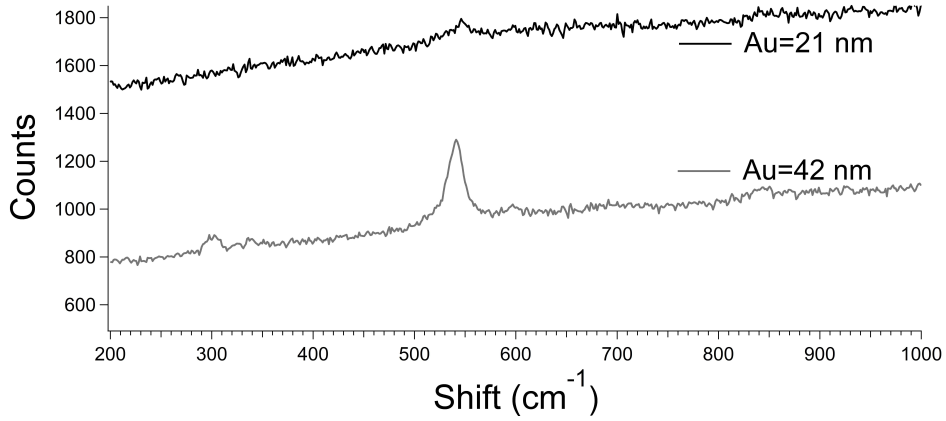

Figure 3.11: SERS activity of Au=21 nm/Cr=14 nm and Au=42 nm/Cr=31 nm samples annealed at 325 °C for 1 hour (1 h) showing that the sample with the thicker initial gold layer gives higher enhancement. CCC bending peak positions are at 546 cm^{-1} for the former and at 541 cm^{-1} for the latter along with a peak at 298 cm^{-1} which can be related to PAH-Cr. Both substrates here were immersed in a 0.01 mg/L solution of phenanthrene in ethanol overnight.

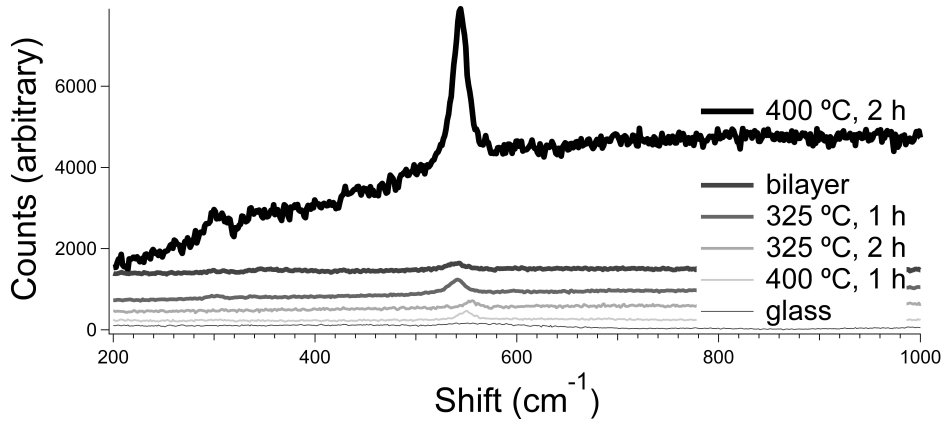

Figure 3.12: SERS activity comparison for Au=42 nm/Cr=31 nm as-deposited bilayer sample and its variously annealed counterparts, all being exposed to a phenanthrene solution of 0.01 mg/L in ethanol overnight. 1 h and 2 h in the annotations mean annealed for 1 hour and 2 hours respectively. The Raman spectrum for the 400 °C, 2 h sample is offset downward to fit in the plot. Positions of CCC bending peak from top to bottom are 544 cm^{-1}, 542 cm^{-1}, 541 cm^{-1}, 556 cm^{-1}, 551 cm^{-1}, and no CCC bending peak for glass slide. Also seen for 400 °C, 2 h sample is a peak at 300 cm^{-1} which can be related to PAH-Cr.

adsorbed molecules on rougher (higher surface area) annealed samples (see Table 3.2).

$$\text{Enhancement} = \frac{I_{\text{annealed}}/I_{\text{bilayer}}}{A_{\text{annealed}}/A_{\text{bilayer}}} \tag{3.2}$$

I_{annealed} stands for the phenanthrene CCC bending peak height at about 540 cm^{-1} and I_{bilayer} is the same for the as-deposited bilayer sample. $A_{\text{annealed}}/A_{\text{bilayer}}$ is the ratio of surface area of the annealed sample to the as-deposited bilayer sample. The enhancement values for SERS substrates fabricated from annealing of the Au=42 nm/Cr=31 nm bilayer are collected in Table 3.2.

Phenanthrene was detected when the Au=42 nm/Cr=31 nm, 400 °C, 2 h substrate was immersed in analyte solution even for 5 seconds (see Figure 3.13). The signal intensity for the CCC bending on this substrate shows an increase with the increase in analyte concentration (see Figure 3.13). The highest concentration solution (178 mg/L, saturated, nearly 20 times more concentrated than the 10 mg/L solution)

Table 3.2: Raman peak heights (for CCC bending), roughnesses, and surface areas for different SERS substrates. The calculated increased surface areas and the SERS enhancements are also tabulated. The roughness and surface area are obtained from a 20x20 μm AFM scan except for the marked ones where 5x5 μm scan was used. The Raman enhancement ratios for annealed samples of Au=42 nm/Cr=31 nm are calculated relative to their parent as-deposited bilayers using Equation 3.2 as explained in the text. Peak height values are from SERS data for substrates which were submerged in 0.01 mg/L phenanthrene solutions. Roughness data are calculated by averaging over four areas across each scan.

Sample	Peak height counts	Roughness nm	surface area μm^2	Increased surface area due to roughness	SERS enhancement
Au=42 nm/Cr=31 nm, 400 °C, 2 h	3565	97.59 ± 13.04	468.1	1.170	23.4
Au=42 nm/Cr=31 nm, 400 °C, 1 h*	195	11.00 ± 0.71	25.9	1.04	1.48
Au=42 nm/Cr=31 nm, 325 °C, 2 h	191	44.65 ± 7.66	451.3	1.128	1.30
Au=42 nm/Cr=31 nm, 325 °C, 1 h	325	26.72 ± 5.94	402.4	1.006	2.36
Au=42 nm/Cr=31 nm*	130	4.03 ± 1.68	25.7	1.03	
Au=21 nm/Cr=14 nm*	64	3.34 ± 1.18	25.2	1.01	
Au=13 nm/Cr=17 nm	44	2.87 ± 0.13	400.7	1.002	
Au=145 nm	558	1.42 ± 0.72	400.0	1.000	

* for a smaller 5x5 μm AFM scan

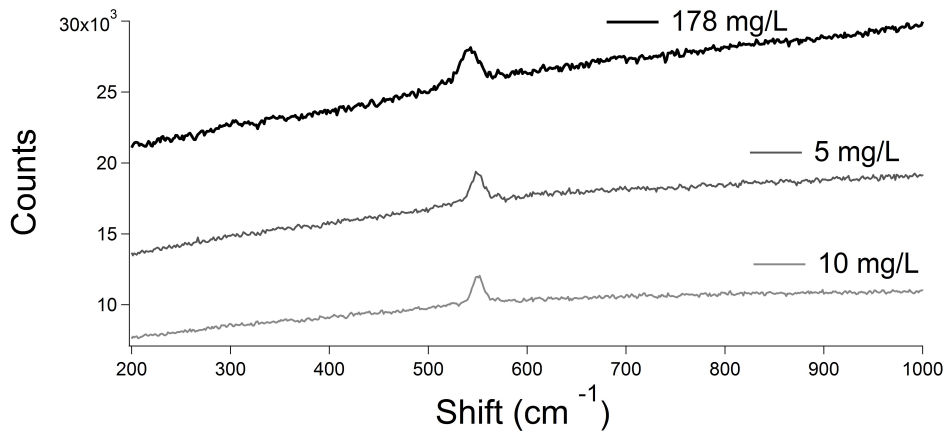

Figure 3.13: The Au=42 nm/Cr=31 nm sample annealed at 400 °C for 2 hours (2 h) shows sufficient SERS activity for detecting the analyte (phenanthrene) at various concentrations when immersed in ethanol solutions for 5 seconds. CCC bending peak positions from top to bottom are similar (543 cm^{-1}, 548 cm^{-1}, and 548 cm^{-1}.)

does result in a larger SER peak for CCC bending, but neither peak height nor peak area scale with concentration. Apart from various issues which contribute to the difficulty in quantitation for SERS as explained by Pieczonka and Aroca [6], related to inconsistencies in peak position, peak appearance, peak intensity degradation (due to photodesorption, photobleaching and photodegradation) and bandwidth, the results in this work indicate that low concentrations of phenanthrene are easily detected with these substrates both in water and ethanol solutions.

The Raman spectrum for solid phenanthrene presented in Figure 3.14 shows distinct peaks comprising a fingerprint of phenanthrene. Raman spectra of 10 mg/L phenanthrene solution are also presented in Figure 3.14. Since few peaks appeared with the collection time of 6 seconds used elsewhere, the exposure time was increased to 60 seconds, with the resulting spectrum also shown in Figure 3.14. In this case peaks start to appear but with a very low signal to noise ratio. A comparison of these results with SER spectra clearly illustrates the efficacy of the developed substrates in the detection of trace phenanthrene concentrations. The peak height of CCC for solid phenanthrene is 486 counts which is not outstanding when compared to the SER

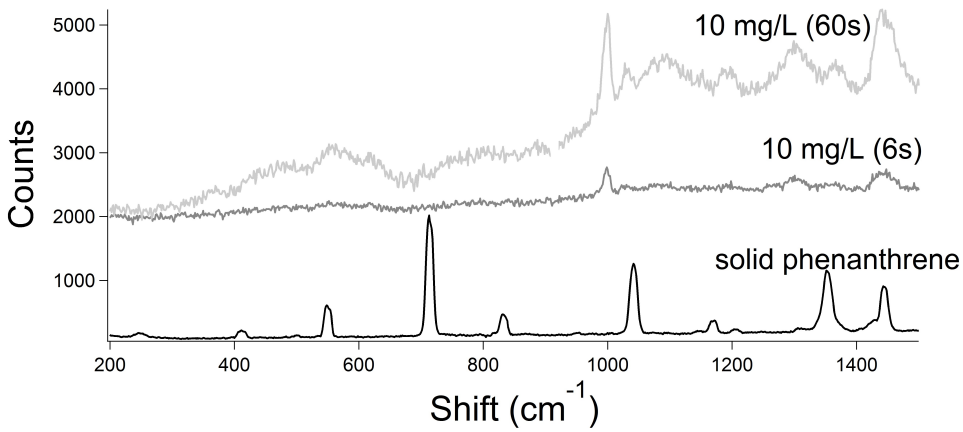

Figure 3.14: Experimental normal Raman spectra (not SERS) for solid phenanthrene and its 10 mg/L solution (in ethanol) collected with 532 nm laser excitation using a 50X objective lens and 2 acquisitions, each of 6 seconds. One spectrum is obtained with 60 seconds of exposure time to obtain higher signal to noise ratio for the solution.

height of 3546 counts attainable with Au=42 nm/Cr=31 nm, 400 °C, 2 h. Other SER peak height values in Table 3.2 are smaller compared to solid phenanthrene, but given that the adsorbed phenanthrene coverage on the SERS substrate is not comparable to a pure bulk solid, one can see the importance of the SERS substrates developed here in qualitative detection of trace concentrations.

3.4 Conclusions

Textured gold and chromium surfaces act as SERS active substrates. The Cr underlayer which dissolves into the gold islands as a result of annealing seems to act as a trap for phenanthrene, since it has a tendency to bind organic analytes [17]. The microscale corrugation and nanoscale roughness, along with the mixed metal islands, the characteristic features of the annealing approach taken herein, appear to provide affinity for the phenanthrene and generate the enhancement that allows the detection of low concentrations of phenanthrene from solution. Additional experiments and data are necessary to conclusively determine SERS activity e.g. obtaining Raman re-

sponse of SERS substrates when not exposed to analyte, studying a different analyte like anthracene, and use of a lower power laser.

Bibliography

[1] Alvarez-Puebla, R. A.; Liz-Marzán, L. M. *Angew. Chem. Int. Ed.* **2012,** *51,* 11214-11223.

[2] Pfannkuche, J.; Lubecki, L.; Schmidt, H.; Kowalewska, G.; Kronfeldt, H.-D. *Mar. Pollut. Bull.* **2012,** *64,* 614-626.

[3] Baker, G. A.; Moore, D. S. *Anal. Bioanal. Chem.* **2005,** *382,* 1751-1770.

[4] Cialla, D.; März, A.; Böhme, R.; Theil, F.; Weber, K.; Schmitt, M.; Popp, J. *Anal. Bioanal. Chem.* **2012,** *403,* 27-54.

[5] Wilson, D. M.; Hoyt, S.; Janata, J.; Booksh, K.; Obando, L. *IEEE Sens. J.* **2001,** *1,* 256-274.

[6] Pieczonka, N.; Aroca, R. *ChemPhysChem* **2005,** *6,* 2473-2484.

[7] Vo-Dinh, T. *Trends Analyt. Chem.* **1998,** *17,* 557-582.

[8] Lin, X.-M.; Cui, Y.; Xu, Y.-H.; Ren, B.; Tian, Z.-Q. *Anal. Bioanal. Chem.* **2009,** *394,* 1729-1745.

[9] Sandhyarani, N.; Murty, K. V. G. K.; Pradeep, T. *J. Raman Spectrosc.* **1998,** *29,* 359-363.

[10] Baia, L.; Baia, M.; Popp, J.; Astilean, S. *J. Phys. Chem. B* **2006,** *110,* 23982-23986.

[11] Rairden, J. R.; Neugebauer, C. A.; Sigsbee, R. A. *Metall. Trans.* **1971,** *2,* 719-722.

[12] Moody, N. R.; Adams, D. P.; Medlin, D.; Headley, T.; Yang, N.; Volinsky, A. *Int. J. Fract.* **2003,** *119/120,* 407-419.

[13] Huang, Y.; Qiua, H.; Wang, F.; Pana, L.; Tian, Y.; Wu, P. *Vacuum* **2003,** *71,* 523-528.

[14] Huang, Y.; Qiu, H.; Pan, L.; Tian, Y.; Wang, F.; Wu, P. *Journal of University of Science and Technology Beijing* **2004,** *11,* 235-239.

[15] Brown, D. A.; Raju, J. R. *J. Chem. Soc. A* **1966,** 1617-1620.

[16] Arrais, A.; Diana, E.; Gervasio, G.; Gobetto, R.; Marabello, D.; Stanghellini, P. *Eur. J. Inorg. Chem.* **2004,** *2004,* 1505-1513.

[17] Bermudez, V. M. *J. Vac. Sci. Technol., A* **2013,** *31,* 031402/1-031402/8.

[18] Xu, H.; Aizpurua, J.; Käll, M.; Apell, P. *Phys. Rev. E: Stat. Nonlinear Soft Matter Phys.* **2000,** *62,* 4318-4324.

[19] Moskovits, M. *Phys. Chem. Chem. Phys.* **2013,** *15,* 5301-5311.

[20] Kneipp, K.; Kneipp, H.; Itzkan, I.; Dasari, R. R.; Feld, M. S. *J. Phys. Condens. Matter* **2002,** *14,* R597-R624.

[21] Alajtal, A. I.; Edwards, H. G. M.; Elbagerma, M. A.; Scowen, I. J. *Spectrochim. Acta, Part A* **2010,** *76,* 1-5.

[22] Cialla, D.; Siebert, R.; Hübner, U.; Möller, R.; Schneidewind, H.; Mattheis, R.; Petschulat, J.; Tünnermann, A.; Pertsch, T.; Dietzek, B.; Popp, J. *Anal. Bioanal. Chem.* **2009,** *394,* 1811-1818.

[23] Du, J.; Jing, C. *J. Phys. Chem. C* **2011,** *115,* 17829-17835.

[24] Asylum Research Offline Help, 101010+2015 ed.; 2014.

[25] Bartlett, P. N.; Baumberg, J. J.; Coyle, S.; Abdelsalam, M. E. *Faraday Discuss.* **2004,** *125,* 117-132.

[26] USB2000 Fiber Optic Spectrometer Installation and Operation ManualManual, Document Number 170-00000-000-02-1005 ed.; 2006.

[27] Marchand, P.; Marmet, L. *Rev. Sci. Instrum.* **1983,** *54,* 1034-1041.

[28] Verschueren, K. *Handbook of Environmental Data on Organic Chemicals;* volume 1-2 John Wiley & Sons: New York, NY, 4th ed.; 2001.

[29] Sousa, P.; Silvestre, A.; Popovici, N.; Conde, O. *Appl. Surf. Sci.* **2005,** *247,* 423-428.

[30] Gadenne, P.; Sella, C.; Gasgnier, M.; Benhamou, A. *Thin Solid Films* **1988,** *165,* 29-48.

[31] Halas, N. J. *Opt. Photon. News* **2002,** *13,* 26–30.

[32] Vandenabeele, P. Interfrences and Side-effects. In *Practical Raman Spectroscopy: An Introduction*; John Wiley & Sons, Ltd: West Sussex, 2013.

[33] Ramart-Lucas, M.; Matti, M. J.; Guilmart, T. *Bull. Soc. Chim. Fr.* **1948,** *15,* 1215-1224.

[34] Kou, J.; Zhang, H.; Yuan, Y.; Li, Z.; Wang, Y.; Yu, T.; Zou, Z. *J. Phys. Chem. C* **2008,** *112,* 4291-4296.

[35] Shirk, M.; Molian, P. *Carbon* **2001,** *39,* 1183-1193.

[36] Oklejas, V.; Sjostrom, C.; Harris, J. M. *J. Phys. Chem. B* **2003,** *107,* 7788-7794.

Chapter 4

TDHF Study of Laser Field Directionality and Energy Effects on Raman Intensities of Oriented PAHs; With Applications to the Detection of PAHs with SERS

4.1 Introduction

SERS has attracted considerable interest for sensor applications [1]. Its sensitivity of single molecule detection [2–4] makes it more appealing for sensor application. The most important challenge that SERS faces is reproducibility [5]. When it comes to detection of small numbers of molecules or other species, reproducibility is highly affected by heterogeneity of orientation/alignment [6]. If one can control the alignment of analytes, not only between themselves and with the substrate surface, but also with

regard to monochromatic laser propagation and laser electric field direction or above all and more importantly, with the dominant local electric field, then one is that much closer to quantitative SERS [7].

A few papers have reported studies of the effect of the angle between the polarization of the exciting light and the major axis of nanoparticles to illustrate that SERS signal enhancement fluctuates periodically with this angle [8–12]. These studies with emphasis on the electromagnetic mechanism of SERS enhancement elaborate on the modification of the incident laser polarization on the surface by the local surface electric field which could override laser field direction depending on the geometry of the experiment. In special cases such as when the chemical mechanism is the main contributor to SERS enhancement, as in the study of graphene-enhanced Raman spectroscopy [6], the initial laser polarization will be maintained since it will not be modified by the non-metallic surface because of the absence of a local field on the graphene substrate. Herein it is demonstrated that for a reproducible signal for either SERS or Raman, when the purpose is to sense a trace amount in a quantitative manner, one needs to bear in mind that those few molecules must preserve their orientation and angle with the laser field direction as well. Maintaining this orientation (and consequently the orientation with respect to the surface or more specifically the local field) could be achieved with, for example, an aligned molecularly-imprinted polymer (MIP) serving as a matrix to capture/confine analytes (see section 5.2.5). Raman signals in this chapter are calculated when

1. the polarized incident laser interacts with molecules oriented with respect to that incident polarization without considering modifications by a SERS surface electric field (a model for confinement in a matrix like an MIP), or

2. the unpolarized incident light (natural light) interacts with a molecule for both static and dynamic field cases.

Changing the orientation of the molecule with respect to the laser field is geometrically equivalent to changing the orientation of the field with respect to a fixed molecule. We do the latter in our calculations, in accordance with the functional definitions of the software used [13, 14].

One could consider calculating the Raman signal of the confined molecules in the presence of a surface electric field to obtain SERS signals, but this is not performed here. The present study provides the basis for more complex calculations such as including a SERS surface, by exploring how the field can affect the Raman response from a confined phenanthrene or naphthalene molecule. The further modifications of this response by coupling with the enhanced electric field of a surface or hot spot (the local electric field coupled with the laser field) are important to consider in the future [11].

Detecting PAHs in low concentrations in produced water from the off-shore oil industry is important because of their adverse effects on marine organisms [15]. Raman activities/spectra of naphthalene and phenanthrene, two common and simple polycyclic aromatic hydrocarbons (PAHs), are calculated for the first time using the method introduced in this chapter both for an oriented molecule under different laser electric field directions and a free molecule. The calculated Raman activities/spectra for static Raman and dynamic Raman with two different laser wavelengths (536 nm and 1139 nm) are compared for a free molecule in order to investigate laser energy-dependent Raman responses. Results on these molecules and the broader findings about the importance of the molecule-laser electric field interaction geometry approach the ultimate goal of quantitative Raman/SERS sensor design, as discussed in sections 1.1 and 1.8 in Chapter 1.

4.2 Methods

Two polycyclic aromatic hydrocarbons (PAHs), naphthalene and phenanthrene, were studied in this work. All calculations were done with GAMESS-US version 1 OCT 2010 (R1) [13, 14]. Molecular visualization was done with Macmolplt [16]. The molecular structures were determined with geometry optimization using the restricted Hartree Fock method with 6-31G(d,p) and 6-31+G(d,p) basis sets, applying vibrational analysis to ensure that energy minima were obtained.

Ordinary Raman intensities were calculated with Hartree Fock, performing numerical calculations in the presence of an external static finite electric field after first determining the force constant matrices and force gradient vectors of the equilibrium structures. These Raman intensities are produced by the numerical differentiation procedure of Komornicki [17] using the default value of 0.002 a.u. for the applied static electric field strength. These calculations were performed only to obtain vibrational mode symmetry assignments.

The dynamic (non-resonant) and static Raman and depolarization ratios were obtained with the extended time-dependent (restricted) Hartree-Fock (TDHFX) method, which permits a fully analytical calculation, within the double-harmonic oscillator approximation, of the non-resonant Raman activities with explicit inclusion of the effects of the frequency (ω) of the applied laser [18–21]. Other previously available methods were only able to perform either a fully analytical calculation of Raman activities at the static level or a mixed analytic/numerical procedure at the dynamic level [19]. TDHFX produces derivatives of frequency-dependent polarizability tensor components of the ith vibrational normal mode with respect to its coordinate Q_i for calculation of the associated dynamic Raman activity [19]. This provides a computationally efficient way to conduct two studies here: first to investigate the effect of the frequency ω of the applied incident laser on non-resonant dynamic Raman activities

as presented in section 4.3.2, and second and more specifically to study the laser field directionality effect on an oriented molecule's non-resonant dynamic Raman response as presented in section 4.3.1 [19].

4.2.1 Definitions of orientation

To obtain dynamic Raman the input structures have to be designed based on the master frame rules for GAMESS-US, which is simply a standard orientation for the molecule. According to these rules, the z axis coincides with the principal rotation axis and the x axis with the perpendicular two-fold rotation axis. Hence, for either naphthalene with D_{2h} symmetry or phenanthrene with C_{2v} symmetry the principal rotation axis has to be aligned along the z axis. The xy and xz planes are σ_h and σ_v planes, respectively, if these exist for the molecular symmetry. Therefore, the molecular planes for naphthalene and phenanthrene coincide with xy and xz planes, respectively. See Figures 4.1 and 4.2 for the structures and graphical depictions of the definitions of the axes. In order to further confirm that structures were correctly designed according to master frame rules, the COORD=PRINAXIS option was included which uses Cartesian coordinates, as input and transforms them to principal axes.

A Raman calculation within the TDHFX method provides choices of a plane-polarized incident laser in the x, y or z direction adoptable for oriented molecules (confined in space), and an unpolarized ("natural") incident light adoptable for free molecules. For oriented molecules the illumination and detection geometry are illustrated in Figure 4.3 for which the direction of propagation of the incident laser coincides with the y axis [21]. See Appendix D, section D.2 and Figure D.1 to be familiarized with key script terms defining these conditions in the input file.

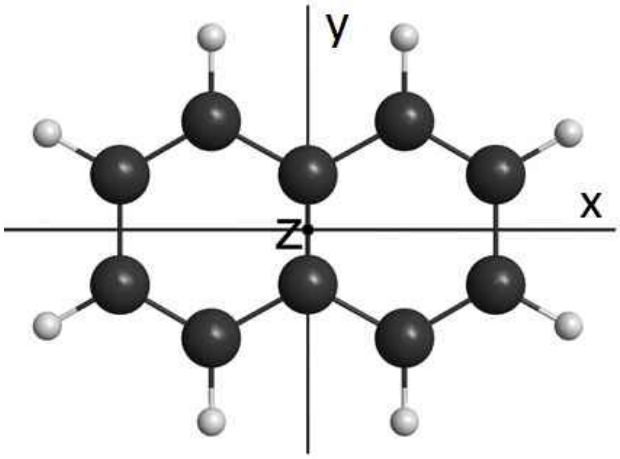

Figure 4.1: Naphthalene orientation with regard to the Cartesian coordinates. This is an orientation based on the master frame rules for GAMESS-US for a molecule with D_{2h} symmetry.

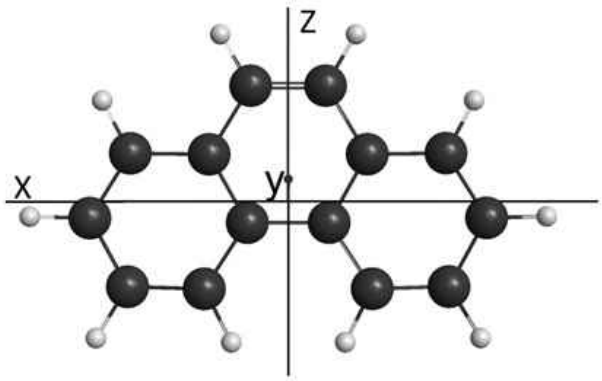

Figure 4.2: Phenanthrene orientation with regard to the Cartesian coordinates. This is an orientation based on the master frame rules for GAMESS-US for a molecule with C_{2v} symmetry.

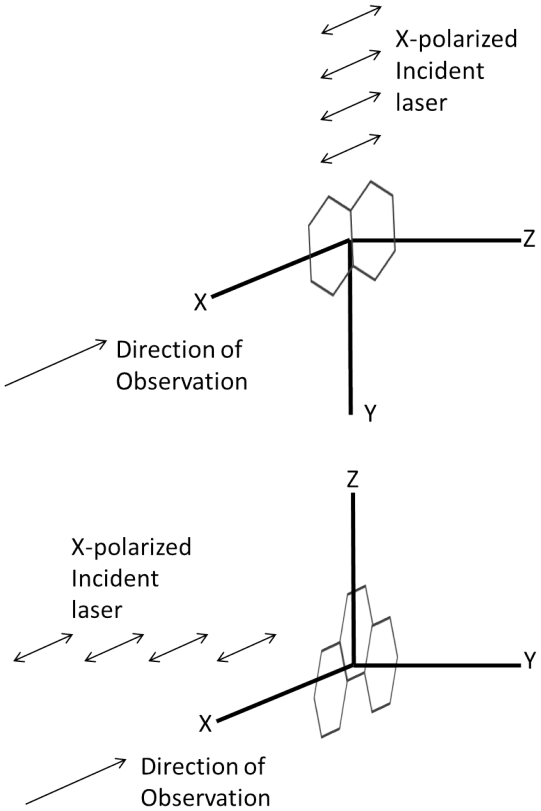

Figure 4.3: Molecule-laser field interaction geometry with an x-polarized laser for (a) oriented naphthalene and (b) oriented phenanthrene. The incident laser could be also y or z polarized. Note the different orientations which are required to match the master frame rules for GAMESS-US for molecules of different symmetry.

4.2.2 Raman activities and intensities

The Raman responses presented here are scattering activity coefficients as directly obtained from the program output. Although labeled as Raman intensities, these are actually activities. But obviously a bigger Raman activity denotes a stronger Raman intensity for a particular mode, which addresses the purpose here, namely investigating the inherent molecular response to a varying laser field direction and energy. If one wants to reproduce the shape of the whole Raman spectrum for a large molecular population of a specific compound, the direct output of the TDHFX calculation should be fed to Equation 4.1. This equation shows how the scattering activity coefficient of mode i is related to its Raman intensity [19].

$$I_i\left(\omega \pm \omega\right) = NI_0\left(\frac{1}{1440\epsilon_0^2\pi^2c^4}\right)\frac{\left(\omega \pm \omega_i\right)^4}{\left(1-e^{-(h\omega_i)/kT}\right)^{-1}}I_i\left(\omega\right) \tag{4.1}$$

where $I_i\left(\omega \pm \omega\right)$ is the frequency-dependent Raman intensity for mode i, N is the number of molecules, I_0 is the irradiance, ω_i is the angular frequency of the vibrational normal mode, ϵ_0 is the permitivity of vacuum, c is the speed of light, h is Planck's constant, k is the Boltzmann constant, T is the temperature, and $I_i(\omega)$ is the scattering coefficient (Raman activity) of mode i which is defined in Equation 4.3. The - and + signs refer to the Stokes and anti-Stokes bands respectively. To get anti-Stokes intensities, Equation 4.1 should be multiplied by a factor of $e^{-(h\omega_i)/kT}$ to account for the smaller vibrational excited state population [19].

Each value of I_i or $I_i(\omega)$ for mode i produced by the software is an intensity activity coefficient or scattering activity coefficient, expressed in units of $\text{Å}^4\text{amu}^{-1}$ which for ordinary Raman is calculated by Equation 4.2 [17]:

$$I_i = \alpha'^2 + \left(\frac{13}{45}\right)\gamma'^2 \tag{4.2}$$

where α' and γ' are the derivatives of the trace and anisotropy of the Raman tensor, respectively, of the polarizability tensor.

For dynamic Raman (produced by the TDHFX method) the activity values are obtained within the double harmonic approximation: force constants are harmonic and only linear terms in the series expansion of the polarizability tensor components are utilized with respect to a normal mode [19, 21, 22]. They are calculated from Equation 4.3:

$$I(\omega)_i = 45\left(\alpha_i'(\omega)\right)^2 + 7\left(\gamma_i'(\omega)\right)^2 \tag{4.3}$$

in which $I(\omega)_i$ is the frequency (ω) dependent scattering coefficient of mode i, and $\alpha_i'(\omega)$ and $\gamma_i'(\omega)$ are the frequency-dependent derivatives of the trace and anisotropy of the Raman tensor, respectively. Equation 4.3 assumes that the incident light is plane polarized, the observation (detection) is made in a direction perpendicular to both the electric field and its propagation direction [18, 19], and the scattered light is collected without an analyzer [23] (see Figures 4.3 and D.1 in Appendix D). This equation states that the calculated activity value for each mode is the sum of the two components polarized parallel and perpendicular to the direction of the polarization of the incident laser (laser electric field direction) whose activities could be obtained from Equations 4.4 and 4.5 respectively [18, 19]:

$$I_{\parallel}(\omega)_i = 45\left(\alpha_i'(\omega)\right)^2 + 4\left(\gamma_i'(\omega)\right)^2 \tag{4.4}$$

$$I_{\perp}(\omega)_i = 3\left(\gamma_i'(\omega)\right)^2 \tag{4.5}$$

When the incident beam is linearly polarized, the laser depolarization ratio for dynamic Raman is calculated with the same interaction geometry defined for $I(\omega)_i$

using Equation 4.6 [18, 21]:

$$\rho_i(\omega) = \frac{3\left(\gamma_i'(\omega)\right)^2}{45\left(\alpha_i'(\omega)\right)^2 + 4\left(\gamma_i'(\omega)\right)^2} \tag{4.6}$$

Tables D.1, D.2, D.3 and D.4 provide α' and γ' values for naphthalene and phenanthrene from which Raman activity coefficients and depolarization ratios (not presented here) are calculated using Equations 4.3, and 4.6 for polarized lasers, keeping in mind some necessary unit conversions for activity coefficients.

4.3 Results

Dynamic Raman responses are calculated for two laser energies $\omega = 0.085$ hartree = 2.31 eV (a green laser with wavelength of 536 nm) and $\omega = 0.04$ hartree = 1.09 eV (an IR laser with wavelength of 1139 nm) for free naphthalene and phenanthrene. Raman responses are also calculated for oriented naphthalene and phenanthrene under various electric field directions of the IR laser. Simulated Raman spectra of naphthalene and phenanthrene for laser field polarizations along x, y and z directions and for a non-polarized incident light (free molecule) are graphed in Figures 4.4 and 4.5 respectively. Those modes that show significant changes for calculated Raman activities under those conditions are summarized in Tables 4.1 and 4.2. Simulated Raman spectra for different laser energies $\omega = 0.04$ hartree (1.09 eV) and $\omega = 0.085$ hartree (2.31 eV) and with a static field for naphthalene and phenanthrene are presented in Figures 4.6 and 4.7 respectively. Modes which show significant changes for calculated Raman activities for varying laser energies and static field are presented in Tables 4.3 and 4.4.

Table 4.5 collects theoretical and experimental vibrational frequencies, calculated dynamic Raman activities and experimental Raman signal strengths for low and high

energy lasers along with tentative assignments of corresponding vibrational types (when available from [24]) followed by symmetries assigned by the ordinary Raman calculation for phenanthrene. There is ambiguity in some peak assignments in the 1200–1500 cm^{-1} region, which is also seen in comparing other experimental and computational data in the literature [25, 26]. There are disagreements in the literature about some peak assignments. The mode at 1245 cm^{-1} is assigned to a_1 by Bree *et al.* but to b_1 by Huang *et al.* The mode at 1316 cm^{-1} is not observed by either although Bree *et al.* observes a nearby peak at 1321 cm^{-1}, assigning it a_1 symmetry. The mode at 1418 cm^{-1} is assigned to a_1 by Huang *et al.* Modes at 409 cm^{-1} and 498 cm^{-1} are assigned to a_1 and b_1 by Bree *et al.* as they are in the table, but Huang *et al.* associate them with b_2 symmetry. Symmetry assignment for the peak at 828 cm^{-1} is the same as Bree *et al.* Figures 4.8 and 4.9 show visualized examples of vibration normal modes selected from Table 4.1. Additional tabulated values are presented in Appendix D.

4.3.1 Altered laser field (polarization) directions

The significant changes in Raman intensity of oriented naphthalene modes for altered laser field directions (plane polarized lasers being polarized along x, y or z directions) happen at 1782, 1620, 1487 and 831 cm^{-1}. To obtain the most intense Raman signal for each of these peaks one should use y, x, x and y polarization directions respectively (see Table 4.1 and Figure 4.4). For the mode at 1620 cm^{-1}, the laser polarized along x gives the largest relative activity and the highest activity coefficient.

A more detailed investigation into the observed differences reveals that for naphthalene the most intense peak in the spectrum is either 3371 cm^{-1} or 3345 cm^{-1} with laser field direction alteration. The mode at 3371 cm^{-1} is the most intense Raman peak when the laser field directions are x or z or with an unpolarized incident light

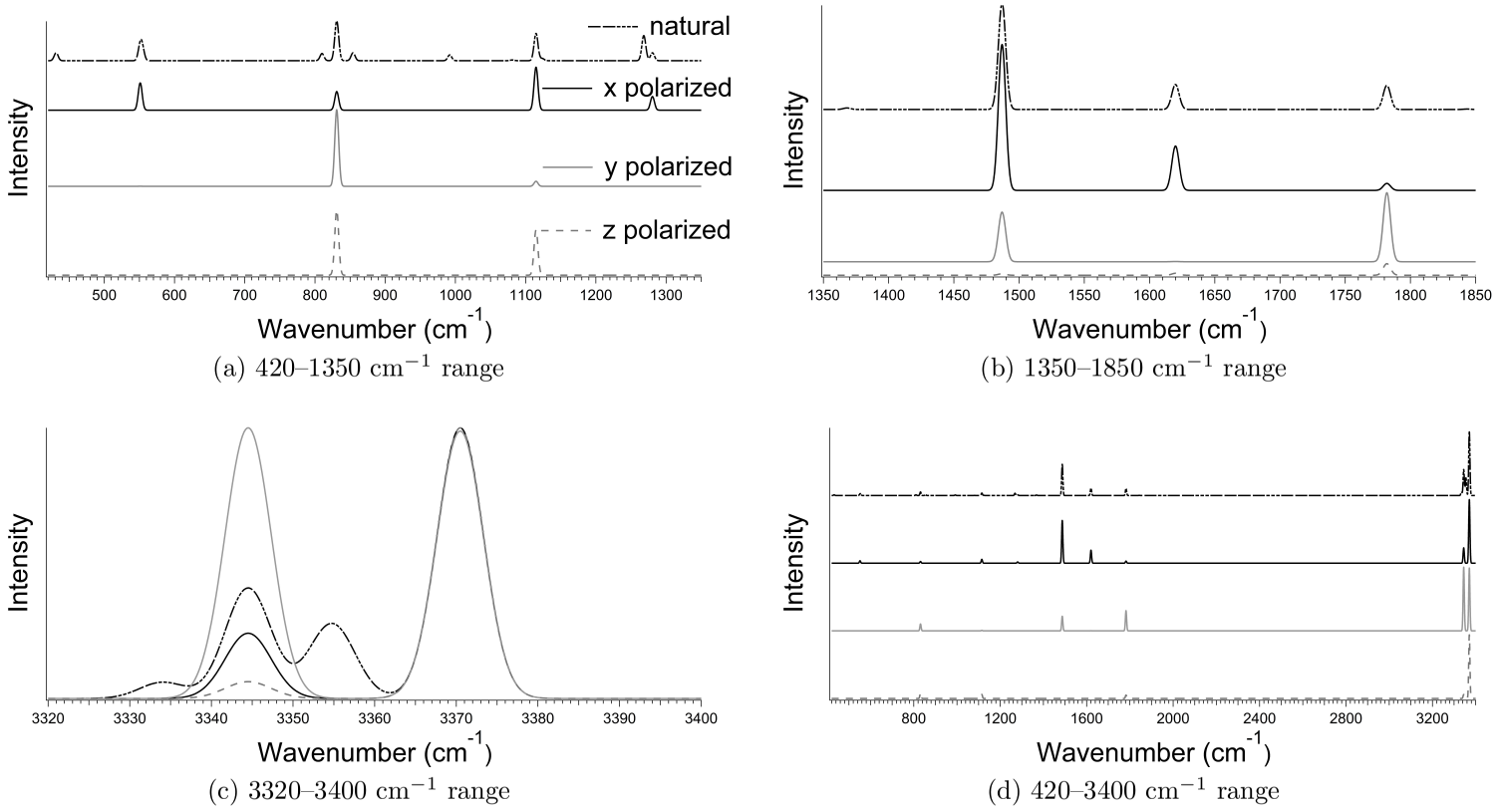

(a) 420–1350 cm^{-1} range

(b) 1350–1850 cm^{-1} range

(c) 3320–3400 cm^{-1} range

(d) 420–3400 cm^{-1} range

Figure 4.4: Raman intensities for naphthalene for varying laser field direction and unpolarized incident light when $\omega = 0.04$ hartree (1.09 eV). Each relative intensity (in percentage) is associated to a Gaussian fit (FWHM = 4 cm^{-1}), the area under which is equal to that percentage value.

Table 4.1: Intensities of naphthalene modes that show significant changes under different laser conditions (polarized and unpolarized), calculated with the 6-31G(d,p) basis set and $\omega = 0.04$ hartree (IR). The values in parentheses are percentages with regard to the most intense mode.

frequency (cm^{-1})	x-polarized	y-polarized	z-polarized	unpolarized
831	7.83 (2.60)	19.0 (10.7)	0.100 (9.10)	30.5 (5.60)
1487	205 (67.1)	40.6 (22.8)	0.0100 (0.70)	268 (49.0)
1620	62.3 (20.4)	0.190 (0.100)	0.0100 (0.900)	61.8 (11.3)
1782	9.81 (3.20)	56.4 (31.7)	0.0600 (5.30)	60.7 (11.1)
3345	73.5 (24.1)	178 (100)	0.0700 (6.20)	223 (40.8)
3371	305 (100)	176 (98.8)	1.10 (100)	547 (100)

(see Table 4.1). The 3345 cm^{-1} peak has almost the same intensity (100%) as the 3371 cm^{-1} peak (99%) when the laser field direction of y is used, while with unpolarized incident light its intensity drops to 41% of its most intense state and to 24% and 6% respectively when x and z are used (see Table 4.1 and Figure 4.4). This is very useful either for sensor design or resolving the molecular alignments in a film of naphthalene molecules as a monolayer (such as from a Langmuir film with subsequent deposition) or confined in a matrix of an (aligned) MIP thin film.

For phenanthrene, the 1705, 1462, 1405, and 1365 cm^{-1} modes appear to have higher activities under the x-polarized laser field in comparison to other plane polarized lasers, with the two modes at 1839 and 775 cm^{-1} highest with the z-polarized laser field (see Table 4.2 and Figure 4.5). All these altered peak intensities have a_g symmetry in naphthalene and are of a symmetry in phenanthrene. (For symmetry assignments see Tables D.5 and D.6 in Appendix D.) Those that do not show intensity change for altered laser fields are all related to rotationally anti-symmetric vibration modes such as b_{1g}.

When a polarized laser is used some modes show zero intensity, while they have non-zero activities in the case of the unpolarized incident light. In the case of naphtha-

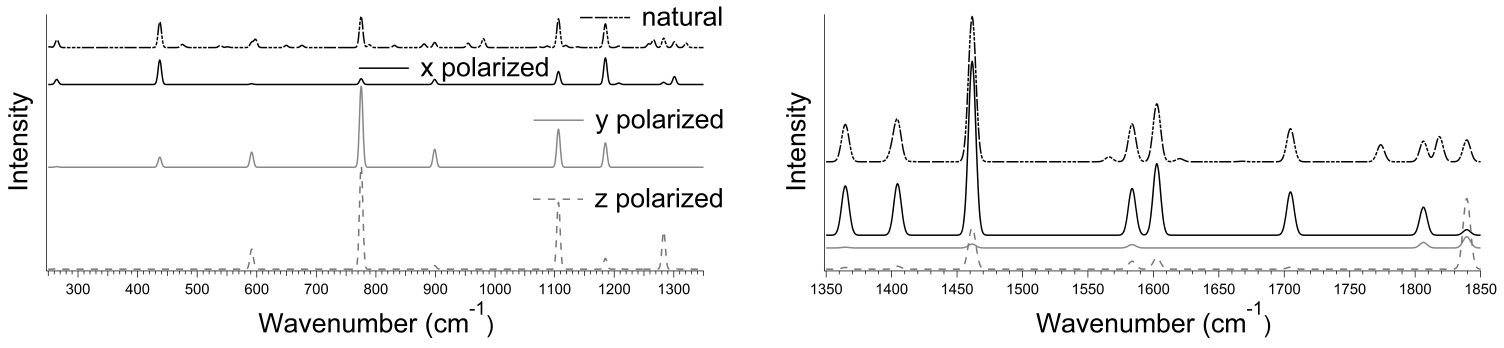

(a) 250–1350 cm^{-1} range

(b) 1350–1850 cm^{-1} range

(c) 3320–3450 cm^{-1} range

(d) 250–3450 cm^{-1} range

Figure 4.5: Raman intensities for phenanthrene for varying laser field direction and unpolarized incident light when $\omega = 0.04$ hartree (1.09 eV). Each relative intensity (in percentage) is associated to a Gaussian fit (FWHM = 4 cm^{-1}), the area under which is equal to that percentage value.

Table 4.2: Raman activities of phenanthrene modes that show significant changes under different laser conditions (polarized and unpolarized), calculated with the 6-31G(d,p) basis set and $\omega = 0.04$ (IR). The values in parentheses are percentages with regard to the most intense mode.

frequency (cm^{-1})	x-polarized	y-polarized	z-polarized	unpolarized
775	3.19 (0.800)	0.100 (11.3)	18.0 (14.4)	23.7 (4.20)
1365	85.7 (20.6)	0.00240 (0.300)	0.930 (0.700)	89.0 (15.6)
1405	89.5 (21.5)	0 (0)	1.55 (1.20)	94.0 (16.5)
1462	302 (72.6)	0.0100 (1.60)	21.7 (17.3)	345 (60.6)
1705	75.4 (18.1)	0 (0)	0.990 (0.800)	79.0 (13.8)
1839	9.69 (2.30)	0.0400 (4.70)	37.0 (29.5)	51.9 (9.10)

lene, when using an incident laser polarized along the z axis the calculated intensities are negligible (Table 4.1). This is the case for the y-polarized laser for phenanthrene (Table 4.2). These field directions are both perpendicular to the molecular planes (σ_h for naphthalene and σ_v for phenanthrene, see Figures 4.1 and 4.2). A summary of all intensities for polarized lasers and unpolarized incident light is found in Tables D.5 and D.6.

4.3.2 Altered laser energies

In altering laser energies, some but not all vibration modes for naphthalene demonstrate a signal increase for higher laser energy, as seen in Figure 4.6 and Table 4.3. The peaks at 1487, 1620, 1782 and 3371 cm^{-1} show the most significant increase, while those at 831, 1115 and 1268 cm^{-1} show a small increase. For phenanthrene, more vibrational modes show increased intensity when using a higher energy laser (1365, 1405, 1462, 1584, 1603, 1705, 3349, and 3368 cm^{-1}), with other modes showing small increases (1774, 1806, 1819, 1839, 1185, 1106, 775, 437 cm^{-1}), as seen in Figure 4.7 and Table 4.4.

Table 4.3: Effect of the laser energy on Raman activities for naphthalene. The values in parentheses are Raman activity coefficients as a percentage of the most intense mode.

frequency (cm^{-1})	activity (cm^{-1})		
	static	$\omega = 0.04$	$\omega = 0.085$
831	29.1 (5.40)	30.5 (5.60)	36.9 (6.30)
1115	19.8 (3.70)	21.0 (3.80)	26.4 (4.50)
1268	18.0 (3.30)	19.1 (3.50)	25.4 (4.40)
1487	241 (44.7)	268 (49.0)	407 (70.0)
1620	57.7 (10.7)	61.8 (11.3)	80.4 (13.8)
1782	54.0 (10.0)	60.7 (11.1)	98.2 (16.9)
3345	218 (40.4)	223 (40.8)	245 (42.2)
3355	146 (27.1)	152 (27.7)	175 (30.2)
3371	538 (100)	547 (100)	581 (100)

Table 4.4: Effect of the laser energy on Raman activities of phenanthrene. The values in parentheses are Raman activity coefficients as a percentage of the most intense mode.

frequency (cm^{-1})	activity (cm^{-1})		
	static	$\omega = 0.04$	$\omega = 0.085$
1185	17.2 (3.10)	19.0 (3.30)	27.0 (4.30)
1365	79.5 (14.3)	89.0 (15.6)	139 (22.5)
1405	81.4 (14.7)	94.0 (16.5)	164 (26.5)
1462	306 (55.2)	345 (60.6)	539 (86.9)
1584	76.6 (13.8)	89.6 (15.8)	163 (26.3)
1603	121 (21.9)	137 (24.2)	219 (35.3)
1705	70.5 (12.7)	78.6 (13.8)	120 (19.3)
1774	36.8 (6.60)	40.1 (7.10)	57.1 (9.20)
1806	44.8 (8.10)	48.6 (8.60)	65.1 (10.5)
1819	54.7 (9.90)	59.5 (10.5)	83.0 (13.4)
1839	44.9 (8.10)	51.9 (9.10)	105 (17.0)
3349	246 (44.4)	254 (44.8)	287 (46.3)
3368	555 (100)	569 (100)	620 (100)

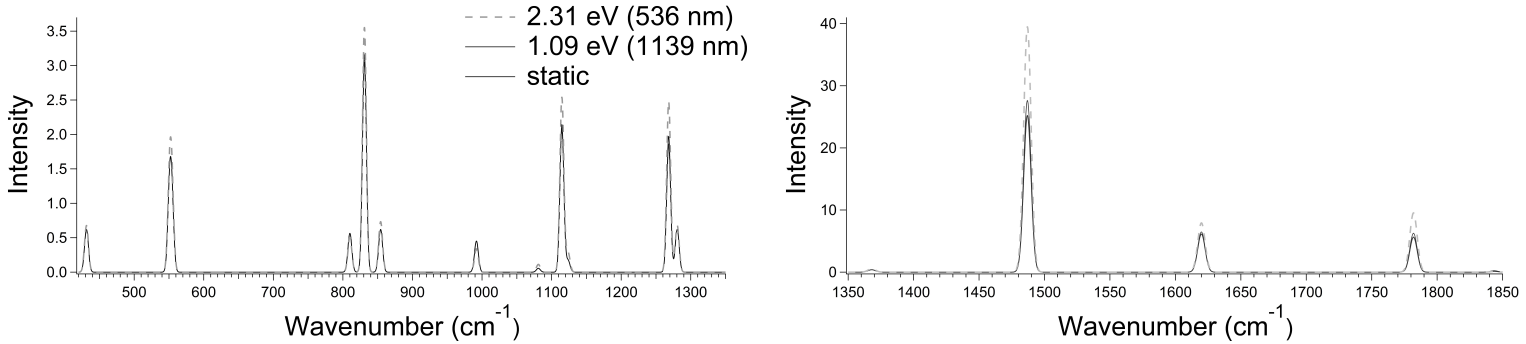

(a) 420–1350 cm^{-1} range

(b) 1350–1850 cm^{-1} range

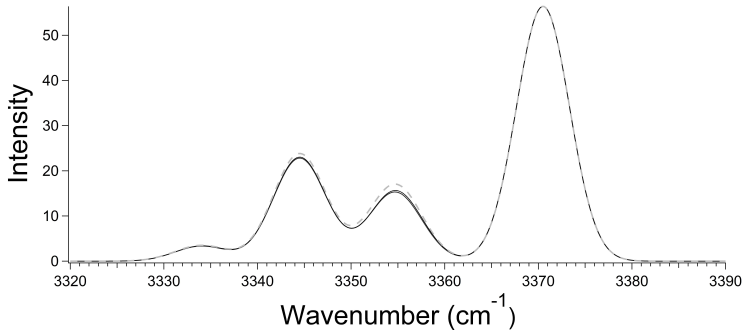

(c) 3320–3400 cm^{-1} range

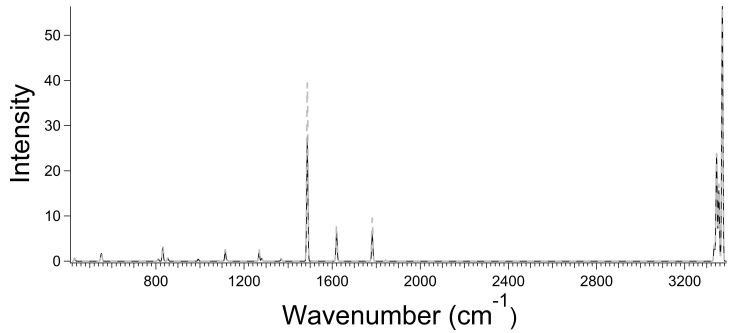

(d) 420–3400 cm^{-1} range

Figure 4.6: Raman intensities for naphthalene for laser field energies $\omega = 0.04$ hartree (1.09 eV) and $\omega = 0.085$ hartree (2.31 eV) and for a static field. Each relative intensity (in percentage) is associated to a Gaussian fit (FWHM = 4 cm^{-1}), the area under which is equal to that percentage value.

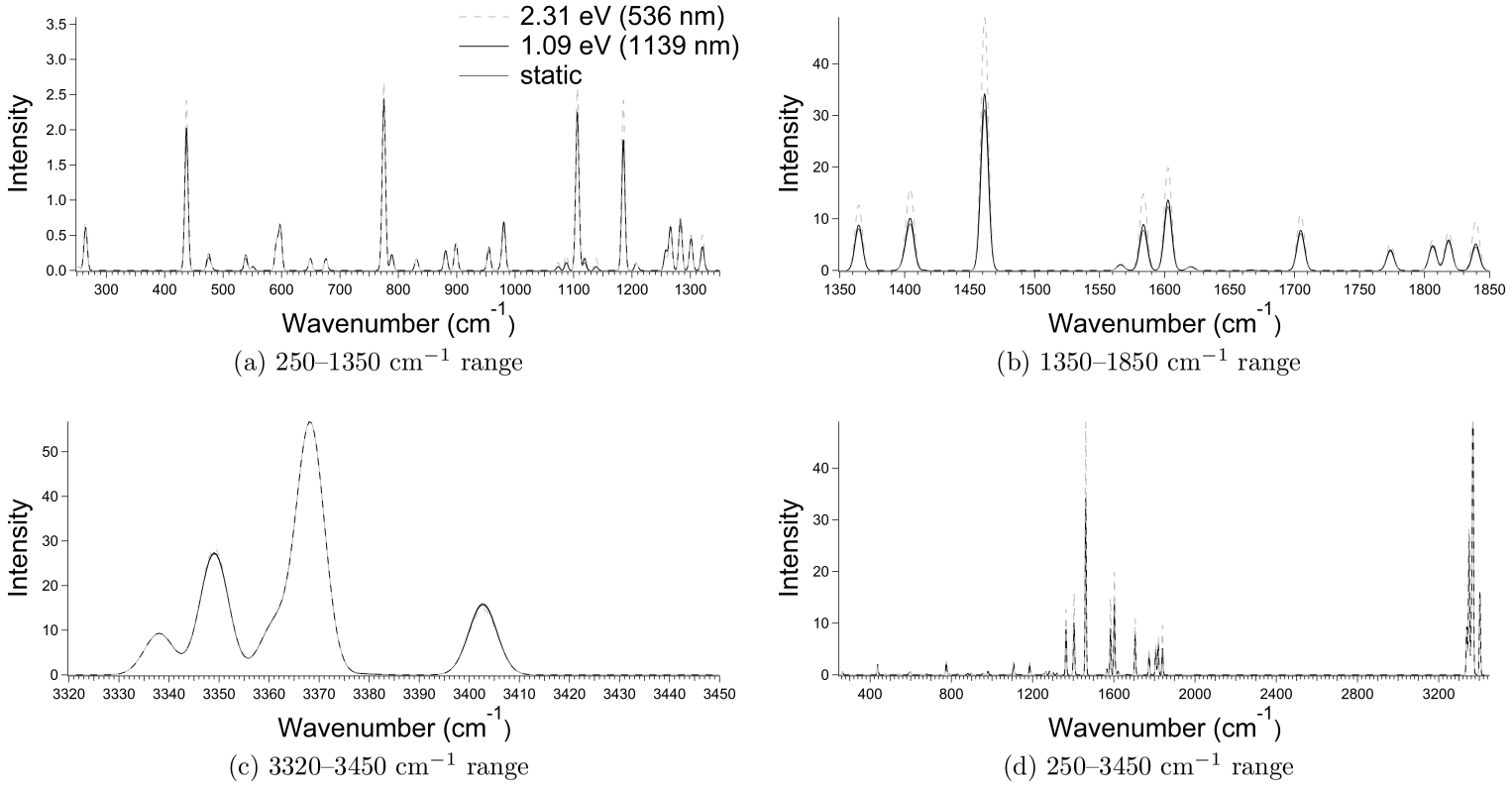

(a) 250–1350 cm^{-1} range

(b) 1350–1850 cm^{-1} range

(c) 3320–3450 cm^{-1} range

(d) 250–3450 cm^{-1} range

Figure 4.7: Raman intensities for phenanthrene for laser field energies $\omega = 0.04$ hartree (1.09 eV) and $\omega = 0.085$ hartree (2.31 eV) and for a static field. Each relative intensity (in percentage) is associated to a Gaussian fit (FWHM = 4 cm^{-1}), the area under which is equal to that percentage value.

4.4 Discussion

4.4.1 Effect of altered laser field (polarization) directions

The laser field affects two similar molecules differently, which is useful with selective sensing. This is because α' and γ' values under different laser fields acquire different values which results in different Raman activity coefficients. When the applied laser field is plane polarized normal to the molecular plane, the intensities acquire values less than 1.0 because the electric field direction is not along the polarizability tensor. This effect is significant in PAHs, which all have electron dense regions confined in the molecular plane [27]. This results in a low scattering intensity; hence this field direction does not provide an appropriate Raman signal for direct sensing purposes. However, this spectrum combined with other Raman spectra acquired in other directions confirms the alignment of confined molecules in a specific plane normal to the field direction. The combination of data with different polarization directions can also help to distinguish otherwise similar molecules. However, this does not apply when we are dealing with a molecule adsorbed in a hot spot because the local field is dominating the type of polarization felt by the analyte and re-emitted as a SERS signal [11]. The applicability of this is valid for the controlled condition where e.g., the chemical mechanism is the only contributor to the SERS enhancement in the work by Ling *et al.* where they study the effect of molecular orientation on the intensity of chemical enhancement of a planar probe aligned parallel and perpendicular with the surface of graphene [6], or e.g., when confined molecules within the matrix of MIP film will be studied with Raman.

A close look at the Raman activity tables (Tables D.5 and D.6 in Appendix D) reveals that the high symmetry vibrational modes (a_{1g} for naphthalene and a_1 for phenanthrene) show Raman activity for all types of incident lasers whilst lower sym-

metry modes are active only under an unpolarized incident light. The modes that show higher Raman activity with specific polarizations than with the unpolarized incident light must have considerable polarizability tensor components in the same direction of the applied laser. Raman tensors of confined molecules under different laser electric field directions are presented in Tables D.7 and D.8 in Appendix D for selected modes of both molecules, such as the vibration mode for naphthalene at 1487 cm^{-1} which is visualized in Figure 4.8. For this combination of displacements the polarizability tensor has a major component (α_{xx}) in the direction of the x axis. Therefore when an x polarized laser is used for the molecule which is oriented in the xy plane the largest Raman response could be obtained. For the vibration mode at 1782 cm^{-1} in Figure 4.9 the largest Raman response occurs under a y polarized laser in which case the polarizability tensor has the largest component (α_{yy}) in the same direction. Indeed it is not trivial by simply looking at a visualized vibration to predict which tensor component will have the major contribution to the polarizability tensor. These examples suggest that for reproducible Raman signals one must have a similar interaction geometry from measurement to measurement unless the analyte of study is of tetrahedral, octahedral or icosahedral symmetry groups in which case the Raman response will be independent of orientation. Furthermore, one can consider a fixed angle between the laser field and the molecular plane to reproduce the specific desired signal.

A CC stretching/HC bending mode occurs at a similar position ($\sim$1168 cm^{-1}) for both naphthalene and phenanthrene.* Only an x-polarized incident laser gives rise to a Raman signal for this mode in naphthalene (5.93, 1.90%) but in phenanthrene both z- and x- polarized incident lasers result in Raman signals (6.64, 5.30% and 1.33,

*1167 cm^{-1} [28], 1169 cm^{-1} [29] with a_g symmetry for naphthalene and 1170 cm^{-1} [28], 1169 cm^{-1} [24] with a_1 symmetry for phenanthrene. The associated calculated frequencies are 1281 cm^{-1}(naphthalene) and 1283 cm^{-1}(phenanthrene).

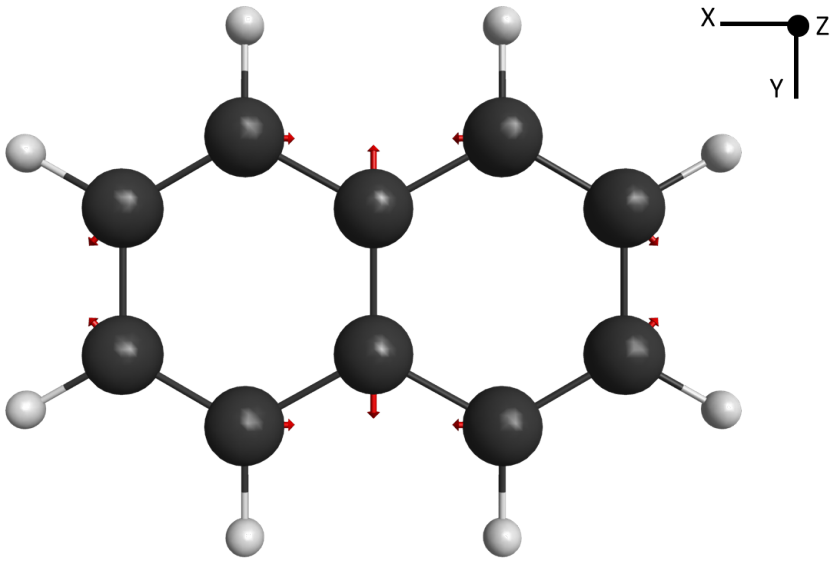

Figure 4.8: Depicted vibration mode at 1487 cm^{-1} for naphthalene. This vibration mode shows higher Raman activity under x-polarized laser. Refer to Table 4.1 for the Raman activity values calculated under different electric field directions.

0.300% respectively). Altogether, these results provide valuable information on how the spectrum changes with changing molecular orientation. This helps with sensor design, as for example if one uses an aligned MIP film (see Section 5.2.4) as a confining matrix for the analyte of interest.

4.4.2 Effect of altered laser energies

With altering laser energy there are specific modes that show a significant increase in Raman activity because of the frequency-dependence of both α' and γ' which are shown as $\alpha'(\omega)$ and $\gamma'(\omega)$ in Equation 4.3.

In fact, in the double harmonic oscillator approximation the non-resonant Raman intensity of the vibrational normal mode Q is proportional to the derivatives of the frequency-dependent polarizability $\alpha\left(-\omega;\omega\right)$ with respect to atomic Cartesian

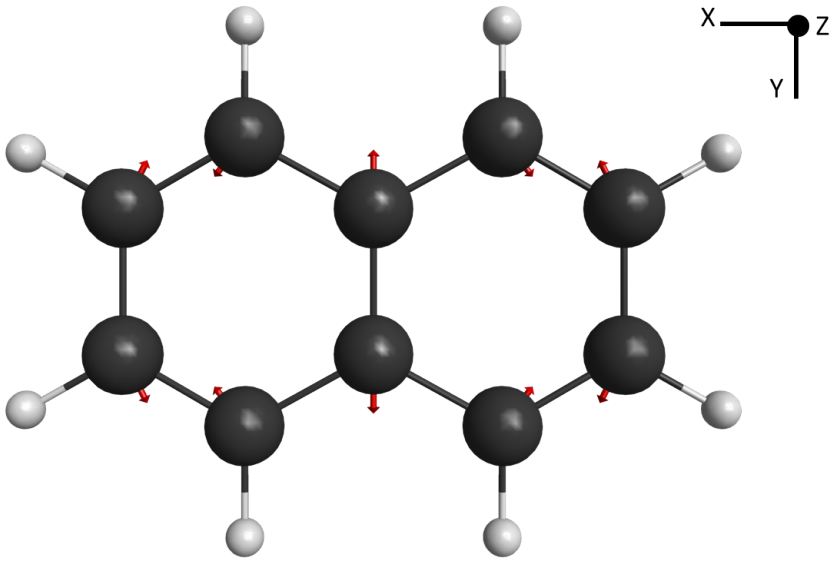

Figure 4.9: Depicted vibration mode at 1782 cm^{-1} for naphthalene. This vibration mode shows higher Raman activity under y-polarized laser. Refer to Table 4.1 for the Raman activity values calculated under different electric field directions.

coordinates as seen in Equation 4.7:

$$I(\omega) \propto \left(\frac{\partial \alpha(-\omega;\omega)}{\partial Q} \right)^2 \tag{4.7}$$

Frequency ω is the frequency at which the dynamic electric field of the incident laser resonates. Hence a change in laser energy alters the relative Raman intensities. In this way, with an appropriate laser choice particular vibrational normal modes can be emphasized, helping with determination of complex molecular structures [18]. Quinet and Champagne have shown such potential for small molecules of NH_3, H_2O and CH_4 [18]. This increase in signal with higher energy lasers is observed for mostly higher symmetry vibrational modes like a_{1g} and b_{1g} for naphthalene and a_1 and b_1 for phenanthrene. A signal increase in experimental non-resonance Raman for phenanthrene was observed in the work by Alajtal *et al.* for some modes when the laser energy was altered from low energy (1064 nm) to high (532 nm) (see Table 4.5) [24].

The thirteen vibration modes which showed increased Raman activity for the high energy laser presented in Table 4.4 are compared with the thirteen experimental peaks which showed changes in the observed Raman intensity in Table 4.5. There is a 70% match with experimental data for that group of thirteen calculated modes which showed signal change. Those are modes at 1185, 1405, 1462, 1584, 1603, 1806, 1819, 1839 and 3368 cm^{-1} among which 54% correspond to observed modes which showed increased peak strength. The observed mode at 3035 cm^{-1} associated with a calculated frequency of 3349 cm^{-1} which also showed a signal increase does not appear in the experimental Raman spectrum with a 514 nm laser. For the remaining three calculated modes (1365, 1705, 1774 cm^{-1}), experimental data do not show a change in signal strength.

Table 4.5: Comparison of calculated Raman activities and experimental Raman intensities for phenanthrene. Experimental Raman results show an increase in signal strength when the laser wavelength was altered from 1064 nm to 532 nm. For comparison purposes the calculated Raman activities for 1139 and 536 nm wavelengths are provided. Calculated Raman frequencies are scaled by a factor of 0.905 [19, 30]. Symmetry assignments are provided by ordinary Raman calculation by GAMESS-US. Vibrational assignments are mostly the ones proposed by Alajtal *et al.* (in bold), while some are done by mode visualization with Macmolplt to help with associating experimental Raman shifts more accurately to the calculated frequencies. The notations represent the strength of the observed Raman intensities (v st, very strong; st, strong; m, medium; w, weak; v w, very weak; sh, shoulder; w sh, weak shoulder; m sh, medium shoulder; st sh, strong shoulder). stch stands for stretching.

Freq. (cm^{-1})			Raman responses				Assigned vib.	Sym.
Calc.	Scaled	Obs.	Calc.		Obs.			
		$\lambda =$	1139 nm	536 nm	1064 nm	514 nm		
104	93.7		0.910	0.980				a_2
110	99.1		0.330	0.350				b_2
252	228		0.790	0.890				b_2
264	239	250	2.76	3.58	m	m		a_1

Table 4.5 (cont.)

Freq. (cm^{-1})			Raman responses				Assigned vib.	Sym.
Calc.	Scaled	Obs.	Calc.		Obs.			
		$\lambda =$	1139 nm	536 nm	1064 nm	514 nm		
265	240		3.61	3.89				a_2
437	396	409	14.5	19.7	st	st	**CCC bend**	a_1
437	396		5.47	6.65				a_2
475	430	442	2.00	2.24	w	w		b_1
480	434		0.620	0.720				b_2
539	488	498	1.94	1.85	vw	w		b_1
551	499		0.630	0.560				b_2
591	535		4.12	4.39			CCC bend, ring deformation-in plane	a_1
598	541	546	6.44	7.70	m	st	**CCC bend**, ring deformation-out of plane	a_2
650	588		1.64	1.90				a_2
676	612		1.54	1.56				b_1
773	699		0.89	1.03				b_1
775	702	710	23.7	28.6	st	v st		a_1
789	714		2.11	2.04				b_2
831	752		1.65	1.63				b_2
849	768		0.140	0.0300				a_2
881	797		2.57	2.76				a_2
899	813	828	4.07	4.20	m	m	CCC bend	a_1

Table 4.5 (cont.)

Freq. (cm^{-1})			Raman responses				Assigned vib.	Sym.
Calc.	Scaled	Obs.	Calc.		Obs.			
		$\lambda =$	1139 nm	536 nm	1064 nm	514 nm		
							ring deformation-in plane	
917	830		0.130	0.190				b_2
955	864		3.14	3.97				b_1
976	883		0.620	0.420				a_2
981	887		6.63	6.50				b_2
1074	972		0.600	1.12				a_2
1085	982		0.100	0.0700				b_2
1088	984		1.13	2.40			ring deform	b_1
1106	1001		1.33	2.11			HCC bend	a_2
1106	1001	1036	21.8	26.9	st	st	**C-C stch, HCC bend**	a_1
1118	1012		0.0400	0.0700			HCC bend	b_2
1119	1012		1.45	2.45			HCC bend	a_2
1139	1030		0.780	1.58				b_1
1185	1073	1162	18.9	27.0	w	m		a_1
1208	1093		1.13	1.55				a_1
1258	1138		2.66	1.70			HCC bend	b_1
1266	1146		6.30	6.22			HCC bend	b_1
1283	1161	1169	7.22	8.75	m	m	HCC bend	a_1
1301	1178	1200	4.52	5.78	m	m	**C-C stch, HCC bend**	a_1

Table 4.5 (cont.)

Freq. (cm^{-1})			Raman responses				Assigned vib.	Sym.
Calc.	Scaled	Obs.	Calc.		Obs.			
		$\lambda =$	1139 nm	536 nm	1064 nm	514 nm		
1321	1195		3.49	5.62				b_1
1365	1235		89.0	139			HCC bend	a_1
1400	1267		21.2	27.5			HCC bend	b_1
1405	1271	1245	94.0	164	st	m	**HCC bend**	a_1
1415	1280	1316	0.790	1.32	w	w		b_1
1462	1323	1350	345	539	st	v st	**C-C stch,**	a_1
							HCC bend	
1566	1417	1418	11.1	14.9	m sh	st	C-C stch,	b_1
							HCC bend	
1584	1433	1429	89.6	163	w sh	st	**C-C stch**	a_1
							HCC bend	
1603	1450	1440	137	219	st	v st	**C-C stch,**	a_1
							HCC bend	
1620	1466		7.40	9.30			C-C stch,	b_1
							HCC bend	
1668	1509		0.860	2.10			C-C stch,	b_1
							HCC bend	
1705	1543	1523	78.6	120	st	st	C-C stch,	a_1
							HCC bend	
1774	1605	1570	40.1	57.1	m	m	**C-C stch**	b_1
1806	1635	1599	48.6	65.1	w sh	w	C-C stch	a_1
1819	1646	1613	59.5	83.0	m sh	st sh	**C-C stch**	b_1

Table 4.5 (cont.)

Freq. (cm^{-1})			Raman responses				Assigned vib.	Sym.
Calc.	Scaled	Obs.	Calc.		Obs.			
		$\lambda =$	1139 nm	536 nm	1064 nm	514 nm		
1839	1665	1622	51.9	105	m	st	**C=C stch**	a_1
3336	3019		4.61	4.50				b_1
3338	3021		81.7	90.0				a_1
3340	3023		11.0	12.2				b_1
3349	3031	3035	254	287	m	not seen	C-H stch	b_1
3350	3031		21.7	24.9				a_1
3361	3042		108	120				a_1
3366	3046		0.0100	0				b_1
3368	3048	3057	569	620	m	m sh	C-H stch	a_1
3379	3058		2.47	3.78				b_1
3403	3079	3071	159	162	st	st	**C-H stch**	a_1

A pitfall might occur in the interpretation of the laser energy effect on observed and calculated Raman signals. The dependency seen here for some Raman peak heights on incident laser energy should not be confused with resonance Raman where the increase in signal intensity occurs due to tuning the incident laser energy into the molecular excited state. Neither of the applied lasers were in the energy range that matches UV-Vis absorption maximum for phenanthrene (λ_{max} = 240 nm, 5.17 eV) [31]. In fact the observed behavior is due to the inherent dependency of polarizability on the incident laser's dynamic electric field energy and it is not related to the so-called ν^4 effect presented with the $(\omega \pm \omega_i)^4$ term in Equation 4.1. Here all data (Tables

and Figures) are direct output values from the TDHFX method for Raman activity coefficients which were calculated by Equation 4.3.

4.5 Potential correlations between calculated and experimental Raman data seen for phenanthrene in Chapter 3

The CCC bending mode which appears at around 540 cm^{-1}, in the SERS study of Chapter 3 (and at 546 cm^{-1} in the study by Alajtal *et al.* [24]) has two possible assignments.

1. The 598 cm^{-1} mode (scaled to 541 cm^{-1}, calculated here) shows slightly increased activity with an increase in laser energy (see Figure 4.7 and Table D.6). This increase in calculated data here (from 6.44, 1.10% to 7.20, 1.20%) corresponds to an increase in signal strength seen by Alajtal *et al.* (from medium to strong) [24]. This mode does not show any change in activity when changing the laser field direction or using an unpolarized incident light.

2. The 591 cm^{-1} mode (scaled to 535 cm^{-1}, calculated here) shows a slightly increased absolute activity with increasing laser energy but there is no change in this peak intensity relative to the highest peak intensity (from 4.12, 0.700% to 4.39, 0.700%). The activity of this mode is modified with different orientations of the incident laser (see Figure 4.5 and Table D.6 in Appendix D). This change in intensity with orientation could explain the specific enhancement of this peak observed experimentally in the SERS of a trapped phenanthrene molecule.

The SERS peak at 846 cm^{-1} (828 cm^{-1}, Alajtal *et al.* [24]) seen for phenanthrene on Au=42 nm (Figure 3.10, Chapter 3) probably corresponds to the calculated mode

of 898 cm^{-1} (scaled to 813 cm^{-1}). The calculated Raman activities under x-, y-, and z- polarized lasers and an unpolarized incident light are 2.93 (0.700%), 0.0200 (2.50%), 0.670 (5.00%) and 4.07 (0.700%). This mode shows the largest relative Raman signal (percentage value) with the y polarized laser. Simulated activities suggest the above-mentioned observation could be in line with the interaction of a polarized laser in the direction parallel to the molecular plane of phenanthrene on the substrate.

4.6 Conclusions

Alignment clearly makes a difference in the measured Raman spectra, with heterogeneity in alignment contributing to non-reproducible Raman signals in anisotropic systems such as adsorbates on a SERS substrate. By aligning the molecules, such as by adsorbing them within an aligned MIP, one could thus reduce the variability in Raman scattering between measurements and samples.

By performing Raman calculations, the proper design could be predicted for a sensor such as proposed aligned MIP on a SERS substrate. What matters most is reproducibility rather than a particular alignment. This chapter shows how the spectrum changes with changing orientation. Molecular species (confined) show different polarizability for different laser field directions resulting in various increases in Raman response of different vibrational modes. These findings inform the design of Raman experiments and Raman/SERS-based sensors in two ways. They help to determine the appropriate molecular orientation(s) for optimum signal acquisition, and they have the added benefit of providing distinguishing features for the identification of similar molecules that respond differently to changes in polarization. The calculations on different laser energies also provide further distinguishing features.

Bibliography

[1] Halvorson, R. A.; Vikesland, P. J. *Environ. Sci. Technol.* **2010,** *44,* 7749-7755.

[2] Kneipp, K.; Kneipp, H.; Itzkan, I.; Dasari, R. R.; Feld, M. S. *Chem. Rev.* **1999,** *99,* 2957-2975.

[3] Kneipp, K.; Wang, Y.; Kneipp, H.; Perelman, L. T.; Itzkan, I.; Dasari, R.; Feld, M. S. *Phys. Rev. Lett.* **1997,** *78,* 1667-1670.

[4] Nie, S.; Emory, S. R. *Science* **1997,** *275,* 1102-1107.

[5] Cialla, D.; März, A.; Böhme, R.; Theil, F.; Weber, K.; Schmitt, M.; Popp, J. *Anal. Bioanal. Chem.* **2012,** *403,* 27-54.

[6] Ling, X.; Wu, J.; Xu, W.; Zhang, J. *Small* **2012,** *8,* 1365–1372.

[7] Etchegoin, P. G.; Le Ru, E. C. *Phys. Chem. Chem. Phys.* **2008,** *10,* 6079-6089.

[8] Tao, J.; Lu, Y. H.; Chen, J. X.; Lu, D. W.; Chen, C. C.; Wang, P.; Ming, H. *Plasmonics* **2011,** *6,* 785-789.

[9] Mohanty, P.; Yoon, I.; Kang, T.; Seo, K.; Varadwaj, K. S. K.; Choi, W.; Park, Q. H.; Ahn, J. P.; Suh, Y. D.; Ihee, H.; Kim, B. *J. Am. Chem. Soc.* **2007,** *129,* 9576-9577.

[10] McLellan, J. M.; Li, Z. Y.; Siekkinen, A. R.; Xia, Y. N. *Nano Lett.* **2007,** *7,* 1013-1017.

[11] Etchegoin, P. G.; Galloway, C.; Le Ru, E. C. *Phys. Chem. Chem. Phys.* **2006,** *8,* 2624-2628.

[12] Xu, H. X.; Käll, M. *ChemPhysChem* **2003,** *4,* 1001-1005.

[13] Schmidt, M. W.; Baldridge, K. K.; Boatz, J. A.; Elbert, S. T.; Gordon, M. S.; Jensen, J. H.; Koseki, S.; Matsunaga, N.; Nguyen, K. A.; Su, S.; Windus, T. L.; Dupuis, M.; Montgomery, J. A. *J. Comput. Chem.* **1993,** *14,* 1347-1363.

[14] Gordon, M. S.; Schmidt, M. W. Advances in electronic structure theory: GAMESS a decade later. In *Theory and Applications of Computational Chemistry: the first forty years*; Dykstra, C. E.; Frenking, G.; Kim, K. S.; Scuseria, G. E., Eds.; Elsevier: Amsterdam, 2005.

[15] Neff, J. M.; Johnsen, S.; Frost, T. K.; Utvik, T. I. R.; Durell, G. S. *Mar. Environ. Res.* **2006,** *62,* 224–246.

[16] Bode, B. M.; Gordon, M. S. *J. Mol. Graphics Modell.* **1998,** *16,* 133-138.

[17] Komornicki, A.; McIver, J. W. *J. Chem. Phys.* **1979,** *70,* 2014-2016.

[18] Quinet, O.; Champagne, B. *J. Chem. Phys.* **2001,** *115,* 6293-6299.

[19] Quinet, O.; Champagne, B. *Int. J. Quantum Chem.* **2002,** *89,* 341-348.

[20] Craig, D. P.; Thirunamachandran, T. *Molecular Quantum Electrodynamics: An Introduction to Radiation Molecule Interactions;* Academic Press Inc.: London, 1984.

[21] Wilson, E. B.; Decius, J. C.; Cross, P. C. *Molecular Vibrations: The Theory of Infrared and Raman Vibrational Spectra;* Dover, New York: 1980.

[22] Michalska, D.; Wysokinski, R. *Chem. Phys. Lett.* **2005,** *403,* 211–217.

[23] Polavarapu, P. *J. Phys. Chem.* **1990,** *94,* 8106-8112.

[24] Alajtal, A. I.; Edwards, H. G. M.; Elbagerma, M. A.; Scowen, I. J. *Spectrochim. Acta, Part A* **2010,** *76,* 1-5.

[25] Huang, Q.-W.; Zhang, J.; Berlie, A.; Qin, Z.-X.; Zhao, X.-M.; Zhang, J.-B.; Tang, L.-Y.; Liu, J.; Zhang, C.; Zhong, G.-H.; Lin, H.-Q.; Chen, X.-J. *J. Chem. Phys.* **2013,** *139,* 104302/1-104302/7.

[26] Bree, A.; Solven, F.; Vilkos, V. *J. Mol. Spectrosc.* **1972,** *44,* 298-319.

[27] Hammond, J. R.; Kowalski, K.; deJong, W. A. *J. Chem. Phys.* **2007,** *127,* 144105/1-144105/9.

[28] Maddams, W.; Royaud, I. *Spectrochim. Acta, Part A* **1990,** *46,* 309-314.

[29] Shinohara, H.; Yamakita, Y.; Ohno, K. *J. Mol. Struct.* **1998,** *442,* 221-234.

[30] Scott, A. P.; Radom, L. *J. Phys. Chem.* **1996,** *100,* 16502-16513.

[31] Asher, S. A. *Anal. Chem.* **1984,** *56,* 720-724.

Chapter 5

Conclusions

5.1 Summary

The purpose of this PhD project has been to establish the groundwork required for the fabrication of a sensor package to detect hydrocarbons in harsh environments. The findings will ultimately be adopted by the oil industry for online fast water quality monitoring for the detection of PAHs. That sensor package would be either for online or remote screening of PAHs and human impact in ocean or river water within the Atlantic region. This requires qualitative detection and further down the road the ability for quantified detection. The work presented here includes (i) fabrication of a robust metal layer, (ii) the surface enhanced Raman scattering (SERS) active metal film with an ability to engage the hydrocarbon on the surface, and (iii) in-advance calculations of Raman responses of the two renowned polycyclic hydrocarbons phenanthrene and naphthalene which help with the design of the ultimate package.

Development of an analytical tool based on SERS relies on materials fabrication methods that provide stable structures – a challenging criterion for SERS based sensors [1]. Hence this project has tried to tackle this through the development of a

mechanically stable gold film which can be used as a SERS substrate in miniaturized microfluidic lab-on-chip devices with application in harsh environments [2–4]. We looked at both possible scenarios of colloidal and flat SERS substrates considering their advantages and disadvantages. As discussed in Chapter 1, it was decided to utilize flat substrates by depositing a gold thin film on glass slides. One problem was the robustness of gold thin films on glass slides. This is addressed through the post-deposition-curing method in Chapter 2.

One important factor for SERS substrates is the roughness of the film. Roughness impacts the SERS signal in a variety of ways, e.g., by affecting (i) the density of adsorption sites for analytes [5], (ii) the extent of light scattering and (iii) surface plasmons [6]. In this regard, finding a cost-effective way to allow control over surface roughness is of value. Alteration of the polymer underlayer thickness is a potential way to affect the ultimate gold thin film roughness, as discussed in Chapter 2. In Chapter 3, a systematic approach of annealing of gold/chromium bilayers, at either 325 °C or 400 °C for 1 or 2 hours, was applied in order to alter surface roughness and also to modify optical properties of samples. Not all of the results (roughness, UV-Vis reflectance intensities and features seen in UV-Vis spectra) show systematic dependence on the annealing conditions, but annealing at 400 °C for 2 hours produced samples with the highest roughness values. Among these samples, those which were produced from a bilayer Au/Cr film with the thickest gold top layer showed the best SERS activity for phenanthrene, possibly through enhanced optical property and chemical binding of phenanthrene to diffused chromium entities within the gold islands.

The following factors can affect the SERS signal: the SERS-active metal, the laser energy, and the laser power [7]. More specifically, the SERS response depends on the relation between the energy of the incident laser and the field in resonance in the

nanogap (hot spot). Etchegoin *et al.* have shown that in visible, field enhancement falls in the 10^3–10^5 range when laser polarization is fixed at 0° with regard to the axis of the dimmer of two silver colloids [8]. If the laser energy matches a UV-Vis absorption band of an analyte/chemisorbed analyte, this would cause resonance SERS [9]. For SERS studies it is suggested to have a couple of lasers with different energies available in order to tune the best energy for the specific system which is under development [10].

Finally, the angle at which the laser field interacts with the local field (e.g. dimer axis) also impacts the SERS signal [8]. For reproducibility (required for quantification) of the SERS signal, one also needs to consider the analyte and metal (hot spot) interaction geometry. The interaction geometry of the laser with this analyte-metal system should also be controlled in order to achieve reproducible robust signals. The alignment within the analyte-metal system defines how well the molecular polarizability tensors are aligned with the local electric field, a simple scenario of which has been discussed for alignment of planar molecules with respect to the laser electric field in Chapter 4.

5.2 Future directions

5.2.1 Roughness modification of the gold/SU-8 film system

The morphology of the stable gold film on the post-deposition-cured SU-8 can be tailored by applying different thicknesses of SU-8 film. This could be achieved by two approaches. One way is to try the different suggested spin speeds for SU-8 spin casting recommended by the SU-8 provider [11]. The second way is to decrease the viscosity by either diluting with propanol or trying other SU-8 formulations which differ in their viscosities [11]. Modification of the pre-bake procedure by placing a

layer between the SU-8 coated glass and the hot plate could also be tried as another alternative to tailor the morphology. This intermediate layer affects how quickly the glass slide temperature will rise to the final set temperature of the hot plate, hence affecting the solvent evaporation rate from the SU-8 which is cast on the substrate. Evaporation rate is dependent on the diffusion coefficient of the solvent in the resist which exponentially increases with increase in temperature [12].

5.2.2 Gold/SU-8 cantilever fabrication for biosensor applications

Gold coated AFM cantilevers fabricated from SU-8 have been made with applications either as AFM surface probe [13] or as biosensor [14]. Applying the method explained in Chapter 2, cantilevers of a higher quality with improved adhesion and mechanical quality than those made by Nordström and Genolet *et al.* can be fabricated. For this purpose the SU-8 2000 series should be used which – according to the manufacturer – is specifically formulated for manufacturing durable skeletons [11]. SU-8 is chemically stable and due to its low Young's modulus ($\cong$ 4 GPa) has been used for cantilever fabrication as an AFM probe where a low stiffness cantilever was required [13]. Stiffness k of a cantilever is defined by Equation 5.1 [13]:

$$k = \frac{Ewt^3}{4l^3} \tag{5.1}$$

E is the Young's modulus, w, t, and l are width, thickness and length of the lever. In AFM the sensitivity of the optical lever sensor is inversely dependent on the cantilever length [15]. Fabrication of a short lever with a low stiffness (low spring constant (<5 N/m)) from silicon and silicon nitride (with high Young's modulus E of 190 and 385 GPa respectively) becomes an issue because the only solution would be to reduce the

thicknesses (<1 μm) which is technologically difficult to access with these materials. Instead, photoresists with low Young's modulus such as novolak and SU-8 ($E \cong 4$ GPa) have been used by Pechmann *et al.* and Genolet *et al.* [13, 16]. In such cases the back side of a cantilever has to be coated with a thin layer of gold via thermal evaporation to obtain the optical reflectivity – the requirement for detection with an optical lever sensor. The method presented in Chapter 2 could be applied in this field to obtain a high quality cantilever.

5.2.3 Aiming for further modification of islands of gold and chromium

The gold chromium corrugation can be varied further by depositing different thicknesses of chromium and gold via thermal evaporation followed by an annealing step at elevated temperatures.

Their SERS activity can be further optimized by varying the size and distribution of the features. Hence, annealing parameters like target temperature, thermal elevation ramp speed and time for annealing at target temperature could be explored to obtain the nanodimensional islands of gold and chromium expected to have the highest SERS activity.

5.2.4 Raman spectroscopy of molecularly imprinted polymers with analyte

Molecularly imprinted polymers (MIPs) are synthetic polymers which hold cavities formed by the polymerization of a matrix around a template molecule which is removed later using an appropriate solvent [17]. Cavities left in the polymer have the tendency to selectively capture the template molecules since they fit their size and

shape (see Figure 5.1). Fabrication of an MIP, which is selective to PAHs in water, requires hydrophilic type polymers, like polyurethanes, for a better wettability. To enhance the affinity of PAH molecules to the cavity, since PAHs do not possess functional groups, the use of monomers with aromatic rings is suggested in order to provide the chance for $\pi - \pi$ interactions with PAHs [18].

McStay *et al.* have incorporated bulk MIPs with Raman spectroscopy for detection of bound analytes in the MIP [19]. There are a few works reporting the implementation of MIP thin films on flat substrates for SERS purposes [20–22]. The limitations of these works are explained in section 5.2.5 and they still need to be optimized before obtaining a proper SERS signal. The application of a thin MIP film to SERS-active substrates, or even plain flat substrates, can address the reproducibility issues respectively for SERS and Raman signals, as discussed in section 1.6, by fixing the adsorbed molecule orientations with respect to surface and laser at the same time. The polymer provides randomly oriented pockets on the surface, but if one can design a method that generates a polymer with specific orientation of pockets (an aligned MIP, which would be an ideal case), that will add more reproducibility for SERS. One way to achieve this could be to spin cast a layer of MIP solution in the presence of a static field with subsequent polymerization. However, a polymer with randomly oriented pockets still could be useful to generate a reproducible Raman signal from specific points on the substrate surface because the pockets will always preserve the few randomly oriented molecules in exactly same orientation with respect to the laser and surface features at those specific points. The MIP also avoids analyte-analyte interactions, which would otherwise lead to further heterogeneity in the signal [23].

The application of MIP films to plain flat substrates (non-SERS) can also provide the opportunity for trace analysis by concentrating the desired analyte selectively on the substrate. As discussed, this provides control over the laser-analyte angle on the

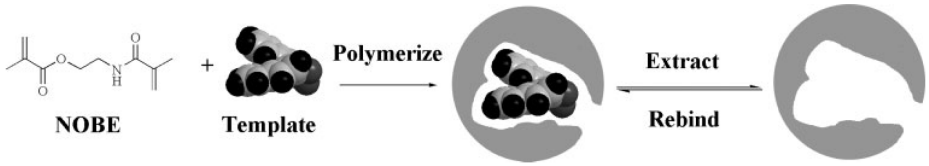

Figure 5.1: Schematic of MIP formation. N,O-bismethacryloyl ethanolamine (NOBE), which is both the cross linker and the monomer, polymerizes around the template molecule (R-(+)-1,1'-bi-2-naphthol). When the MIP is formed, the last step is to wash the template away in order to leave a binding cavity which selectively captures the template molecule (used with permission from [17]).

specific region of the substrate. Hence, by acquiring the Raman spectrum from the same spot one should expect similar signals in repeated runs. Also, this way one can obtain reproducible Raman signals without being worried about the thickness constraint for the thin MIP film which is required for the SERS signal. To obtain the SERS signal the analyte in the MIP film should be within 1000 nm of the SERS surface, which is the spatial range that the field can extend over 10–200 nm thick metallic thin film [24]. In section 5.2.5 more details are laid out on the benefits of combining MIP films with Raman and SERS.

5.2.5 Implementation of MIP films on a flat substrate with Raman microscopy and SERS

It has been stated by several pioneers in the SERS field that it is difficult to control the orientation for a single or few molecules in the hot spot [25, 26]. In this regard, MIPs are proposed here as a solution to this problem. The accessible factors to the operator in order to control the SERS effect were discussed in section 5.1. When an MIP thin film is applied to a flat substrate there will be more factors in hand to control the SERS effect. The following are the further parameters which can be accessed by a proper Raman experiment design if an MIP thin film approach is chosen:

- distance and orientation of the analyte with regard to the surface (flat substrate): This is simply done by altering the thickness of the MIP film, with the possibility of aligning the analytes in a desired orientation with regard to the surface during the MIP polymerization step.

- geometry of the laser-analyte-substrate system: In addition to varying the polarization of the laser (orientation of the electric field), one can also rotate the MIP-coated substrate to vary the laser-analyte angles.

By simply assembling the MIP on a flat substrate and acquiring the Raman spectrum with a given laser field (polarization) and angle with respect to the flat substrate a repeatable signal can be easily obtained. For this purpose one needs to first choose an MIP whose Raman spectrum does not overlap with the characteristic Raman peaks of the target analyte [20]. The polymer itself, when it is spin cast on the SERS substrate, will show an enhanced Raman signal which might or might not swamp weak signals from the analyte. As with any MIP, one should ensure that the MIP of choice can release the template molecule with a solvent wash and also recapture it when the analyte is reintroduced. Finally this MIP should have selectivity for the target molecule components [20].

Holthoff *et al.* integrated MIP films in the 7–10 μm thickness range with a SERS-active surface as the sensing layer for SERS detection of 2,4,6-trinitrotoluene (TNT) [20]. They were able to detect TNT with a 6 μM detection limit without polymer background interference. Kantarovich *et al.* deposited an MIP droplet array on SERS-active substrates for detection of S-propranolol and 2,2-dimethoxy-2-phenyl acetophenone (DPAP) [21, 22].

Many factors dynamically affect the geometry of interaction between the surface and the adsorbed molecule before and during the Raman experiment under the in-

cident laser. One such factor is the sample dryness. As Kim *et al.* reported, when the solvent (10^{-5} M, 50% methanol in de-ionized water) was evaporating the solute (4-aminobenzenethiol (4-ABT)) SERS signal changed due to the increased contribution of chemical enhancement to the electromagnetic enhancement, so that when all the solvent was gone, all peak intensities stabilized [27]. This is because the solvent presence affects the molecular angle with regard to the surface. In the work by Kim *et al.*, the drier the surface the smaller is the angle. But when the SERS study is assisted with MIP thin films, we have a polymeric medium (MIP) that confines each molecule in a specific direction. This prevents its changing angle and orientation with regard to the substrate. This means that the averaged SERS signal from a specific region of the substrate will stay the same for repeated measurements, provided that the laser-substrate interaction angle is kept the same.

When this geometry factor is fixed by incorporating an MIP film onto a flat substrate, the reproducibility will be more achievable. It can be useful to change the laser polarization direction to distinguish between otherwise similar molecules. The laser polarization angle should be "optimized". It is essential to control the laser field direction between experiments, as discussed in 5.2.4.

Bibliography

[1] Wei, A.; Kim, B.; Sadtler, B.; Tripp, S. *ChemPhysChem* **2001,** *2,* 743-745.

[2] Wilson, D. M.; Hoyt, S.; Janata, J.; Booksh, K.; Obando, L. *IEEE Sensors J.* **2001,** *1,* 256-274.

[3] Halvorson, R. A.; Vikesland, P. J. *Environ. Sci. Technol.* **2010,** *44,* 7749-7755.

[4] Gordon, R.; Sinton, D.; Kavanagh, K. L.; Brolo, A. G. *Acc. Chem. Res.* **2008,** *41,* 1049-1057.

[5] Fleischman, M.; Hendra, P. J.; McQuillan, A. J. *Chem. Phys. Lett.* **1974,** *26,* 163-166.

[6] Hoffmann, A.; Lenkefi, Z.; Szentirmay, Z. *J. Phys. Condens. Matter* **1998,** *10,* 5503-5513.

[7] Smith, E.; Dent, G. *Modern Raman Spectroscopy: A Practical Approach;* John Wiley & Sons, Inc.: Chichester, 2005.

[8] Etchegoin, P. G.; Galloway, C.; Le Ru, E. C. *Phys. Chem. Chem. Phys.* **2006,** *8,* 2624-2628.

[9] Lombardi, J. R.; Birke, R. L. *Acc. Chem. Res.* **2008,** *42,* 734-742.

[10] Lin, X.-M.; Cui, Y.; Xu, Y.-H.; Ren, B.; Tian, Z.-Q. *Anal. Bioanal. Chem.* **2009,** *394,* 1729-1745.

[11] http://microchem.com/pdf/SU-82000DataSheet2000_5thru2015Ver4.pdf, 2014.

[12] del Campo, A.; Greiner, C. *J. Micromech. Microeng.* **2007,** *17,* R81-R95.

[13] Genolet, G.; Brugger, J.; Despont, M.; Drechsler, U.; Vettiger, P.; de Rooij, N. F.; Anselmetti, D. *Rev. Sci. Instrum.* **1999,** *70,* 2398-2401.

[14] Nordström, M.; Johansson, A.; Sánchez Nogueron, E.; Calleja, M.; Boisen, A. *Microelectron. Eng.* **2005,** *78-79,* 152-157.

[15] Meyer, G.; Amer, N. M. *Appl. Phys. Lett.* **1988,** *53,* 2400-2402.

[16] Pechmann, R.; Kohler, J. M.; Fritzsche, W.; Schaper, A.; Jovin, T. M. *Rev. Sci. Instrum.* **1994,** *65,* 3702-3706.

[17] Meng, A. C.; LeJeune, J.; Spivak, D. A. *J. Mol. Recognit.* **2009,** *22,* 121-128.

[18] Dickert, F. L.; Tortschanoff, M.; Bulst, W. E.; Fischerauer, G. *Anal. Chem.* **1999,** *71,* 4559-4563.

[19] McStay, D.; Al-Obaidi, A. H.; Hoskins, R.; Quinn, P. J. *J. Opt. A: Pure Appl. Opt.* **2005,** *7,* S340-S345.

[20] Holthoff, E. L.; Stratis-Cullum, D. N.; Hankus, M. E. *Sensors* **2011,** *11,* 2700-2714.

[21] Kantarovich, K.; Tsarfati, I.; Gheber, L. A.; Haupt, K.; Bar, I. *Biosens. Bioelectron.* **2010,** *26,* 809-814.

[22] Kantarovich, K.; Tsarfati, I.; Gheber, L. A.; Haupt, K.; Bar, I. *Anal. Chem.* **2009,** *81,* 5686-5690.

[23] Pieczonka, N.; Aroca, R. *ChemPhysChem* **2005,** *6,* 2473-2484.

[24] Xia, Y. N.; Halas, N. J. *MRS Bull.* **2005,** *30,* 338-344.

[25] Ling, X.; Wu, J.; Xu, W.; Zhang, J. *Small* **2012,** *8,* 1365-1372.

[26] Etchegoin, P. G.; Le Ru, E. C. *Phys. Chem. Chem. Phys.* **2008,** *10,* 6079-6089.

[27] Kim, N.-J.; Lin, M.; Hu, Z.; Li, H. *Chem. Commun.* **2009,** 6246-6248.

Appendix A

Supplementary information for "Improved Adhesion of Gold Thin Films Evaporated on Polymer Resin: Applications for Sensing Surfaces and MEMS"*

A.1 Example force curve

Figure A.1 is the force curve from the post-deposition-cured sample and Figure A.2 is the magnified view of the contact region.

*This Appendix is a modified version of supplementary information for "Improved Adhesion of Gold Thin Films Evaporated on Polymer Resin: Applications for Sensing Surfaces and MEMS", Moazzez B, O'Brien SM, Merschrod S EF, *Sensors* **13**, 7021-7032 (2013).

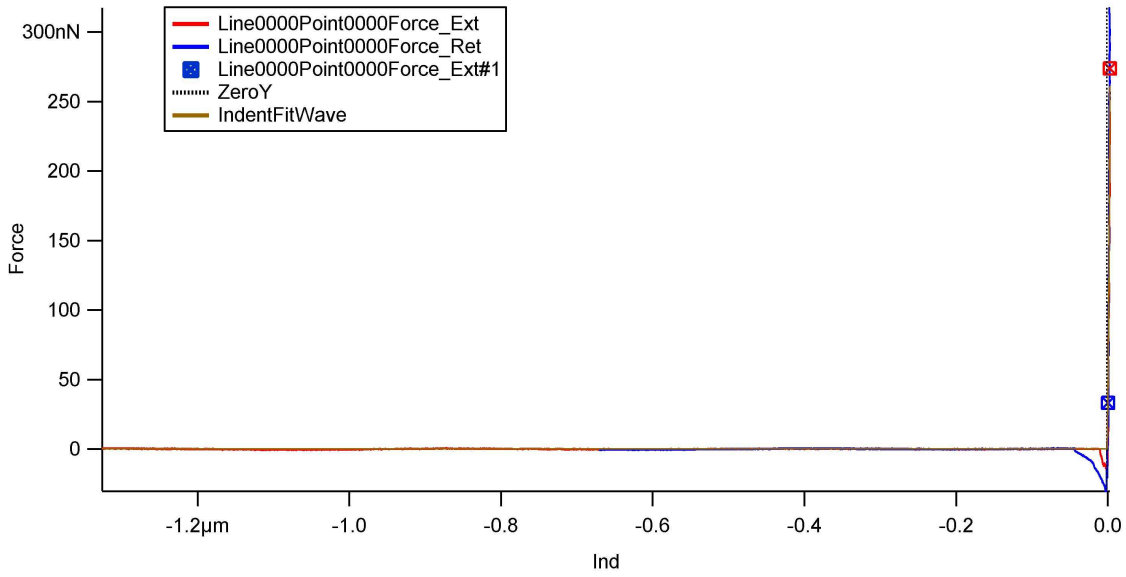

Figure A.1: A typical force curve from the post-deposition-cured sample

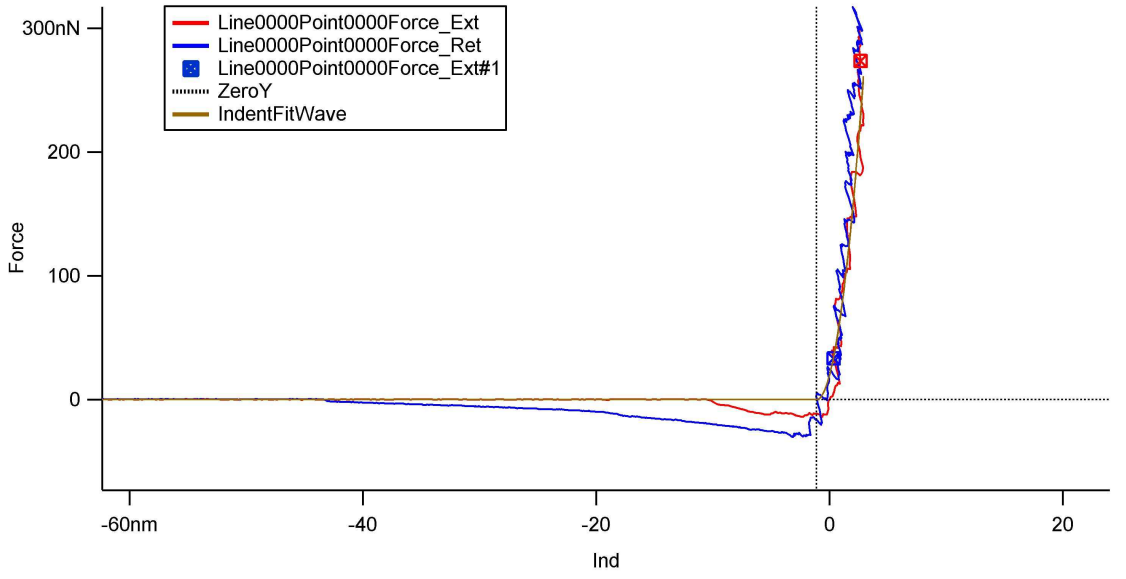

Figure A.2: Magnified view of the same force curve from the post-deposition sample, showing the region fitted to calculate adhesion and elastic modulus

A.2 Calibration of the cantilever force constant

In order to determine the cantilever spring constant using the thermal method, the tip was first brought into contact with the mica surface and the deflection measured. This was done by acquiring a single force curve. Then a second force curve was obtained to determine the slope of the contact region, which is the inverse optical lever sensitivity of the cantilever (in nm/V). Optical lever sensitivity (OLS) is defined as the cantilever deflection (in V) divided by the Z sensor displacement (in nm). This is explained in detail by Emerson and Camesano [1]. In the last step the cantilever's natural resonance frequency was obtained when the tip was withdrawn from the mica surface. This step produces a power spectrum (amplitude versus frequency) in which the area under the natural resonance peak (fundamental mode) gives the thermal noise (x^2) [2]. A built-in routine within the software provided by the AFM manufacturer (Asylum Research MFP-3D system) calculated the spring constant using the equipartition theorem and the temperature as measured by the temperature sensor in the scanner. For the comparison of measured and manufacturer-provided force constant and resonance frequency values for a NSC35/AlBS silicon tip (MikroMasch), see Table A.1.

Table A.1: MikroMasch manufacturer cantilever specifications for NSC35/AlBS (tip B) and comparison to measured force constant (thermal method) and resonance frequency. **Manufacturer** column presents the expected specification range provided by manufacturer (nominal values). **Measurement** shows the actual values which were obtained experimentally

	Manufacturer	**Measurement**
Resonance Frequency, kHz	min:240, typical:315, max:405	249.978
Force Constant, N/m	min:6.5, typical:14, max:27.5	20.25

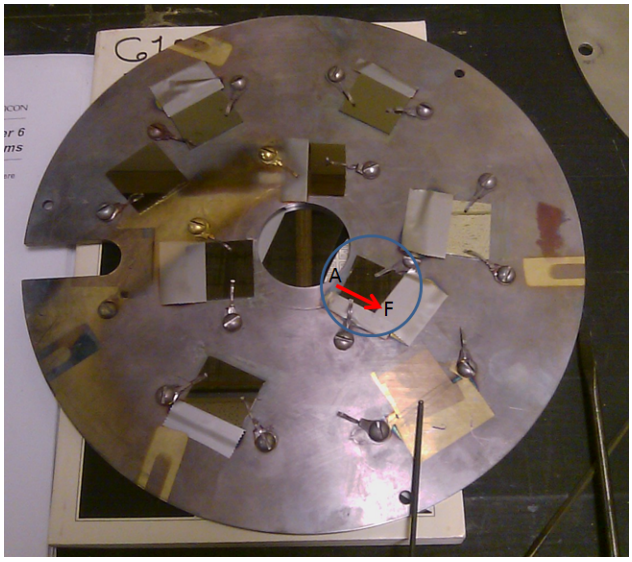

Figure A.3: The picture illustrates the sample holder of the metal evaporator device (after a metal deposition run) on which glass slides are mounted. The circled sample shows a glass slide which was partially masked by tape to avoid metal deposition on the edge of the slide. This is in order to create a clear metal thin film boundary on the glass slide for the purpose of subsequent thickness measurements with AFM.

A.3 Thickness measurement

A thickness measurement can be performed by scanning in contact mode across a masked region where there is a clear boundary between the metal deposited region and the masked region where no metal is deposited, such as indicated in Figure A.3. The AFM tip was moved perpendicular to the boundary (e.g. perpendicular to the red arrow in Figure A.3) to obtain a contact mode image. A subsequent section analysis on the height image was done along a line profile perpendicular to the boundary to obtain the height difference across the boundary which gives the thin film thickness.

Bibliography

[1] Emerson, R. J.; Camesano, T. A. *Ultramicroscopy* **2006,** *106,* 413-422.

[2] Walters, D. A.; Cleveland, J. P.; Thomson, N. H.; Hansma, P. K.; Wendman, M. A.; Gurley, G.; Elings, V. *Rev. Sci. Instrum.* **1996,** *67,* 3583-3590.

Appendix B

Supplementary information for SU-8 polymer resin

The SU-8 photoresist which is used in this PhD project was bought from the MicroChem company. The model is SU-8 2010 from the SU-8 2000 series. The company offers SU-8 with a range of twelve standard viscosities. Film thicknesses of 0.5 to 200 μm can be fabricated with these wide-ranging viscosities. There are two points here which are worth mentioning: low viscosity adhesives provide good wetting of the substrate [1] while the adhesive with very low viscosity tends to flow easily resulting in thinner film when spin cast on the substrate. The manufacturer suggests that SU-8 should be kept in a refrigerator in order to preserve its properties during the course of time. Viscosity is directly proportional to temperature. Hence in our experiments SU-8 polymer was left at room temperature for half an hour before spin cast. This is of importance because this will have an immediate impact on the wettability and final thickness of the polymer and thickness reproducibility. SU-8 is a negative photoresist which means the exposed area of the film is insoluble in SU-8 solvent.

Photoresist is a light-sensitive material used in several industrial processes, such as

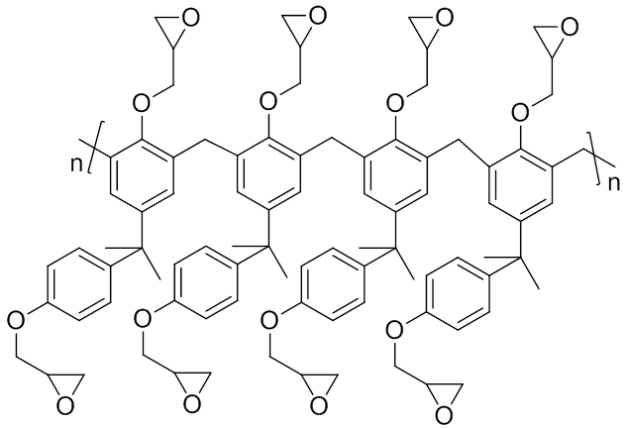

Figure B.1: When exposed to UV light followed by thermal treatment, SU-8's long molecular chains join from their epoxy group ends. This results in SU-8 hardening.

photolithography, to fabricate a patterned polymeric coating on a surface. SU-8 photoresist contains epoxide groups. When cured (here by light and thermal treatment) it turns into a clear and tough epoxy polymer. See Figure B.1 for the chemical structure of SU-8. For more information and physical properties refer to the manufacturer's manual, and for "processing guidelines" for the SU-8 2000 series [2, 3]. When SU-8 is spin cast on the pre-cleaned substrate the subsequent curing process is comprised of three steps, pre-exposure bake, exposure bake and post-exposure bake. In the first step the solvent is evaporated to create adhesion between SU-8 and the substrate [4]. Upon exposure to UV light a strong acid forms and during immediate post-exposure baking (PEB) acid-catalyzed, thermally-driven epoxy cross-linking occurs [4]. See Figure B.2 for the schematic of the gold substrate fabricated on SU-8.

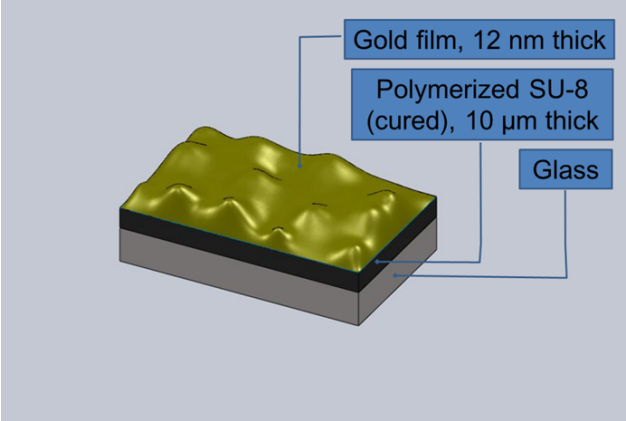

Figure B.2: Gold thin film fabricated on an SU-8 cast glass slide according to the proposed recipe. When exposed to UV light followed by thermal treatment, SU-8 hardens and shrinkage of the polymeric layer results in a rough top gold layer. The top gold layer thickness is 10 nm and SU-8 thickness is 10 μm

Bibliography

[1] Daly, J. G.; Daly, D. J. *Proc. SPIE Int. Soc. Opt. Eng.* **2001,** *4444,* 177-184.

[2] http://microchem.com/pdf/SU-82000DataSheet2000_5thru2015Ver4.pdf, 2014.

[3] http://microchem.com/pdf/SU-8-table-of-properties.pdf, 2014.

[4] del Campo, A.; Greiner, C. *J. Micromech. Microeng.* **2007,** *17,* R81-R95.

Appendix C

Supplementary information for "Annealing Approach to Hot Spots for SERS Substrates: Applications to the Detection of Polycyclic Aromatic Hydrocarbons (PAHs)"

C.1 AFM

AFM tapping mode images (Figure C.1) provide morphological data for as-deposited bilayer films and their annealed versions. The roughness of each sample is also provided in Figure C.1.

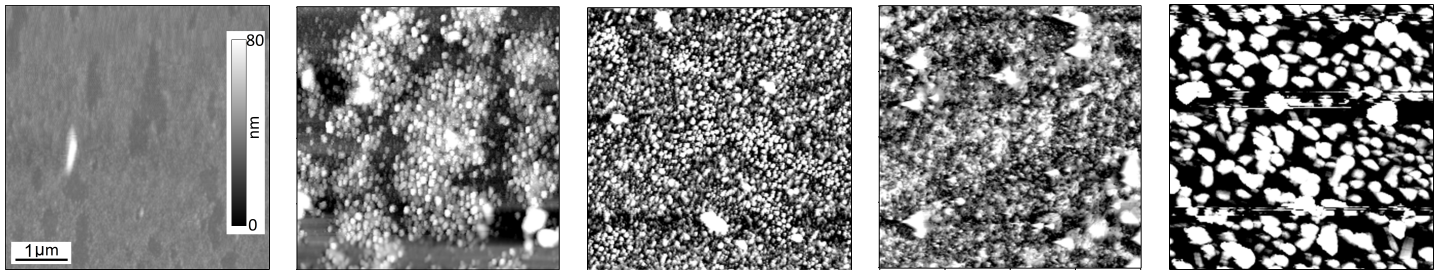

(a) Sample 1: Au=21 nm/Cr=14 nm, 3.34 ± 1.18 nm

(b) Sample 1, 325 °C, 1 h, 22.35 ± 2.81 nm

(c) Sample 1, 325 °C, 2 h, 37.50 ± 3.68 nm

(d) Sample 1, 400 °C, 1 h, 28.21 ± 2.54 nm

(e) Sample 1, 400 °C, 2 h, 113.58 ± 21.78 nm

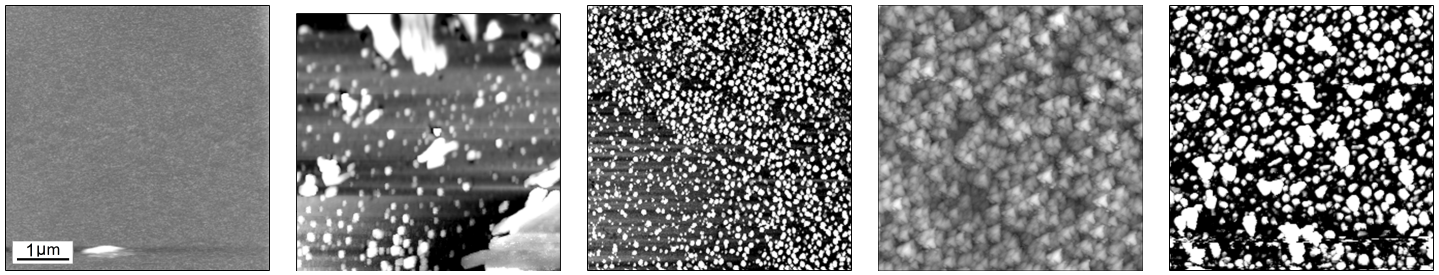

(f) Sample 2: Au=42 nm/Cr=31 nm, 4.03 ± 1.68 nm

(g) Sample 2, 325 °C, 1 h, 26.72 ± 5.94 nm

(h) Sample 2, 325 °C, 2 h, 44.65 ± 7.66 nm

(i) Sample 2, 400 °C, 1 h, 11.00 ± 0.71 nm

(j) Sample 2, 400 °C, 2 h, 97.59 ± 13.04 nm

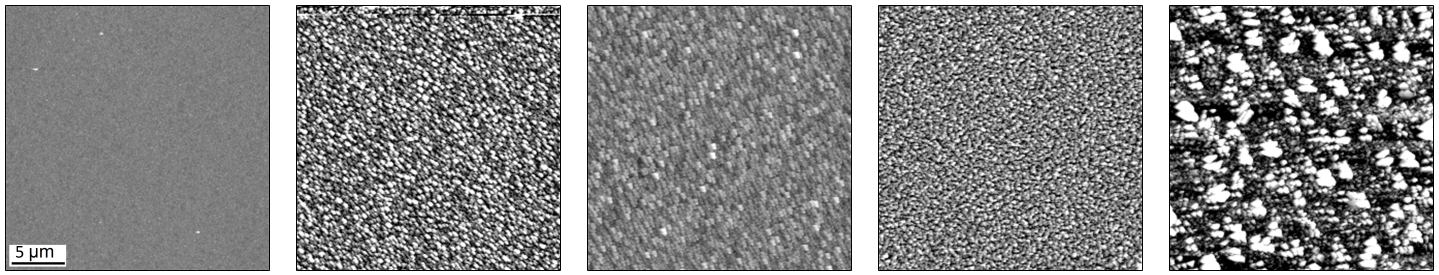

(k) Sample 3: Au=13 nm/Cr=17 nm, 2.87 ± 0.13 nm

(l) Sample 3, 325 °C, 1 h, 28.44 ± 1.58 nm

(m) Sample 3, 325 °C, 2 h, 9.42 ± 0.32 nm

(n) Sample 3, 400 °C, 1 h, 19.50 ± 0.29 nm

(o) Sample 3, 400 °C, 2 h, 42.70 ± 3.97 nm

Figure C.1: AFM tapping mode images. Each row presents a bilayer as-deposited Au/Cr sample along with its corresponding various thermally treated counterparts with their roughness value mentioned below each image. All images are 20x20 μm except as-deposited Au=21 nm/Cr=14 nm (a), Au=42 nm/Cr=31 nm (f) bilayer films and Sample 2, 400 °C, 1 h (i) which are 5x5 μm. The z colour-scale for all images is 0-80 nm as shown in image (a). Thermally treated samples reveal the change in morphology and roughness. For example surface features for samples annealed for 2 hours (2 h) at 400 °C are larger in comparison to the samples annealed for 1 hour (1 h) at the same temperature. The same trend is seen for their roughness. Roughness data are calculated by averaging over four areas across each scan.

C.2 Bands in UV-Vis reflection spectra

Figures C.2 and C.3 represent the original data where a smoothing function is not applied. As becomes clear upon comparing these original spectra to the smoothed data provided in the text (Figures 3.7 and 3.8), smoothing has preserved the main features in the original spectra without creating new features (artifacts). Smoothing makes it easier to identify peak maxima values and to detect trends in sample optical properties.

C.3 UV-Vis instrumentation details

The R200-MIXED probe (Ocean Optics) contains fourteen optical fibers consisting of 6 UV/Vis fibers and 6 Vis/NIR fibers plus 1 UV/Vis and 1 Vis/NIR read fiber. R200-MIXED has a 3.0 in by 0.25 in stainless steel ferrule to hold its optical fibers. This probe is for reflection experiments in the 200–1100 nm range which covers UV-Vis-Shortwave NIR. Each fiber core diameter is 200 μm. The numerical aperture for this probe is 0.22 which yields an acceptance angle of 24.8° in air [1]. The numerical aperture for an optical fiber is defined by Equation C.1 [2]:

$$N.A. = n_{air} Sin\theta_{max} = \sqrt{n_{core}^2 - n_{clad}^2} \tag{C.1}$$

in which $N.A.$ is the numerical aperture of the optical fiber, n_{air}, n_{core} and n_{clad} are refractive indices of air, optical fiber and the cladding which covers the optical fiber respectively. θ_{max} is the acceptance angle (the half angle of the acceptance cone) within which the entered light can propagate through the optical fiber. Figures C.5 and C.4 represent detailed information about the optical fibers used in the UV-Vis reflection probe.

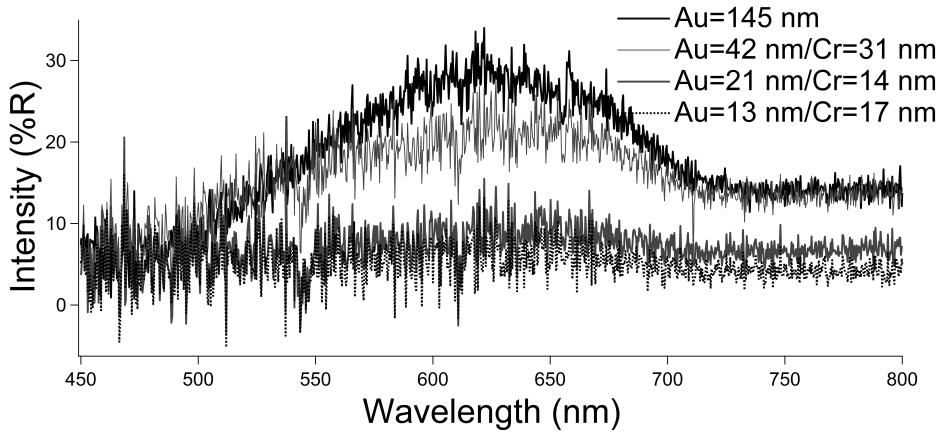

Figure C.2: Original UV-Vis reflection spectra (without smoothing) of bilayer films and a single layer gold film. The reflection property of bilayer films correlates with the gold thickness.

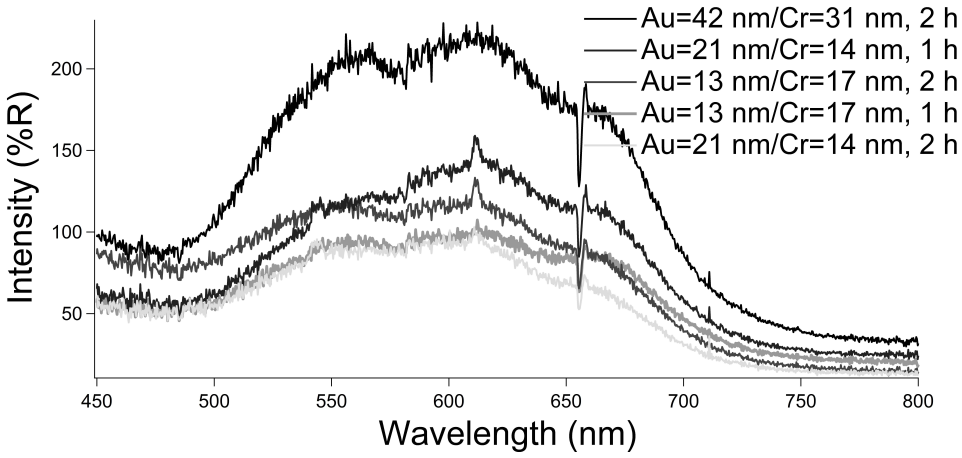

Figure C.3: Original UV-Vis reflection spectra (without smoothing) of films annealed at 400 °C for 1 hour (1 h) or 2 hours (2 h).

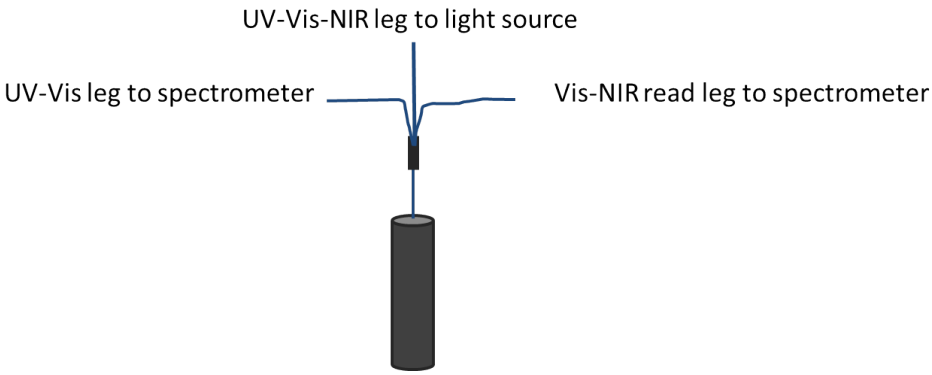

Figure C.4: The R200-MIXED reflection/backscattering probe for expanded wavelength coverage. The leg which goes to the light source consists of 12 optical fibers, 6 for UV-Vis and 6 for VIS-NIR. The UV-Vis leg can carry the signal in the range of 200–750 nm. The other leg carries the signal in the 450–100 nm range. Only one leg at a time can be connected to the spectrometer. In experiments performed here in this thesis the UV-Vis leg was used.

Figure C.5: The R200-MIXED reflection/backscattering probe is for expanded wavelength coverage. The diameter is 0.25 in (6.35 mm). This is almost four times the diameter of the inner circle which contains the optical fibers. Hence the diameter of the circle on the sample which is illuminated by probe could be estimated to be roughly in the range of 1.6–6.35 mm.

C.4 Solubility limits and other physical properties of phenanthrene

The solubility limit of phenanthrene in ethanol is 0.182 M at 25 °C [3]. The melting and boiling points are 101 °C and 332 °C respectively [4], which are higher than those of naphthalene with 80.2 °C and 217.9 °C respectively [5]. Compared to naphthalene, the Raman results should not be that prone to quick vaporization for phenanthrene under laser exposure when the SERS substrate is exposed under the microscope to a high energy laser excitation of 532 nm.

C.5 Raman

Raman spectra from the literature show the finger-print features for phenanthrene with different laser excitations [6] (see Figure C.6). Figure C.7 presents SER spectra for phenanthrene over a wider wavenumber shift range than in Chapter 3, showing other peaks in addition to the CCC bending band.

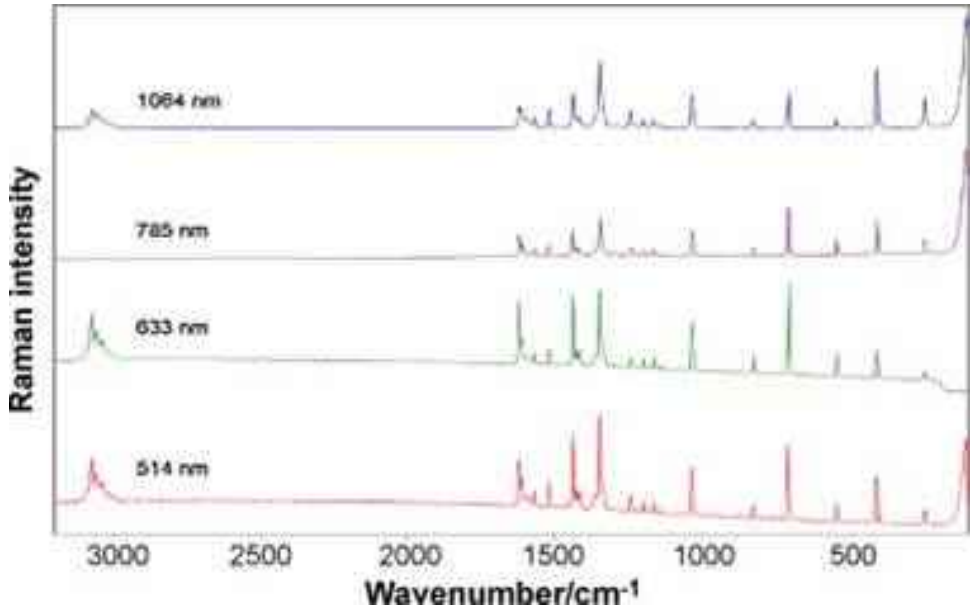

Figure C.6: Raman spectra of solid phenanthrene obtained with 1064, 785, 633 and 514 nm lasers (used with permission from [6]).

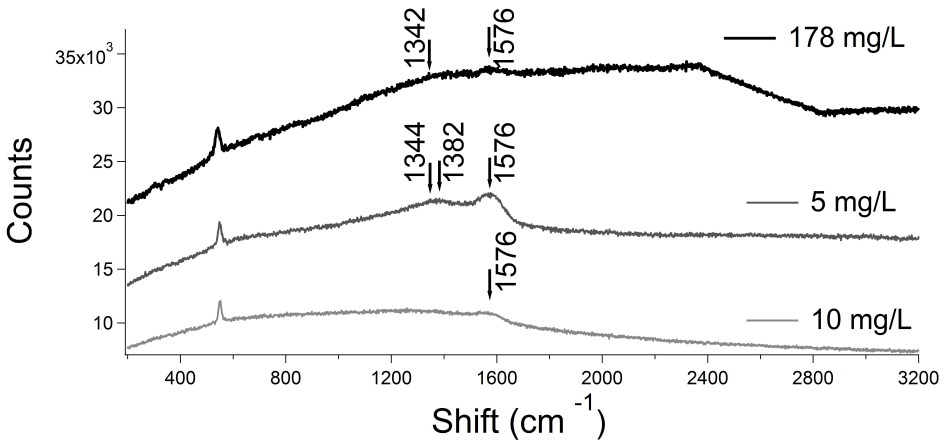

Figure C.7: The Au=42 nm/Cr=31 nm sample annealed at 400 °C for 2 hours (2 h) shows sufficient SERS activity for detecting the analyte at different concentrations when immersed in ethanol solutions for 5 seconds. These spectra are the same spectra presented in Figure 3.13 but with a larger window for wavenumber shift values on the x axis.

C.5.1 Laser power

Alajtal *et al.*, in their study of laser wavelength effects on the Raman spectra of solid state phenanthrene with 1064, 785, 633 and 514 nm excitations, have used these settings: laser power 50 mW, 5 accumulations, 10 seconds exposure time per each accumulation. With these settings the total acquisition time was 8 minutes [6]. In the work described in this thesis 70 mW power is used to obtain a high enough signal from the small concentration of phenanthrene adsorbates on the surface. This is in contrast to the work by Alajtal *et al.*, who used 50 mW power to measure spectra of solid-state bulk phenanthrene and therefore did not suffer from a small amount of samples. Even with the high laser power, the spectra in this thesis still show clear phenanthrene peaks and no peaks can be attributed to decomposition products. Nonetheless it is suggested for the future to find the minimal laser power (in the range of μW for SERS studies) required to still obtain a signal in order to avoid possible photodecomposition and substrate heating [7]. Heating effects can also be avoided by integrating the SERS substrate into a microfluidic device (for heat dissipation) [7] and using faster scan rates (μs) (to reduce exposure time) [8].

C.5.2 Laser spot

Laser spot diameter is defined by Equation C.2 [9]:

$$a = \frac{1.22\lambda}{N.A.} \tag{C.2}$$

where a is the laser spot diameter, $N.A.$ is the numerical aperture of a 100X objective lens and λ is the wavelength of the laser which is 532 nm here. This theoretical formula is applicable in standard optical microscopy but for Raman spectroscopy, due to laser scattering and the interaction of the laser with molecules and interfaces, the optical

processes are more complex [10]. For the same situation (same laser wavelength and same N.A. as applied here) the laser spot size is expected to be around 1 μm.

C.5.3 Optical density

Optical density d (Equation C.3) is defined as

$$d = -log\frac{I}{I_0} \tag{C.3}$$

I is the intensity of light transmitted through the filter (filtered light) and delivered to the sample. I_0 is the unfiltered light intensity. When d is equal to 1 it means the intensity of the filtered light is 10 times attenuated ($I = 0.1I_0$) while for $d = 0.6$ it is attenuated to a quarter of its original intensity ($I = 0.25I_0$).

Bibliography

[1] http://www.oceanoptics.com/Products/reflectionprobesreference.asp, 2014.

[2] Mitschke, F. *Fiber Optics Physics and Technology;* Springer: Heidelberg, 2009.

[3] Fakhree, M. A. A.; Shayanfar, A.; Acree, W. E.; Jouyban, A. *J. Chem. Eng. Data* **2009,** *54,* 1405-1408.

[4] Lide, D., Ed.; *CRC Handbook of Chemistry and Physics;* CRC Press, Taylor & Francis: Boca Raton, FL, 88th ed.; 2007-2008.

[5] O'Neil, M. J., Ed.; *The Merck Index - An Encyclopedia of Chemicals, Drugs, and Biologicals;* Merck and Co., Inc.: Whitehouse Station, NJ, 13th ed.; 2001.

[6] Alajtal, A. I.; Edwards, H. G. M.; Elbagerma, M. A.; Scowen, I. J. *Spectrochim. Acta, Part A* **2010,** *76,* 1-5.

[7] Cialla, D.; März, A.; Böhme, R.; Theil, F.; Weber, K.; Schmitt, M.; Popp, J. *Anal. Bioanal. Chem.* **2012,** *403,* 27-54.

[8] Yeo, B.-S.; Schmid, T.; Zhang, W.; Zenobi, R. *Appl. Spectrosc.* **2008,** *62,* 708-713.

[9] Wayne, R. *Light and Video Micrroscopy;* Academic Press: Burlington, 2009.

[10] Smith, E.; Dent, G. *Modern Raman Spectroscopy: A Practical Approach;* John Wiley & Sons, Inc.: Chichester, 2005.

Appendix D

Supplementary information for "TDHF Study of Laser Field Directionality and Energy Effects on Raman Intensities of Oriented PAHs; With Applications to the Detection of PAHs with SERS"

D.1 Sample input file for an ordinary Raman calculation

Ordinary Raman calculations in GAMESS-US [1,2] require two steps. The first step is to obtain the Hessian matrix of force constants from an optimized geometry. This can

be done in two ways: by running two separate jobs consecutively (one for optimization and one for obtaining Hessians) or by running a single job which performs both in sequence. When this first step is done then the final step will be the actual ordinary Raman calculation. Below is an example of a script for single optimization and Hessian calculation at once for the phenanthrene molecule.

```
 $CONTRL SCFTYP=RHF RUNTYP=OPTIMIZE MAXIT=30 MULT=1 $END
 $SYSTEM TIMLIM=525600 MEMORY=220000000 $END
 $BASIS GBASIS=N31 NGAUSS=6 NDFUNC=1 NPFUNC=1 $END
 $GUESS GUESS=HUCKEL $END
 $SCF DIRSCF=.TRUE. $END
 $STATPT OPTTOL=0.0001 NSTEP=200 HSSEND=.t. $END
 $FORCE METHOD=ANALYTIC VIBANL=.TRUE. $END
 $DATA
phen
Cnv 2

C           6.0   3.5414744651   0.0000000000  -0.3054142105
C           6.0   2.8656450469   0.0000000000  -1.5338959925
C           6.0   1.4960714892   0.0000000000  -1.5701912848
C           6.0   0.7297111786   0.0000000000  -0.3857869056
C           6.0   1.4144701798   0.0000000000   0.8432803347
C           6.0   2.8230807753   0.0000000000   0.8586831063
C           6.0   0.6705919482   0.0000000000   2.0746876201
H           1.0   4.6117343605   0.0000000000  -0.2824855748
H           1.0   3.4224308219   0.0000000000  -2.4483864334
H           1.0   1.0107122038   0.0000000000  -2.5215750431
```

```
H           1.0   3.3274906826   0.0000000000   1.8040929681
H           1.0   1.2164595800   0.0000000000   2.9965114554
 $END
```

The data file of this run will contain GRAD, HESS and DIPDR groups which need to be included within the script for the final Raman calculation along with the optimized geometry obtained from the output file of optimization run. Care must be taken to select the final GRAD and HESS groups from the data file, not the initial ones. Below is an example of a script for an ordinary Raman calculation which contains GRAD, HESS and DIPRD groups copied from the data file of an optimization/Hessian run. Part of the HESS group is cut for brevity.

```
 $contrl scftyp=rhf runtyp=Raman $end
 $system timlim=525600 MEMORY=220000000 $end
 $basis GBASIS=N31 NGAUSS=6 NDFUNC=1 NPFUNC=1 $end
 $guess guess=huckel $end
 $scf dirscf=.true. conv=1d-6 $end
 $Raman $end
 $data
phen
Cnv 2

C           6.0   3.5401435645  -0.0000000000  -0.3032493701
C           6.0   2.8653917116  -0.0000000000  -1.5319155975
C           6.0   1.4983158103  -0.0000000000  -1.5705382238
C           6.0   0.7305471367   0.0000000000  -0.3873021292
C           6.0   1.4133249226   0.0000000000   0.8398136625
```

```
C           6.0   2.8216165041  -0.0000000000   0.8580142841
C           6.0   0.6693039637   0.0000000000   2.0732488833
H           1.0   4.6153958046  -0.0000000000  -0.2784567132
H           1.0   3.4253089989   0.0000000000  -2.4503903383
H           1.0   1.0139524657   0.0000000000  -2.5276590007
H           1.0   3.3273364873  -0.0000000000   1.8081263898
H           1.0   1.2164540411  -0.0000000000   2.9998281929
 $end
 $GRAD
E=     -536.0276484512  GMAX=   0.0000785  GRMS=   0.0000177
C            6.   -2.5303167908E-06    3.0986420191E-22   -1.6351301837E-05
C            6.    2.5303167908E-06    0.0000000000E+00   -1.6351301837E-05
C            6.    7.5584550143E-06   -9.2561320356E-22    1.8008291904E-05
C            6.   -7.5584550143E-06    0.0000000000E+00    1.8008291904E-05
C            6.    3.3630250566E-05   -4.1183818524E-21    1.0939749650E-05
C            6.   -3.3630250566E-05    0.0000000000E+00    1.0939749650E-05
C            6.   -1.5039824003E-05    1.8417864035E-21    1.2592581371E-05
C            6.    1.5039824003E-05    0.0000000000E+00    1.2592581371E-05
C            6.   -5.0239496892E-06    6.1523607107E-22   -7.8461644499E-05
C            6.    5.0239496892E-06    0.0000000000E+00   -7.8461644499E-05
C            6.    2.1999724850E-05   -2.6941002834E-21    5.0478952511E-06
C            6.   -2.1999724850E-05    0.0000000000E+00    5.0478952511E-06
C            6.    6.8589230517E-06   -8.3994807505E-22    1.9084190306E-05
C            6.   -6.8589230517E-06    9.8607613153E-32    1.9084190306E-05
H            1.   -3.9894670651E-06    4.8855267163E-22    4.6211546998E-06
H            1.    3.9894670651E-06    0.0000000000E+00    4.6211546998E-06
```

```
H           1.   -1.3734608089E-06    1.6819488333E-22   -4.3712908173E-06
H           1.    1.3734608089E-06    0.0000000000E+00   -4.3712908173E-06
H           1.    3.7851732617E-05   -4.6353472266E-21    1.6142743906E-05
H           1.   -3.7851732617E-05    0.0000000000E+00    1.6142743906E-05
H           1.   -9.4004327389E-07    1.1511829661E-22    2.2275475513E-06
H           1.    9.4004327389E-07    0.0000000000E+00    2.2275475513E-06
H           1.   -2.5390813585E-07    3.1093751645E-23    1.0520080244E-05
H           1.    2.5390813585E-07    0.0000000000E+00    1.0520080244E-05
 $END
 $HESS
ENERGY IS     -536.0276484512 E(NUC) IS      779.4978918819
 1  1 8.49773320E-01-8.40186369E-17 3.46215010E-02-8.69449715E-04 0.00000000E+00
 1  2-3.04277963E-04-2.01041843E-01 1.51286089E-17 1.25730653E-01 2.87898301E-04
 1  3 0.00000000E+00-9.47429498E-04-2.39360455E-02 4.12761328E-18 3.47808653E-02
 1  4-2.31231195E-04 0.00000000E+00-9.44167885E-05 1.63811304E-03-1.15727293E-18
 1  5-1.20386656E-03-4.25542951E-04 0.00000000E+00 2.53015675E-04-2.81418253E-02
 1  6 4.49014334E-18-3.45961645E-02-7.32950834E-05 0.00000000E+00 1.32788479E-04
 1  7-2.38937404E-01 1.99856938E-17-1.68192518E-01-1.68639646E-04 0.00000000E+00
 1  8 6.65618340E-04-4.30425713E-03 1.38943630E-18 3.52795417E-03-1.34870628E-03
 1  9 0.00000000E+00 3.48733584E-04-3.75075398E-01 4.02593374E-17 7.71134146E-03
 1 10 1.13301007E-06 0.00000000E+00-4.19975903E-06 1.49788676E-02-1.30641473E-18
 1 11-2.05163697E-02-3.22810898E-05 0.00000000E+00 5.29127157E-05-6.75496855E-03
 1 12 2.00501293E-18-1.63219161E-04-3.01199486E-05 0.00000000E+00-9.56212852E-05
 1 13 1.50772405E-02-1.15022815E-18 1.87498726E-02-8.91655894E-05 0.00000000E+00
 1 14-4.81023717E-05 2.45866487E-04-4.06257654E-20-3.04800160E-04-5.42871778E-04
 1 15 0.00000000E+00-1.04450881E-04
```

```
[1065 lines were removed in between for brevity.]
$END
$DIPDR
 7.67875161E-01 0.00000000E+00-2.13966208E-01
 [71 lines were removed in between for brevity.]
$END
```

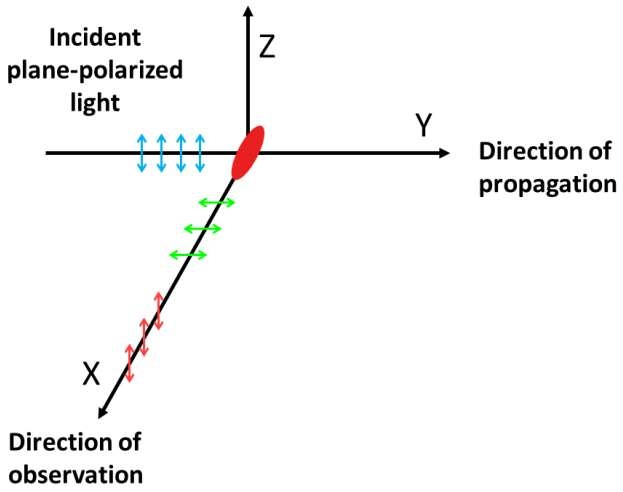

Figure D.1: Schematic of the geometry assumed by GAMESS-US in the TDHFX method for the dynamic Raman calculation of a free molecule using the "ALLDIRS" keyword. The red and green arrows are light scattered parallel and perpendicular to the direction of polarization of the incoming laser respectively.

D.2 Sample input file for a dynamic Raman calculation

The input file for a dynamic Raman calculation with the TDHFX method is provided below. The line that contains the term "ALLDIRS" requires GAMESS to calculate the molecule's response (polarizability) for a free molecule. Raman activities provided in the output file are the sum of the light scattered both parallel and perpendicular to the direction of polarization of the incoming laser. See Figure D.1 for a schematic of the geometry used for this calculation. The results of this calculation also corresponds to the interaction of natural (unpolarized) incident light with the molecule.

To calculate the dynamic Raman activities of an oriented molecule, the term "ALLDIRS" is replaced by either "DIR 1", "DIR 2" or "DIR 3" to set the polarization (electric field) direction of the incident laser to x, y or z respectively. The script "RAMAN 0.04" two lines later directs GAMESS-US to calculate the dynamic Raman activities and the value of 0.04 determines the incident laser energy in hartrees. For

static Raman calculations no value is required but just “RAMAN”.

```
 $contrl scftyp=rhf runtyp=tdhfx nosym=1 ispher=0 $end
 $system TIMLIM=525600 MEMORY=220000000 $end
 $basis  GBASIS=N31 NGAUSS=6 NDFUNC=1 NPFUNC=1 $end
 $guess  guess=huckel $end
 $scf    dirscf=.true. conv=1d-6 $end
 $force  method=analytic  $end
 $cphf   cphf=AO polar=.false. $end
 $tdhfx
   ALLDIRS
   FREQ
   RAMAN 0.04
   $end
 $data
phen-xz-plane
Cnv 2

C           6.0   3.5401435645  -0.0000000000  -0.3032493701
C           6.0   2.8653917116  -0.0000000000  -1.5319155975
C           6.0   1.4983158103  -0.0000000000  -1.5705382238
C           6.0   0.7305471367   0.0000000000  -0.3873021292
C           6.0   1.4133249226   0.0000000000   0.8398136625
C           6.0   2.8216165041  -0.0000000000   0.8580142841
C           6.0   0.6693039637   0.0000000000   2.0732488833
H           1.0   4.6153958046  -0.0000000000  -0.2784567132
H           1.0   3.4253089989   0.0000000000  -2.4503903383
```

```
H           1.0   1.0139524657   0.0000000000  -2.5276590007
H           1.0   3.3273364873  -0.0000000000   1.8081263898
H           1.0   1.2164540411  -0.0000000000   2.9998281929
 $END
```

Table D.1: Important naphthalene modes, their activities, and the first derivatives of their transition polarizabilities under altered laser field directions, calculated with TDHFX using the 6-31G(d,p) basis set and $\omega = 0.04$ hartree (IR). The activities are also given as percentages of the most intense mode (in parentheses). All modes listed here are of a symmetry.

	x polarized			y polarized			z polarized		
frequency (cm^{-1})	activity	α'	γ'	activity	α'	γ'	activity	α'	γ'
831	7.83 (2.60%)	0.0225	0.0676	19.0 (10.7%)	0.0351	0.105	0.100 (9.10%)	0.00255	0.00765
1487	205 (67.1%)	0.115	0.345	40.6 (22.8%)	0.0513	0.154	0.0100 (0.700%)	0.000689	0.00207
1620	62.3 (20.4%)	0.0635	0.191	0.190 (0.100%)	-0.00350	0.0105	0.0100 (0.900%)	0.000815	0.00245
1782	9.81 (3.20%)	0.0252	0.0756	56.4 (31.7%)	-0.0605	0.181	0.0600 (5.30%)	-0.00194	0.00583
3345	73.5 (24.1%)	-0.0690	0.207	178 (100%)	0.107	0.322	0.0700 (6.20%)	0.00210	0.00630
3371	305 (100%)	-0.141	0.421	176 (98.8%)	-0.107	0.320	1.10 (100%)	-0.00846	0.0254

Table D.2: Important naphthalene modes, their activities, and first derivatives of transition polarizabilities under unpolarized incident light calculated with TDHFX method using the 6-31G(d,p) basis set and $\omega = 0.04$ hartree (IR). The values in parentheses are Raman activity coefficients relative to the most intense mode presented as percentages.

frequency (cm^{-1})	activity	α'	γ'
831	30.5 (5.60%)	0.0601	0.0852
1487	268 (49.0%)	0.167	0.298
1620	61.8 (11.3%)	0.0608	0.195
1782	61.0 (11.1%)	-0.0372	0.228
3345	223 (40.8%)	0.0405	0.461
3371	547 (100%)	-0.256	0.356

Table D.3: Important phenanthrene modes, their activities, and the first derivatives of their transition polarizabilities under altered laser field directions, calculated with TDHFX using the 6-31G(d,p) basis set and $\omega = 0.04$ hartree (IR). The activities are also given as percentages of the most intense mode (in parentheses). All modes listed here are of a_1 symmetry.

	x polarized			y polarized			z polarized		
frequency (cm^{-1})	activity	α'	γ'	activity	α'	γ'	activity	α'	γ'
1462	302 (72.6%)	0.140	0.420	0.0100 (1.6%)	0.000930	0.00279	21.7 (17.3%)	0.0375	0.113
1405	89.5 (21.5%)	0.0761	0.228	0 (0%)	0.000084	0	1.55 (1.20%)	0.0100	0.0301
1365	85.7 (20.6%)	0.0745	0.224	0.00240 (0.300%)	0.000394	0.00118	0.930 (0.700%)	0.00776	0.0233
1705	75.4 (18.1%)	-0.0699	0.210	0 (0%)	0.000008	0	0.990 (0.800%)	-0.00802	0.0241
1840	9.69 (2.30%)	-0.0251	0.0752	0.0400 (4.70%)	-0.00161	0.00483	37.0 (29.5%)	-0.0490	-0.0490
775	3.19 (0.800%)	-0.0144	0.0431	0.100 (11.3%)	-0.00249	0.00747	18.0 (14.4%)	-0.0342	0.103

Table D.4: Important phenanthrene modes, their activities, and first derivatives of transition polarizabilities under unpolarized incident light calculated with TDHFX method using the 6-31G(d,p) basis set and $\omega = 0.04$ hartree (IR). The values in parentheses are Raman activity coefficients as a percentage of the most intense mode.

frequency (cm^{-1})	activity	α'	γ'
1462	345 (60.6%)	0.178	0.374
1405	94.0 (16.5%)	0.0862	0.215
1365	89.0 (15.6%)	0.0827	0.212
1705	79.0 (13.8%)	-0.0779	0.199
1839	51.9 (9.10%)	-0.0756	0.123
775	23.7 (4.20%)	-0.0510	0.0831

Table D.5: Effect of the laser field ($\omega = 0.04$ hartree) polarization direction on the Raman activities of naphthalene. The values in parentheses are Raman activity coefficients as a percentage of the most intense mode.

frequency (cm^{-1})	symmetry	activity			
		unpolarized	x-polarized	y-polarized	z-polarized
431	b_{2g}	6.18 (1.10)	0	0	0
519	b_{3g}	0.0400 (0)	0	0	0
551	a_g	11.6 (2.10)	11.5 (3.80)	0	0.0100 (0.800)
555	b_{1g}	7.88 (1.40)	0	0	0
810	b_{2g}	5.37 (1.00)	0	0	0
831	a_g	30.5 (5.60)	7.83 (2.60)	19.0 (10.7)	0.100 (9.10)
854	b_{3g}	6.23 (1.10)	0	0	0
992	b_{3g}	4.32 (0.800)	0	0	0
1022	b_{1g}	0.0600 (0)	0	0	0
1081	b_{2g}	0.570 (0.100)	0	0	0
1115	a_g	21.0 (3.80)	18.2 (6.00)	1.22 (0.700)	0.0700 (6.30)
1124	b_{3g}	1.61 (0.300)	0	0	0
1268	b_{1g}	19.1 (3.50)	0	0	0
1281	a_g	5.91 (1.10)	5.93 (1.90)	0	0
1368	b_{1g}	3.87 (0.700)	0	0	0
1487	a_g	269 (49.0)	205 (67.1)	40.6 (22.8)	0.0100 (0.700)
1618	b_{1g}	1.08 (0.200)	0	0	0
1620	a_g	61.8 (11.3)	62.3 (20.4)	0.190 (0.100)	0.0100 (0.900)
1782	a_g	60.7 (11.1)	9.81 (3.20)	56.4 (31.7)	0.0600 (5.30)
1843	b_{1g}	1.15 (0.200)	0	0	0
3334	b_{1g}	32.7 (6.00)	0	0	0
3345	a_g	223 (40.8)	73.5 (24.1)	178 (100)	0.0700 (6.20)
3355	b_{1g}	152 (27.7)	0	0	0
3371	a_g	547 (100)	305 (100)	176 (98.8)	1.10 (100)

Table D.6: Effect of the laser field ($\omega = 0.04$ hartree) polarization direction on the Raman activities of phenanthrene. The values in parentheses are Raman activity coefficients as a percentage of the most intense mode.

frequency (cm^{-1})	symmetry	activity			
		unpolarized	x-polarized	y-polarized	z-polarized
104	a_2	0.910 (0.200)	0	0	0
110	b_2	0.330 (0.100)	0	0	0
252	b_2	0.790 (0.100)	0	0	0
264	a_1	2.76 (0.500)	2.76 (0.700)	0.0007 (0.100)	0.140 (0.100)
265	a_2	3.61 (0.600)	0	0	0
437.1	a_1	14.5 (2.60)	14.0 (3.40)	0.0100 (1.40)	0.120 (0.100)
437.4	a_2	5.47 (1.00)	0	0	0
475	b_1	2.00 (0.400)	0	0	0
480	b_2	0.620 (0.100)	0	0	0
539	b_1	1.94 (0.300)	0	0	0
551	b_2	0.630 (0.100)	0	0	0
591	a_1	4.12 (0.700)	0.300 (0.100)	0.0200 (2.10)	3.46 (2.80)
598	a_2	6.44 (1.10)	0	0	0
649	a_2	1.64 (0.300)	0	0	0
676	b_1	1.54 (0.300)	0	0	0
773	b_1	0.890 (0.200)	0	0	0
775	a_1	23.7 (4.20)	3.19 (0.800)	0.100 (11.3)	18.0 (14.4)
789	b_2	2.11 (0.400)	0	0	0
831	b_2	1.65 (0.300)	0	0	0
849	a_2	0.140 (0)	0	0	0

Continued on next page

Table D.6 – continued from previous page

frequency (cm^{-1})	symmetry	activity			
		unpolarized	x-polarized	y-polarized	z-polarized
881	a_2	2.57 (0.500)	0	0	0
899	a_1	4.07 (0.700)	2.93 (0.700)	0.0200 (2.50)	0.670 (0.500)
917	b_2	0.130 (0)	0	0	0
955	b_1	3.14 (0.600)	0	0	0
976	a_2	0.620 (0.100)	0	0	0
981	b_2	6.63 (1.20)	0	0	0
1074	a_2	0.600 (0.100)	0	0	0
1085	b_2	0.100 (0)	0	0	0
1088	b_1	1.13 (0.200)	0	0	0
1106.0	a_2	1.33 (0.200)	0	0	0
1106.4	a_1	21.8 (3.80)	7.48 (1.80)	0.0500 (5.30)	11.6 (9.30)
1118	b_2	0.0400 (0)	0	0	0
1119	a_2	1.45 (0.300)	0	0	0
1139	b_1	0.780 (0.100)	0	0	0
1185	a_1	18.9 (3.30)	15.3 (3.70)	0.0300 (3.40)	1.92 (1.50)
1208	a_1	1.13 (0.200)	0.910 (0.200)	0.00300 (0)	0.360 (0.300)
1258	b_1	2.66 (0.500)	0	0	0
1266	b_1	6.30 (1.10)	0	0	0
1283	a_1	7.22 (1.30)	1.33 (0.300)	0	6.64 (5.30)
1301	a_1	4.52 (0.800)	4.56 (1.10)	0	0.180 (0.100)
1321	b_1	3.49 (0.600)	0	0	0
1365	a_1	89.0 (15.6)	85.7 (20.6)	0.00240 (0.300)	0.930 (0.700)

Continued on next page

Table D.6 – continued from previous page

frequency (cm^{-1})	symmetry	activity			
		unpolarized	x-polarized	y-polarized	z-polarized
1400	b_1	21.2 (3.70)	0	0	0
1405	a_1	94.0 (16.5)	89.5 (21.5)	0	1.55 (1.20)
1415	b_1	0.790 (0.100)	0	0	0
1462	a_1	345 (60.6)	302 (72.6)	0.0100 (1.60)	21.7 (17.3)
1566	b_1	11.1 (2.00)	0 (0)	0	0
1584	a_1	89.6 (15.8)	81.18 (19.5)	0.0100 (1.40)	4.15 (3.30)
1603	a_1	137 (24.2)	124 (29.9)	0	6.06 (4.80)
1620	b_1	7.40 (1.30)	0	0	0
1668	b_1	0.860 (0.200)	0	0	0
1705	a_1	78.6 (13.8)	75.4 (18.1)	0	0.990 (0.800)
1774	b_1	40.1 (7.10)	0	0	0
1806	a_1	48.6 (8.60)	48.6 (11.7)	0.0200 (2.30)	0.0200 (0)
1819	b_1	59.5 (10.5)	0	0	0
1839	a_1	51.9 (9.10)	9.69 (2.30)	0.0400 (4.70)	37.0 (29.5)
3336	b_1	4.61 (0.800)	0	0	0
3338	a_1	81.7 (14.4)	21.7 (5.20)	0.03 (3.20)	69.5 (55.5)
3340	b_1	11.0 (1.90)	0	0	0
3349	b_1	254 (44.8)	0	0	0
3350	a_1	21.7 (3.80)	4.26 (1.00)	0.170 (0.200)	19.7 (15.7)
3361	a_1	108 (19.1)	4.66 (1.10)	0.110 (12.6)	109 (86.6)
3366	b_1	0.0100 (0)	0	0	0
3368	a_1	569 (100)	416 (100)	0.850 (100)	94.9 (75.7)

Continued on next page

Table D.6 – continued from previous page

frequency (cm^{-1})	symmetry	activity			
		unpolarized	x-polarized	y-polarized	z-polarized
3379	b_1	2.47 (0.400)	0	0	0
3403	a_1	159 (27.9)	18.6 (4.50)	0.380 (44.8)	125 (100)

D.3 Raman tensors for selected modes of confined naphthalene and phenanthrene molecules

Raman tensors from the output of the TDHF calculation with a laser energy of $\omega = 0.04$ hartree for those modes of confined molecules which were tabulated in Tables 4.1 and 4.2 are collected here.

The Raman tensor under x-polarized incident laser from the output file is copied below for the mode at 831 cm^{-1} for naphthalene:

```
mode   12( 830.9 cm^-1)( -0.0400;  0.0400)

            x               y               z
x.         0.0676         0.0000         0.0000
y.         0.0000         0.0000         0.0000
z.         0.0000         0.0000         0.0000


Mean       :         0.0225
Anisotropy :         0.0676
```

Mean stands for $\bar{\alpha}'$ as defined in Equation 1.12. **Anisotropy** is $\bar{\gamma}'$ whose square is defined in Equation 1.13. Therefore the Raman tensor under x-polarized incident

laser for this mode is $\begin{pmatrix} 0.0676 & 0 & 0 \\ 0 & 0 & 0 \\ 0 & 0 & 0 \end{pmatrix}$ and under y-polarized and z-polarized laser incidents are $\begin{pmatrix} 0 & 0 & 0 \\ 0 & 0.105 & 0 \\ 0 & 0 & 0 \end{pmatrix}$ and $\begin{pmatrix} 0 & 0 & 0 \\ 0 & 0 & 0 \\ 0 & 0 & 0.00765 \end{pmatrix}$ respectively. Raman tensor for a confined molecule is composed of a single non-zero component. These values are summarized in Tables D.7 and D.8.

Table D.7: Raman tensor components of confined naphthalene for modes that show significant Raman activity changes under various laser polarization directions, calculated with the 6-31G(d,p) basis set and $\omega = 0.04$ hartree (IR).

frequency (cm^{-1})	α_{xx} x-polarized	α_{yy} y-polarized	α_{zz} z-polarized
831	0.0676	0.105	0.00765
1487	0.345	0.154	0.00207
1620	0.191	-0.0105	0.00245
1782	0.0756	-0.181	-0.00583
3345	-0.207	0.322	0.00630
3371	-0.421	-0.320	-0.0254

Table D.8: Raman tensor components of confined phenanthrene for modes that show significant Raman activity changes under various laser polarization directions, calculated with the 6-31G(d,p) basis set and $\omega = 0.04$ hartree (IR).

frequency (cm^{-1})	α_{xx} x-polarized	α_{yy} y-polarized	α_{zz} z-polarized
775	-0.0431	-0.00747	-0.103
1365	0.224	0.00118	0.0233
1405	0.228	0.000253	0.0301
1462	0.420	0.00279	0.113
1704	-0.210	0.000023	-0.0241
1839	-0.0752	-0.00483	-0.147

Bibliography

[1] Schmidt, M. W.; Baldridge, K. K.; Boatz, J. A.; Elbert, S. T.; Gordon, M. S.; Jensen, J. H.; Koseki, S.; Matsunaga, N.; Nguyen, K. A.; Su, S.; Windus, T. L.; Dupuis, M.; Montgomery, J. A. *J. Comput. Chem.* **1993,** *14*, 1347-1363.

[2] Gordon, M. S.; Schmidt, M. W. Advances in electronic structure theory: GAMESS a decade later. In *Theory and Applications of Computational Chemistry: the first forty years*; Dykstra, C. E.; Frenking, G.; Kim, K. S.; Scuseria, G. E., Eds.; Elsevier: Amsterdam, 2005.